Path Planning and Guidance Laws of a Formula Student Driverless Car

Solange Dolores Rebocho dos Santos

Thesis to obtain the Master of Science Degree in

Mechanical Engineering

Supervisors: Prof. Miguel Afonso Dias de Ayala Botto
Prof. José Raul Carreira Azinheira

Examination Committee

Chairperson: Prof. Carlos Baptista Cardeira
Supervisor: Prof. Miguel Afonso Dias de Ayala Botto
Member of the Committee: Prof. Rita Maria Mendes de Almeida Correia da Cunha

November 2021

"Daring ideas are like chessmen moved forward; they may be beaten, but they may start a winning game."

<div align="right">– Johann Wolfgang von Goethe</div>

Acknowledgments

I would like to thank to my supervisors professors Miguel Ayala Botto and José Raul Azinheira and to professor Alexandra Moutinho as well, for all the insight, knowledge and advice, particularly during a year of remote work. A special thanks to professor Duarte Valério for his incredible patience and unflagging help during the development of this thesis.

A sincere thank you to André Barroso and Alexandre Athayde for their immense contribution and willingness to help throughout this process, undoubtedly marked by they being a part of it, not only from a technical point of view but also from a motivational one.

Finally, although no less important, a word of appreciation goes out to my family and friends for their everlasting and relentless support, encouragement and patience. Thank you, for all the cheerful breaks from work, for your impact on my personal growth and for a fellowship that knows no bounds.

Resumo

A condução autónoma tem sido um tema de bastante interesse em diversas áreas, das quais a competição automóvel não é exceção. Pretendendo-se controlar autonomamente o futuro veículo da Formula Student Lisboa, este trabalho foi desenvolvido com o objetivo de implementar diferentes estratégias para controlo e planeamento de trajetória. Essas estratégias foram testadas em simulação, recorrendo a um modelo realista do protótipo.

Para planeamento, sendo importante em competição minimizar o tempo de prova, as referências necessárias foram geradas com esse intuito. Tendo sido seguida uma abordagem desacoplada relativamente aos subsistemas lateral e longitudinal, o caminho de referência foi obtido recorrendo a campos potenciais artificiais que, combinado com um algoritmo de duas iterações desenvolvido para gerar o perfil de velocidade, permitiu obter uma solução sub-ótima que retrata adequadamente o comportamento esperado de um condutor humano, respeitando as condições de aderência dos pneus. Seguindo esta abordagem, o processo de gerar a referência de velocidade requer um conhecimento prévio da disposição da pista. Não obstante, outra abordagem foi desenvolvida, sem que essa premissa se verifique, onde as soluções encontradas ainda retrataram o comportamento esperado, mas o desempenho relativamente à minimização do tempo diminui. Finalmente, esta última solução de planeamento foi ainda extrapolada para um cenário onde, em adição aos limites da pista, existem obstáculos estáticos.

Para controlo seguiu-se, novamente, uma abordagem desacoplada, controlando-se individualmente cada um dos subsistemas. Sendo o principal foco o guiamento, foram implementadas diversas estratégias para controlo lateral e apenas uma para controlo longitudinal.

Palavras-chave: Formula Student, condução autónoma, planeamento de trajetória, evasão de obstáculos, guiamento lateral, controlo automóvel

Abstract

Autonomous driving has been a topic of great interest in several areas, from which motor racing is no exception. Aiming to autonomously control the future Formula Student Lisboa vehicle, this work was developed with the objective of implementing different strategies for control and path planning. These strategies were tested in simulation, using a realistic model of the prototype.

For planning, as it is important in competition to minimise the time, the necessary references were generated with this in mind. The approach followed involves the decoupling of the lateral and longitudinal subsystems, where the reference path was obtained using artificial potential fields and then combined with a two passes algorithm developed to generate a speed profile. This allowed to obtain a sub-optimal solution that adequately portrays the expected behaviour of a human driver while respecting traction conditions. Following this approach, the process of generating the speed reference requires prior knowledge of the track layout. However, another approach was developed, without this premise being verified, where the solutions found continue to portray the expected behavior, but with a decrease in performance in terms of time. Finally, this last planning solution was extrapolated to a scenario where, in addition to the track limits, there is the presence of static obstacles.

For control, a decoupled approach was followed once again, controlling each one of the subsystems individually. With guidance as main focus, several strategies were implemented for lateral control and only one for longitudinal control.

x

Contents

List of Tables

List of Figures

Nomenclature

Greek symbols

α Slip angle.

β Sideslip angle.

γ Decay factor.

δ Steering angle.

Δ Linear suspension deformation; variation.

η Angle between the velocity of the car and a given look-ahead line; efficiency.

θ Generic angle.

κ Slip ratio.

λ Cooling factor.

μ Friction coefficient.

ρ Air density; normalised combined slip magnitude.

σ Sliding surface.

τ Time constant.

Φ Euler angles.

ψ Vehicle heading.

$\dot{\psi}$ Angular velocity around the z axis of the vehicle; yaw rate.

ω Wheel angular velocity.

Ω Center of gravity angular velocity.

Roman symbols

$\mathbf{A}$, $\mathbf{B}$, $\mathbf{C}$, $\mathbf{D}$ State space matrices of a linear model.

A_P	Frontal projected area of the vehicle.
a	Acceleration.
$B,\ C,\ D,\ E$	Tire stiffness factor, shape factor, peak-value of the force and curvature factor, respectively.
$C_{\alpha_F},\ C_{\alpha_R}$	Front and rear cornering stiffness.
C_x	Dissipative coefficient related to variable x.
$\mathbf{d}_{i,j}$	Displacement vector between points P_i and P_j.
d	Distance; direction.
e_δ	Difference between the actual steering and a smoother steering.
$\mathbf{e}_\psi$	Heading error.
$e_{\dot\psi}$	Estimation error for the angular velocity $\dot\psi$.
$e_{\dot e_y}$	Estimation error for the rate of change of the lateral error $\dot e_y$.
e_{ss}	Steady-state error.
e_{v_y}	Estimation error for the lateral velocity v_y.
$\mathbf{e}_y$	Cross-track error.
$F,\ \mathbf{f}$	Resultant force.
$F_{att},\ \mathbf{f_{att}}$	Attractive force.
$F_{dis},\ \mathbf{f_{dis}}$	Dissipative force.
$F_g,\ \mathbf{f_g}$	Gravitational force.
$F_{react},\ \mathbf{f_{react}}$	Reaction force.
$F_{rep},\ \mathbf{f_{rep}}$	Repulsive force.
$F_{trc},\ \mathbf{f_{trc}}$	Tractive force.
$F_x,\ \mathbf{f_x}$	Longitudinal tire force.
$F_y,\ \mathbf{f_y}$	Lateral tire force.
$F_z,\ \mathbf{f_z}$	Vertical tire force.
$g,\ \mathbf{g}$	Acceleration of gravity.
I_{zz}	Inertia moment of the vehicle around its z axis.
$\mathbf{J}$	Inertia tensor.

J	Rotational inertia; performance index.
$\mathbf{K}$	Controller gain matrix.
K	Path curvature.
K_u	Under-steer gradient.
K_x	Gain related with variable x.
$k,\ c$	Elastic and damping coefficients of the linear spring damper system.
k_{RP}	Path curvature at reference path in local coordinates.
$\mathbf{L_O}$	Observer gain matrix.
L	Wheelbase of the vehicle.
$L_F,\ L_R$	Distance of the center of gravity of the car to the front and rear axis.
L_{lad}	Look-ahead distance.
L_W	Track width of the car.
$M_z,\ \mathbf{m_z}$	Self-alignment moment.
m	Vehicle mass.
$\mathbf{P},\ \mathbf{P_0}$	Solutions of the Algebraic Riccati Equation for the Linear Quadratic Regulator controller and Kalman filter.
$P,\ \mathbf{p}$	Position of the vehicle in the global coordinate system.
$P_{\mathsf{danger}},\ \mathbf{p}_{\mathsf{danger}}$	Position of the point with higher danger level in the global coordinate system.
$P_{\mathsf{RP}},\ \mathbf{p}_{\mathsf{RP}}$	Reference point.
$P_{\mathsf{WP}},\ \mathbf{p_{WP}}$	Waypoint.
PO	Percentage overshoot.
$\mathbf{Q},\ \mathbf{R}$	Weighting matrices for the Linear Quadratic Regulator controller.
$\mathbf{Q_0},\ \mathbf{R_0}$	Weighting matrices for the Kalman filter.
$\mathbf{R_i^j}$	Rotation matrix of frame i with respect to frame j.
R	Tire radius.
$R_O,\ R_W,\ R_D,\ R_C$	Observation, warning, danger and critical radius.
r_{gear}	Drivetrain gear ratio.
r_{motion}	Motion ratio.

$\mathbf{S}, \mathbf{R}$	Rotation and transformation matrices related to vehicle tri-dimensional kinematics.
S_V, S_H	Vertical and horizontal shifts.
s, a	Normalised slip ratio and slip angle.
s	Arc length.
T	Motor torque; temperature.
T_w, $\mathbf{t_w}$	Wheel's torque.
t	Time.
$\mathbf{t}_{\mathsf{RP}}$	Tangent of path at the reference point.
t_r	Rise time.
t_s	Settling time.
U	Danger level.
v, $\mathbf{v}$	Linear velocity of the vehicle in the local coordinate system.
v_w, $\mathbf{v_w}$	Linear wheel velocity.
$\mathbf{w}, \mathbf{v}$	Process and sensor noises, respectively.
$\mathbf{x}$, $\mathbf{u}$, $\mathbf{y}$	State, input and output vectors, respectively.
X_{MF}, Y_{MF}	Magic Formula tire model input and output.

Subscripts

$\perp$	Orthogonal.
0	Initial value of a variable.
1, 2, 3, 4	Front-right, front-left, rear-right and rear-left tires.
α	Relative to slip angle.
δ	Relative to steering.
κ	Relative to slip ratio.
σ	Relative to sliding surface.
ψ	Relative to orientation.
$\dot{\psi}$	Relative to yaw rate.

Alice	Refers to Alice controller.
$att,\ rep$	Attractive and repulsive.
$bwd,\ fwd$	Backward and forward.
CG	Taken at the Center of Gravity of the vehicle.
cmd	Command.
cri	Critical value in terms of stability.
D	Drag.
d	Desired value of a variable.
danger	Taken at the point with higher danger level.
dec	Deceleration.
diff	Difference or asymmetry.
dis, dis_Ω, dis_w	Dissipation, dissipation from center of gravity rotation and dissipation from wheel rotation.
$\dot{e}_y$	Relative to the rate of change of the cross-track error.
$F,\ R,\ W$	Front, rear and wheelbase of the vehicle.
$FR,\ FL,\ RR,\ RL$	Front-right, front-left, rear-right and rear-left tires.
finish	Relative to finish the lap.
g	Gravity.
L	Lift.
lad	Look-ahead.
lim	Limit value for the variable or parameter.
lin	Linear regime.
MF	Relative to Magic Formula tire model.
m	Refers to motors.
$\max$	Maximum value for the variable or parameter.
$\min$	Minimum value for the variable or parameter.
n	Relative to segment n.
$O,\ W,\ D,\ C$	Observation, warning, danger and critical.

offset	Displacement.
P	Projected; refers to local frame origin.
PP	Refers to Pure Pursuit controller.
PT	Refers to powertrain.
pred	Prediction.
RP	Taken at the current reference point.
range	Range for the variable or parameter.
react	Reaction.
ref	Reference value.
SA	Refers to steering actuation.
$s,\ r$	Settling and rising.
ss	Steady-state.
$t,\ r,\ r_w$	Translation, rotation, wheel rotation.
trans	Transmission.
trc	Traction.
u	Under-steer.
$V,\ H$	Vertical and horizontal.
v_x	Relative to longitudinal velocity.
w	With respect to the wheel.
v_y	Relative to lateral velocity.
$x,\ y,\ z$	Cartesian components on a local referential.

Superscripts

$\hat{\ }$	Estimation.
$\overline{\ \ }$	Mean.
$\dot{\ }$	Time derivative.
$\top$	Transpose.
-1	Inverse.

$1,\ 2,\ 3,\ 4$	Front-right, front-left, rear-right and rear-left tires.
c	Corrected value.
const	Indicates constant variable or parameter.
$F,\ R$	Front and rear of the vehicle.
KLS	Kinematics Speed controller.
LQG	Linear Quadratic Gaussian controller.
MSM	Modified Sliding Mode controller.
min	Minimum value.
ref	Reference value.

Glossary

4WD   Four-Wheel Driven.

AMZ   Academic Motorsports Club Zurich.

ARE   Algebraic Riccati Equation.

CG   Center of Gravity.

DARPA   Defense Advanced Research Projects Agency.

DNF   Did Not Finish.

DOF   Degrees Of Freedom.

FSG   Formula Student Germany.

FSI   Formula Student Italy.

FST   Formula Student Técnico.

FS   Formula Student.

GPS   Global Positioning System.

IMU   Inertial Measurement Unit.

KLS   Kinematics Lateral Speed.

LQG   Linear Quadratic Gaussian.

LQR   Linear Quadratic Regulator.

LiDAR   Light Detection And Ranging.

MDRE   Matrix Differential Riccati Equation.

MPCC   Model Predictive Contouring Controller.

MPC   Model Predictive Control.

MSM   Modified Sliding Mode.

NED   North-East-Down.

PF   Potential Field.

PP   Pure Pursuit.

RMS   Root Mean Square.

RWD   Rear-Wheel Driven.

SAE   Society of Automotive Engineers.

xxx

Chapter 1

Introduction

In this first chapter, the motivation for this work will be described and an overview on the autonomous driving subject will be provided. The objectives of this thesis will be explained and its outline shown, as to provide a comprehensive insight of the developed work.

1.1 Motivation

Control design for autonomous driving and racing has attracted considerable attention from the research community in the last decades leading to the creation of different types of competitions where some of them aim to make a step forward in technology while others are more academic oriented.

In this last environment, the Formula Student (FS) is one of the most well-known competitions, where students are challenged to design, build and test a race car according to a specific set of rules being not only rewarded by the vehicle's performance — dynamic events — but also by management, manufacturing, design and economic aspects — static events. Having already two different competition categories, namely internal combustion engine and electrical, in an attempt to bridge technical universities with the automotive industry needs, a third one was created in 2017: driverless vehicles. However, the organisation of Formula Student Germany (FSG) has decided that, from 2022 on, all participating vehicles with person-driven prototypes should run half of the dynamic events in a self-driven configuration which means that driverless, as an independent category, will cease to exist [1]. As such, the Formula Student team from Instituto Superior Técnico - Universidade de Lisboa (FST), which has been developing cars for this competition since 2001 — first with internal combustion engines and then with electric powertrains from 2011 on — decided to focus all its efforts on the design of one hybrid prototype that allows both configurations: person-driven and driverless.

However, self-driving is a complex achievement as it requires interconnection between different subsystems, namely the sensors or cameras used to perceive the environment, the planning of the trajectory that should be performed by the car, the control strategies used and the vehicle dynamics. Focusing on planning and control, this dissertation aims to improve vehicle performance in the dynamic events of the Formula Student competitions, exploring the advantages and limitations of different algorithms.

1.2   State of the Art

In the last decades, there has been a growth in the research and investment on autonomous vehicles, also known as self-driving vehicles, for which there is a wide range of applications covering different types of systems — like small unguided robots [2] or unmanned vehicles [3] — and environments — extending from indoors to outdoors or even to planetary exploration.

Focusing on driverless cars — which are the subject of this work —, the inherent autonomy is not just "all or nothing", but rather a spectrum with six development stages defined by the Society of Automotive Engineers (SAE) in which each level describes the extent to which the vehicle can take over the tasks and responsibilities from its driver. The core competencies of this autonomy can be broadly divided into three categories, namely perception, planning and control, covering different aspects [4].

Regarding perception, this is what allows the vehicle to detect and process the environment. Making use of GPS (Global Positioning System), computer vision and a wide range of sensors [5] — which, to compensate for individual shortcomings, are usually coupled via sensor fusion — the perception algorithms are increasingly being combined with neural networks, machine learning and deep learning [6] leading to an improvement of their reliability and robustness.

From the received data, planning derives instructions for the system to act in accordance with such data and is usually categorised in: global, which considers high level objectives such as assignment of tasks and how to achieve them; behavioral, when *ad hoc* decisions are made and local objectives generated; or local, when appropriate paths and sets of actions are generated to achieve the local objective [4, 7, 8]. Regarding this last classification — the one of interest in this work — it may concern obstacle avoidance [9, 10], trajectory planning [11, 12] or path planning [7, 13]. When it comes to these last two, it is important to mention that the former requires the specification of both desired position and the time it must move to such position while the latter frequently involves a decoupled approach regarding the steering and the velocity.

Finally, control competency executes the planned actions that have been generated by the previous process. Considering the already mentioned decoupling, this execution is achieved by two different controllers — commonly designated as lateral and longitudinal controllers — giving two different input signals: a steering command and an acceleration or a braking signal, respectively. Given the existence of a continuous change in operating conditions, feedback controllers are usually implemented — which may also have a feedforward component [14] — with the assumption that the state is directly measurable or can be estimated by implementing state observers. Such traditional controllers can be classified as model-free or model-based, where the latter can be further divided into kinematic, dynamic or model predictive [15].

However, the complexity of the underlying algorithms associated with each one of the mentioned categories — perception, planning and control — is highly influenced by the scenario where the vehicle will be inserted. Comparing autonomous city driving with autonomous racing, the degree of unpredictability of the surroundings in the latter is distinctly lower which, combined with the highly controlled and regulated environment, allows for simpler approaches regarding perception that frequently rely on the com-

bination of LiDAR (Light Detection and Ranging) sensors, cameras and computer vision [16–18]. The planning is usually based on a minimum lap time problem, which accounts for the vehicle dynamics and track boundaries [19, 20]. Lastly, the control strategies used in a racing scenario frequently require more data than provided by perception, which can be acquired from motor encoders, GPS or accelerometer, for example, or from estimation [18, 21]. Furthermore, the strategies use models in which the associated degree of complexity is largely influenced by the degree of accuracy required and the available computational power. The longitudinal control problem is frequently simplified by assuming that many of the dynamics of the drivetrain, motors and transmission is regulated by low-level controllers — resulting in a fairly simple system to control, which is done mainly with linear controllers [22] — or combined with the lateral control for an appropriate MPC (Model Predictive Control) formulation [13, 23, 24]. On the other hand, lateral control tends to include the inertia of the car and tire forces — since kinematics models [25, 26] are not adequate for high-speeds — ranging from models based in the path — which may [23, 27] or may not [28, 29] involve MPC formulation —, to models based on vehicle dynamics like single-track [25, 26] or four-wheeled [22, 28] models. Similarly to what was mentioned for perception, control algorithms can be combined with learning based approaches to achieve better results.

Regarding the Formula Student competition, since the driverless category is recent, a substantial margin for improvement is still possible. However, there is one of the competing teams, namely the Academic Motorsports Club Zurich (AMZ) that stands out with a Model Predictive Contouring Controller (MPCC) — which relies on a contouring formulation to maximise the progress along the predicted horizon by minimising the lag and the contouring errors [18, 24] — showing that although driverless cars, along with the inherent technologies, still have a long way to go, remarkable progress is continuously being made.

1.3   Objectives

As previously mentioned, the autonomous vehicle pipeline involves three major components where the last two — planning and control — will be the focus of this dissertation.

Regarding planning, both path planning and obstacle avoidance fields will be addressed. For path planning, the aim is to select some of the FS dynamic events and develop the planning algorithms accordingly, where some approaches will assume that there is an *a priori* knowledge of the track layout and others will not. For obstacle avoidance, the goal is to successfully avoid collision with static obstacles. In both categories, the overall objective is to portray the expected behaviour of a human driver.

With respect to control, the objective is to develop strategies that enable the vehicle to steer and accelerate accordingly with planning, effectively driving autonomously. To this end, since a decoupled approach will be followed with the main focus on lateral control, one approach will be implemented for speed and multiples ones for steering.

Lastly, both planning and control strategies developed should be tested, evaluated and compared, in simulation, resorting to a realistic model of the vehicle — capable of accurately replicate the behaviour of a FS vehicle — in order to provide useful information about their respective performances and limitations.

1.4   Thesis Outline

This dissertation is divided into six chapters, whose contents will now be described.

In the present chapter, the motivation and objectives were presented, together with a first insight and some key-concepts regarding the subject related to this work, i.e., autonomous driving. In turn, the implementation encompasses three different chapters: Chapter 2, related with the vehicle modelling, containing the basis for the simulator and models used for validation and control design, respectively; Chapter 3, dedicated to the explanation of the problem statement — presenting the different events and environments used — as well as the algorithms developed regarding planning for each one of the simulation scenarios; and Chapter 4, in which the theoretical concepts and the models from Chapter 2 are used for designing the controllers for the lateral and longitudinal subsystems of the vehicle. The relationship between these three chapters is illustrated in Figure 1.1, which also gives a general overview of the structure adopted for simulation.
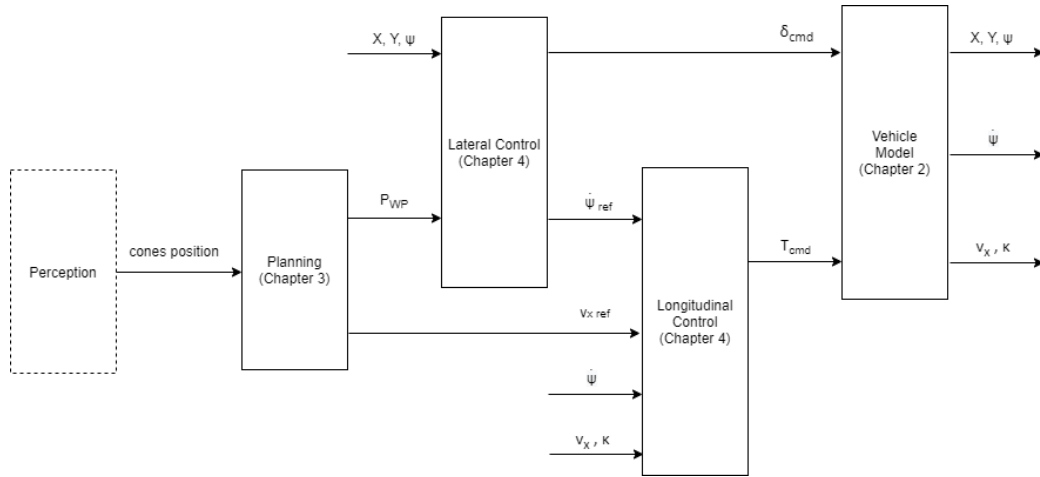
Figure 1.1: Relationship between the different topics regarding the implementation chapters. The block "Perception" is represented with a dashed line since it is out of the scope of this thesis meaning that it was assumed that computer vision algorithms correctly detects the cones. Regarding notation, the meaning of the presented variables can be found in nomenclature and they will be properly defined throughout this thesis

The multiple controllers and planning algorithms implemented were then tested, resorting to a simulation environment with a realistic model of the vehicle intended to be controlled. The results obtained, alongside with a proper analysis, are provided in Chapter 5. Finally, the conclusions of this dissertation are then presented in Chapter 6, where the achievements and shortcomings are summarised, including suggestions for future research on this topic.

Lastly, a brief remark should be made with respect to Chapters 2 and 4. Since this work was developed at the same time as [30], a connection between these two works was created due to the sharing of ideas that led to a partnership, particularly with respect to the model used for simulation and the longitudinal control. As such, the solutions implemented in this work, regarding the mentioned topics, will be based on the ones presented in [30].

Chapter 2

Vehicle Modelling

In motorsports, on-track testing opportunities are usually scarce, which makes it usual to resort to simulation to accelerate the development of a vehicle, short cutting the process of testing different algorithms.

Although the models used in such tests should provide an accurate representation of the vehicle's behaviour — usually implying a higher complexity and detail — the design of controllers for any vehicle subsystem is impractical using nonlinear, tri-dimensional and realistic vehicle models. As such, simplifications of one or more parts of the full system are frequently made and approximated models are derived, providing an intuitive platform for control design, which may employ linear or nonlinear control techniques.

In this chapter, the model used for simulation purposes is presented, as well as the derivations of the vehicle model used for design of the different controllers and estimators.

2.1   Realistic Model

As mentioned before, some considerations and simplifications are necessary for design and development — in order to diminish the overall complexity — whilst, for testing purposes, the model should be as complete as possible. As such, an adaptation from [31] was used, where the vehicle is modeled as a rigid body, with six degrees of freedom (DOF) and a vertical suspension system in each wheel, being four-wheel-driven — by independent electric motors — and front-wheel steered.

To formally describe the vehicle motion, six reference frames are used, namely the global frame — which frequently follows the North-East-Down (NED) convention, where X points North, Y East and Z Down —, the local reference frame — which coincides with the car's center of gravity (CG) with a forwards-right-down alignment — and four additional reference frames — which are attached to the tire contact patches —, all being represented in Figure 2.1.

The model formulation is done resorting to a state-space representation where the states are the linear $\mathbf{v}$ and angular Ω velocities of the CG — expressed in the local frame —, the CG position $\mathbf{p}_{CG}$ — expressed in the global frame —, the Euler angles Φ — associated with the rotations from global to
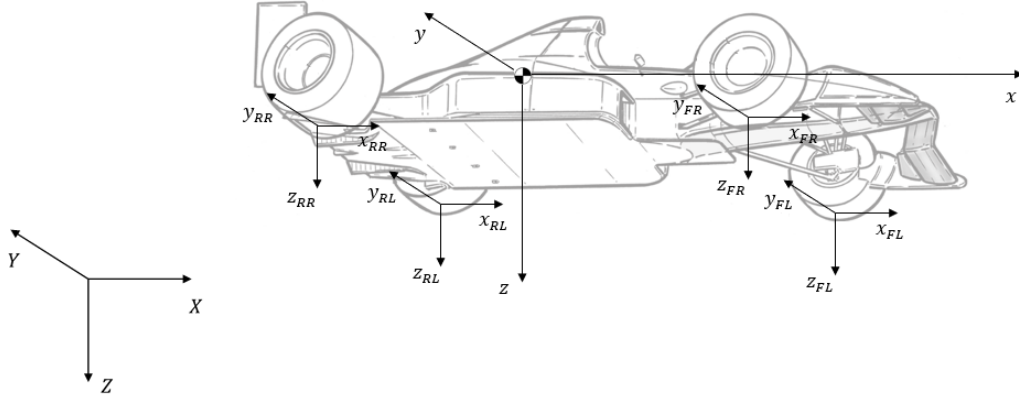
Figure 2.1: Reference frames

local frame — and the angular speeds of each wheel ω . Having as inputs the wheel torques $\mathbf{t}_w$ and the steering angles δ, the model returns the state derivatives and generates as output the suspension deformations $\boldsymbol{\Delta}_z$, the slip ratio κ, the slip angles α and the forces $\mathbf{f}_x, \mathbf{f}_y, \mathbf{f}_z$ and moments $\mathbf{m}_z$ resulting from the tire-ground interaction. Summarising:

$$\text{States:} \begin{bmatrix} \mathbf{v} & \boldsymbol{\Omega} & \mathbf{p}_{CG} & \boldsymbol{\Phi} & \omega \end{bmatrix} \tag{2.1}$$

$$\text{Inputs:} \begin{bmatrix} \mathbf{t}_w & \delta \end{bmatrix} \tag{2.2}$$

$$\text{Outputs:} \begin{bmatrix} \dot{\mathbf{v}} & \dot{\boldsymbol{\Omega}} & \dot{\mathbf{p}}_{CG} & \dot{\boldsymbol{\Phi}} & \dot{\omega} & \boldsymbol{\Delta}_z & \kappa & \alpha & \mathbf{f}_x & \mathbf{f}_y & \mathbf{f}_z & \mathbf{m}_z \end{bmatrix} \tag{2.3}$$

All the states, inputs and outputs are time-variant, but the notation (t) was dropped to simplify the reading.

Regarding the kinematics, the linear and angular velocities of the body frame can be expressed in the global frame as

$$\dot{\mathbf{p}}_{CG} = \mathbf{S}^\top \mathbf{v} \qquad \text{[m/s]} \tag{2.4}$$

$$\dot{\boldsymbol{\Phi}} = \mathbf{R}^{-1} \boldsymbol{\Omega} \qquad \text{[rad/s]} \tag{2.5}$$

where $\mathbf{R}$ stands for the transformation matrix from the Euler angles rate of change to the CG angular velocities and $\mathbf{S}$ is the rotation matrix that converts global frame coordinates into local frame coordinates. The expressions for both matrices can be found in [31].

Lastly, with respect to the dynamics, from the Newton-Euler equations the following equations can be obtained

$$m\dot{\mathbf{v}} = -m(\boldsymbol{\Omega} \times \mathbf{v}) + m\,\mathbf{S}\,\mathbf{g} + \mathbf{f}_{CG} \qquad \text{[N]} \tag{2.6}$$

$$\mathbf{J}\,\dot{\boldsymbol{\Omega}} = -(\boldsymbol{\Omega} \times \mathbf{J}\,\boldsymbol{\Omega}) + \mathbf{t}_{CG} \qquad \text{[N]} \tag{2.7}$$

$$J_w \dot{\omega} = T_w - F_x R - T_{\mathsf{dis}_w} \qquad \text{[N]} \tag{2.8}$$

where m is the vehicle mass, $\mathbf{g}$ the gravity vector, $\mathbf{J}$ and J_w are the vehicle's inertia tensor and wheel

6

rotational inertia, respectively, and R the tire radius. In the above equations, the terms with the subscript CG represent the resultant force and torque acting on the CG, which includes tire, dissipation and aerodynamics forces in (2.6) and energy dissipation in (2.7). In equation (2.8), T_{dis_w} stands for dissipation torque. All dissipations and aerodynamics forces were modeled in a quadratic form.

2.1.1 Powertrain model

Although initially FST prototypes were designed with internal combustion engines, in 2011 a shift was made to employ electric powertrains with in-wheel motors. Such prototypes can have two distinct configurations — four-wheel-driven (4WD) or rear-wheel driven (RWD) — in which each motor is independently controlled meaning that both speed and torque references can be dynamically limited [32]. The motor torque curve is sketched in Figure 2.2, for the motor speed range, where the lighter and darker curves stand for nominal operating and peak performance conditions — in which the motor can only briefly operate — respectively. This curve will be used as reference to establish maximum or limit values.
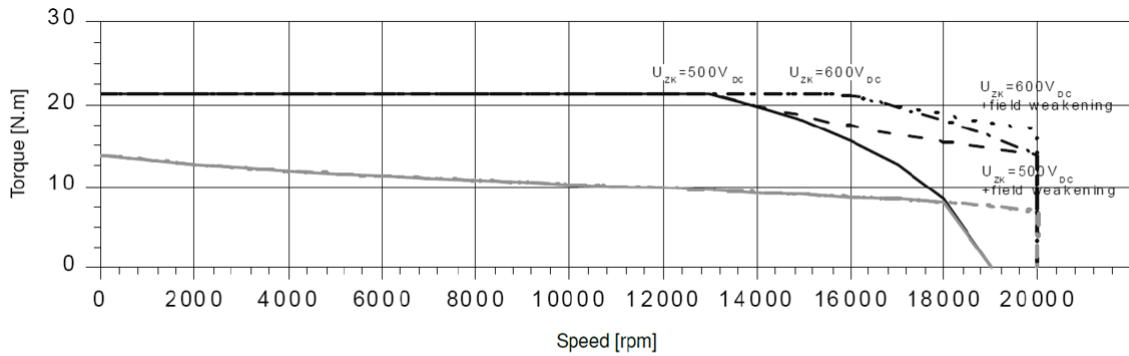
Figure 2.2: Torque curves of the electric motor [32]

Due to the complexity of modeling the full powertrain system — which encompasses the battery, inverters, eletrical connections and drivetrain — a simplification was made in which the motor losses were dynamically modeled, resorting to an efficiency map, presented in Appendix B — together with some additional information related with the motors —, and all the remaining losses were considered as constant. Based on the efficiency map, a look-up table was created — where the efficiencies in generator-operating mode can be obtained by the inverse values of the ones presented in the referenced table, for negative motor torques — allowing the determination of the motor efficiency associated with a given motor speed and torque command, by cubic interpolation between entries. The motor speed ω_m needed to perform such interpolation can be obtained from the angular speed of the corresponding wheel ω through the relation present in (2.9) in which r_{gear} stands for gear ratio.

$$\omega_m = \omega \cdot r_{\text{gear}} \qquad \text{[rad/s]} \qquad (2.9)$$

However, it should be noted that, in a real scenario, ω_m is the variable directly accessible from sensors, namely motor encoders.

7

Additionally, to approximate the torque response dynamics, the first order system

$$T = \frac{\eta_{PT}}{\tau_{PT} s + 1} T_{cmd} \qquad \text{[N·m]} \tag{2.10}$$

— where η_{PT} is an efficiency to account for the remaining losses and τ_{PT} the time constant for the torque dynamics that accounts for the electrical time constant and mechanical response — was implemented.

This modelling was inherited from [30] and was the correspondent diagram block represented in Figure 2.3.
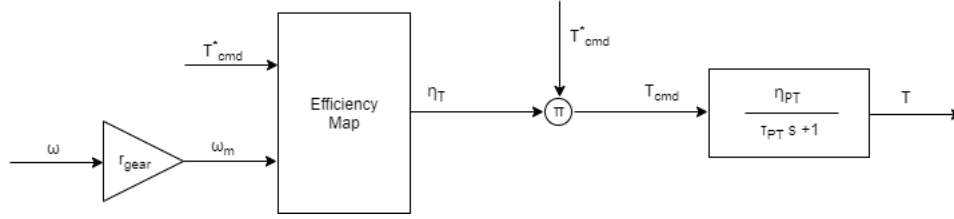
Figure 2.3: Powertrain block diagram where π stands for product

2.1.2 Steering model

The steering geometry is one of the design features influencing the race car performance, which is related with the angle between the tire moving direction and the longitudinal centerline of the vehicle. The internal operation of steering mechanisms depend on the existence of a differential that could induce different angular velocities in wheels of the same axes, as well as the geometry of the car [33].

Considering a low-speed or low curvature cornering manoeuvre, as the vehicle travels along the curved path, all tires follow unique trajectories around a shared turn center, each one with a specific curvature radius. Hence, to avoid sliding and maintain a pure rolling condition, the angle described by the inside front tire angle must be larger than the one described by the outside front tire, as represented in Figure 2.4.
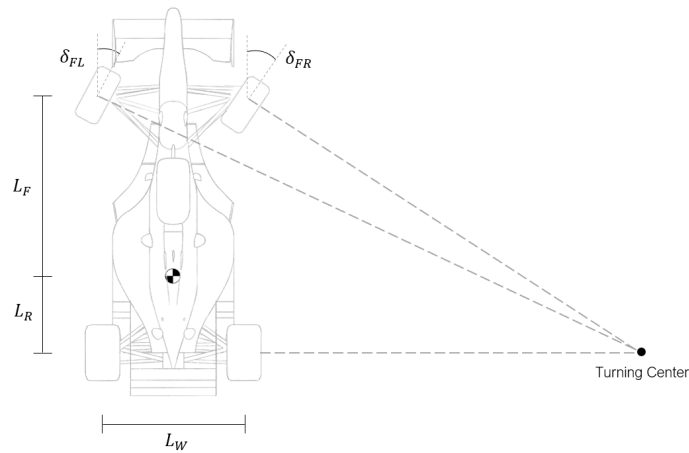
Figure 2.4: Ackermann steering ($\delta_{FL} < \delta_{FR}$)

The geometry that allows to obtain such configuration, known as Ackermann steering, computes the

8

steering angles as [22, 33]

$$\delta_{FR} = \arctan\left(\frac{L\tan(\delta)}{L - \dfrac{L_W}{2}\tan(\delta)}\right) \qquad \text{[rad]} \tag{2.11a}$$

$$\delta_{FL} = \arctan\left(\frac{L\tan(\delta)}{L + \dfrac{L_W}{2}\tan(\delta)}\right) \qquad \text{[rad]} \tag{2.11b}$$

in which $L = L_F + L_R$ and L_W are the wheelbase — sum of the distances from the CG to the front axle L_F and from the CG to the rear axle L_R — and the track width — distance between two wheels of the same axle — respectively.

The Ackermann level in a vehicle steering geometry is represented as a percentage, where 100% implies a match between the geometric low-speed turn centre and the difference in steer angle between the tires on the steerable axle, and 0% means parallel steer [34] — represented in Figure 2.5 (a). Most race cars do not run with a 100% Ackermann or a 100% anti-Ackermann steering geometry — in which the relation regarding the inner and outer steering angles is the opposite to the one described, as represented in Figure 2.5 (b) —; instead, a fine-tuning is performed and the solution lays somewhere in between, meeting specific design goals for the expected operating conditions. Notwithstanding, a 100% Ackermann geometry was considered since low-speed or low curvature cornering manoeuvre are typically found in FS race tracks [30].

(a) Parallel steering ($\delta_{FL} = \delta_{FR}$) (b) Anti-Ackermann steering ($\delta_{FL} > \delta_{FR}$)
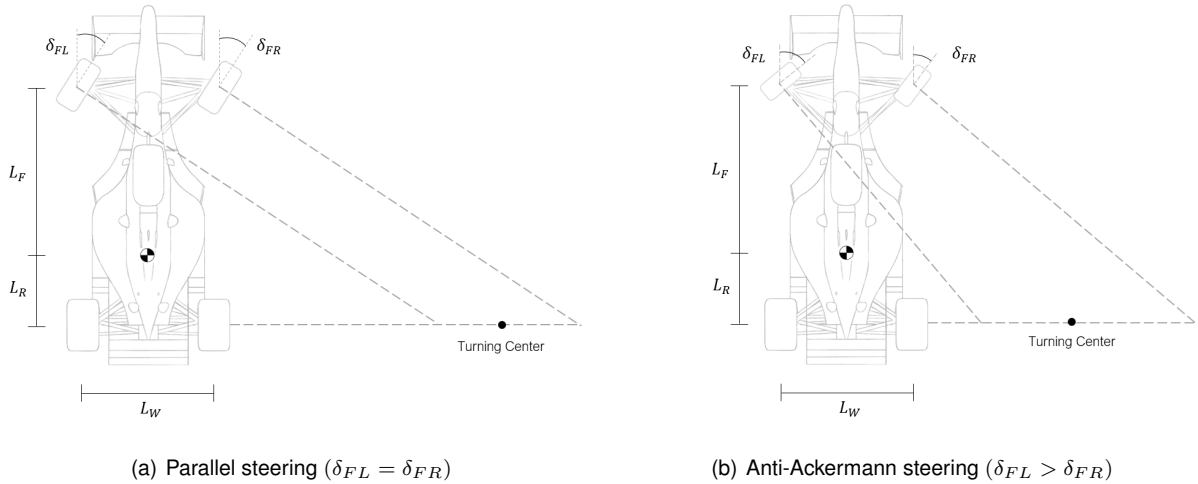
Figure 2.5: Other steering geometries

Similarly to the powertrain modelling, a first-order system was used in order to model the relation between the real and command steering angles. Such model is presented in (2.12), in which τ_{SA} stands for the steering actuation time constant.

$$\delta = \frac{1}{\tau_{SA}s + 1}\delta_{cmd} \qquad \text{[rad]} \tag{2.12}$$

Lastly, a slew rate limitation was also implemented to model the physical limit in the actuator velocity.

2.1.3 Suspension model

Since the tire forces and moments generation — which will be explained in the following section — are influenced by the vertical force acting on each tire, it is important to adequately model such force. With that purpose, a simplified suspension model was used, where each suspension quarter has an equivalent linear spring-damper system — encompassing all the components with viscous or elastic properties — that is directly actuated by tires vertical motion, normal to the ground plane and with punctual contact with the driving surface [31]. This is an approximation since, due to the vertical load, the tire-road contact is not punctual, but rather across a surface that results from the tire deformation.

For this suspension model, the vertical force is given by [30]

$$F_z = \frac{k}{r_{\text{motion}}^2}\Delta_z + \frac{c}{r_{\text{motion}}^2}\dot{\Delta}_z \qquad [\text{N}] \qquad (2.13)$$

in which k and c are the elastic and damping coefficients of the linear spring-damper systems, respectively, and r_{motion} stands for motion ratio — defined as the ratio between wheel and equivalent spring-damper system displacements, which can be obtained through kinematics relations —, introduced to correct the fact that the real suspension mechanism is not directly actuated, but through pushrods and bellcranks, as represented in Figure 2.6.
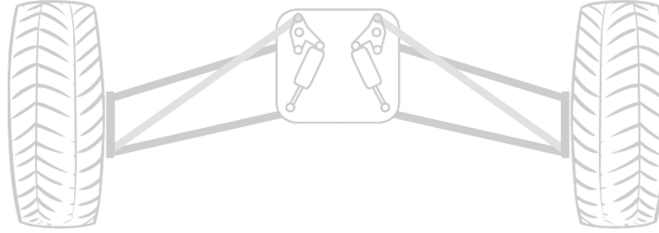
Figure 2.6: Schematics of the suspension mechanism

2.1.4 Tires model

The tires, as the only element interacting with the driving surface, are the ones responsible for the generation of the forces and moments that allow the acceleration, braking and turning of the vehicle, which are represented in Figure 2.7. Due to the inherent complexity of measuring such mechanical quantities in real time, tire models are commonly used to provide estimations, predicting the magnitude and direction of the friction forces and moments.

For this work, the Pacejka tire model [35] was considered to be suitable as it is the one used by the FST Lisboa tire supplier, Continental AG, who provided the documentation [36] to simulate tire behaviour — the boundaries for which such model is valid are presented in Appendix B. However, to be able to employ the provided tire model and compute the friction loads, several concepts must be defined first.

When a vehicle is in contact with the ground, part of the energy delivered by the motor torque is consumed by friction — in the contact patch created by the vertical load — generating a longitudinal force F_x which, opposing the wheel rotation, is responsible for the acceleration and braking of the vehicle

[31]. This force is influenced by the slip phenomenon, which can be quantified by the slip ratio

$$\kappa = \frac{\omega\, R - v_{w_x}}{v_{w_x}} \qquad \text{[-]} \qquad (2.14)$$

in which v_{w_x} represents the longitudinal component of the linear wheel velocity $\mathbf{v_w} = [v_{w_x}\ v_{w_y}\ v_{w_z}]$ in the wheel coordinate system. Analysing (2.14) it can be seen that one of three situations can occur, namely $\omega\, R < v_{w_x}$, when wheels are skidding during deceleration, $\omega\, R > v_{w_x}$, when the opposite happens, i.e, the wheels are spinning due to acceleration or $\omega\, R = 0$, when a heavy braking occurs, making the vehicle lose its desired traction.
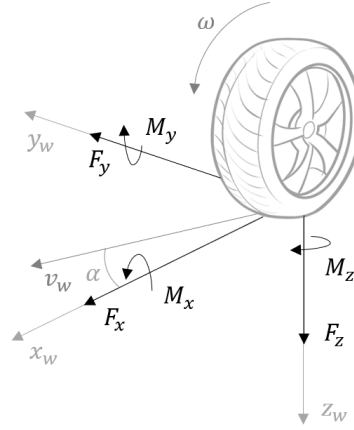
Figure 2.7: Schematics of a tire and generated forces and moments

However, it is important to note that, if the vehicle is turning, a lateral force F_y is also generated, which is influenced not by the longitudinal slip, but by the side slip, quantified by the angle presented in (2.15).

$$\alpha = \arctan\left(\frac{v_{w_y}}{v_{w_x}}\right) \qquad \text{[rad]} \qquad (2.15)$$

Given the non-uniform tire deformation that occurs in the surface originated by the tire-ground interaction — despite the model simplification of considering such interaction as punctual —, not only forces but also moments are generated. Although such moments exist along all axes, only the one known as the self-alignment moment M_z was modeled, which depends on the same parameters as the lateral force since it is generated by it.

Having been defined the concepts associated with tire mechanics, it is now possible to state the formula inherent to the chosen model. Commonly known as the Magic Formula [35], this model resorts to a semi-empirical formulation — which is presented in (2.16) — to mathematically describe not only both longitudinal and lateral forces, but also the self-alignment moment.

$$Y_{MF} - S_V = D\sin\left(C\arctan\left((1-E)B(X_{MF}+S_H) + E\arctan\left(B(X_{MF}+S_H)\right)\right)\right) \qquad (2.16)$$

Regarding the parameters inherent to (2.16), B, C, D and E are the stiffness factor, shape factor, peak value and curvature factor, respectively — which are empirically obtained and must respect the relations presented in [35] —, S_V and S_H are the vertical and horizontal shifts and, lastly, X_{MF} and Y_{MF} are the

input — which can be either κ or α — and output — which can be F_x, F_y or M_z — variables, respectively. Typical curves for this output variables, obtained from [36], are presented in Figure 2.8; the maximising values and linear ranges are defined in Appendix B.

Since both vertical force F_z and friction coefficient μ affect such curves, a normalisation was performed in order to experimentally identify the Magic Formula parameters B, C and E only once, resizing for the desired values of F_z and μ with resource to online computation of the parameter D using the following relation:

$$D = \mu \, F_z \tag{2.17}$$

(a) Longitudinal force F_x for different vertical forces F_z

(b) Lateral force F_y for different vertical forces F_z

(c) Self-alignment moment M_z for different vertical forces F_z
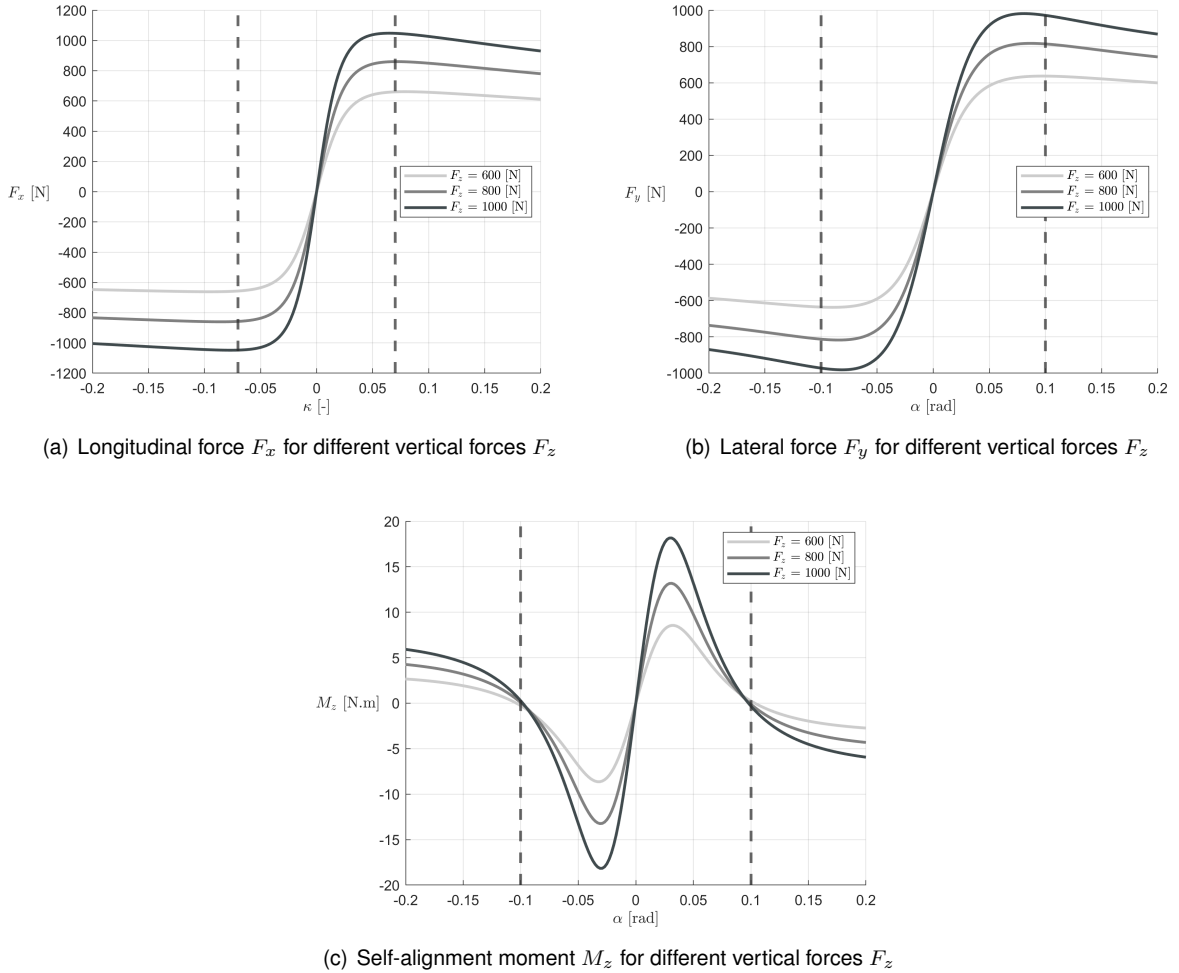
Figure 2.8: Typical pure slip curves for the Magic Formula tire model

As this formulation refers to a pure slip condition and the maximum static friction limitation is referenced to a resultant force — and not only to the longitudinal and lateral components — the concept of combined slip must be considered in order to simultaneously account for both effects.

From the slip ratio and slip angle normalisation

$$s = \frac{\kappa}{\kappa_{\text{cri}}} \qquad \text{[-]} \tag{2.18a}$$

$$a = \frac{\alpha}{\alpha_{\text{cri}}} \qquad \text{[-]} \tag{2.18b}$$

— where the subscript cri stands for critical value for which the maximum force is reached —, the normalised combined slip ρ can be obtained from

$$\rho = \sqrt{s^2 + a^2} \qquad \text{[-]} \tag{2.19}$$

allowing the rewriting of (2.16) to include such phenomenon [31]:

$$F_x = \frac{s}{\rho} D_x \sin\left(C_x \arctan\left((1 - E_x) B_x \rho \kappa_{cri} + E_x \arctan(B_x \rho \kappa_{cri}) \right) \right) \qquad \text{[N]} \tag{2.20a}$$

$$F_y = \frac{a}{\rho} D_y \sin\left(C_y \arctan\left((1 - E_y) B_y \rho \alpha_{cri} + E_y \arctan(B_y \rho \alpha_{cri}) \right) \right) \qquad \text{[N]} \tag{2.20b}$$

2.2 Simplified Models

As can be seen from the previous section, the equations of motion are complex and highly nonlinear, which would lead to an equally complex deduction of the appropriate controllers or estimators. As such, it is common to resort to a simplification of the geometrical composition of the vehicle and approximate or even neglect many of the dynamic effects, obtaining several simplified models with different degrees of complexity.

The next subsections deduce and describe four different models, three of the bicycle type — common designation for single-track models — and the unicycle model. Regarding the bicycle models, the dynamics models will be used for control and estimator design and the kinematics model for planning. From the unicycle model, the slip dynamics will be derived which, combined with the bicycle dynamics model, allows to obtain the model used for validation purposes — presented in the last subsection.

2.2.1 Bicycle Dynamics Model

In order to develop a model and understand the dynamics involved, the balance of forces and moments plays an important role. Making the assumption that the vehicle can be seen as a rigid body with planar motion regarding the steering and accelerating behaviours — which means that the vertical influences of the suspension and the pitch and roll angles of the vehicle are neglected — the dynamics can be expressed by the Newton-Euler following equations [21, 33]

$$F_{x_{CG}} = m(\dot{v}_x - \dot{\psi} v_y) \qquad \text{[N]} \tag{2.21}$$

$$F_{y_{CG}} = m(\dot{v}_y + \dot{\psi} v_x) \qquad \text{[N]} \tag{2.22}$$

$$M_{z_{CG}} = \ddot{\psi} I_{zz} \qquad \text{[N·m]} \tag{2.23}$$

where I_{zz} represents the inertia around the z axis, $[v_x \; v_y]$ the vehicle velocity components in the fixed reference frame and ψ the heading of the car, which means that $\dot{\psi}$ is the yaw rate.

The forces and moments acting upon the car CG can be identified by the free-body diagram presented in Figure 2.9 and obtained from the following equations [30]

$$F_{x_{CG}} = \sum_{i=1}^{4} \left(F_x^i \cos(\delta_i) - F_y^i \sin(\delta_i) \right) \qquad \text{[N]} \tag{2.24}$$

$$F_{y_{CG}} = \sum_{i=1}^{4} \left(F_x^i \sin(\delta_i) + F_y^i \cos(\delta_i) \right) \qquad \text{[N]} \tag{2.25}$$

$$M_{z_{CG}} = \sum_{i=1}^{4} \left(M_z^i + d_y^i \left(F_x^i \cos(\delta_i) - F_y^i \sin(\delta_i) \right) + d_x^i \left(F_x^i \sin(\delta_i) + F_y^i \cos(\delta_i) \right) \right) \qquad \text{[N·m]} \tag{2.26}$$

where d_y^i and d_x^i are the lever arms defined in Table 2.1.
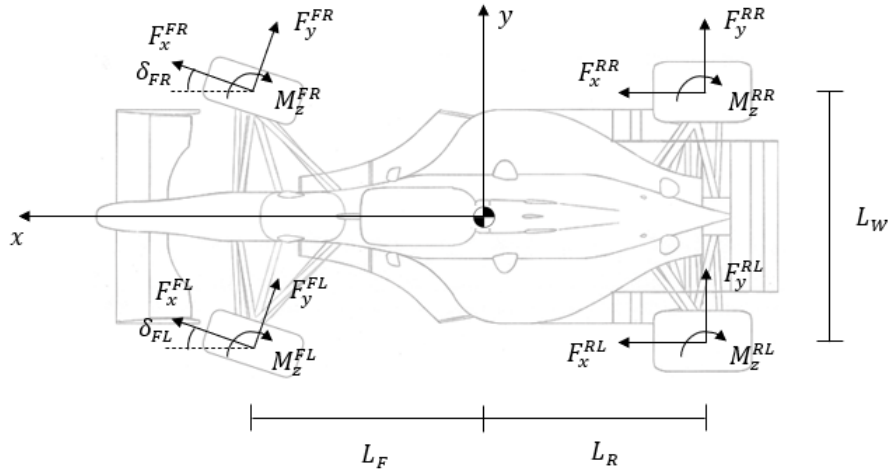
Figure 2.9: Free-body diagram for planar motion in which FL, FR, RL and RR denote for front-left, front-right, rear-left and rear-right wheels, corresponding to indexes {1, 2, 3, 4}, respectively

Table 2.1: Lever arms for M_z computation

	1	2	3	4
d_x	L_F	L_F	$-L_R$	$-L_R$
d_y	$\dfrac{L_W}{2}$	$-\dfrac{L_W}{2}$	$\dfrac{L_W}{2}$	$-\dfrac{L_W}{2}$

In addition to the forces already presented, a resistive one F_{dis} can be also considered to take into account the aerodynamic drag. Such force can be modelled as

$$F_{\text{dis}} = \frac{1}{2} \rho \, C_D A_P v^2 \qquad \text{[N]} \tag{2.27}$$

in which, ρ is the air density, C_D the aerodynamic drag coefficient, A_P the projected frontal area of the vehicle and, for simplicity, the influence of the wind was neglected.

Nevertheless, some additional assumptions can be made to further simplify the above equations. Neglecting any kind of moment created by a mechanical or electrical differential, and assuming that the

vehicle is RWD and front steered only, from the lumping of the two wheels belonging to the same axle — inherent to the bicycle model formulation, which has the free-body diagram represented in Figure 2.10 — the dynamics can be described by

$$\dot{v}_x = \frac{1}{m}\Big(-F_y^F \sin(\delta) + F_x^R - F_{\text{dis}}\Big) + v_y\dot{\psi} \qquad [\text{m/s}^2] \qquad (2.28)$$

$$\dot{v}_y = \frac{1}{m}\Big(F_y^F \cos(\delta) + F_y^R\Big) - v_x\dot{\psi} \qquad [\text{m/s}^2] \qquad (2.29)$$

$$\ddot{\psi} = \frac{1}{I_{zz}}\Big(L_F F_y^F \cos(\delta) - L_R F_y^R\Big) \qquad [\text{rad/s}^2] \qquad (2.30)$$
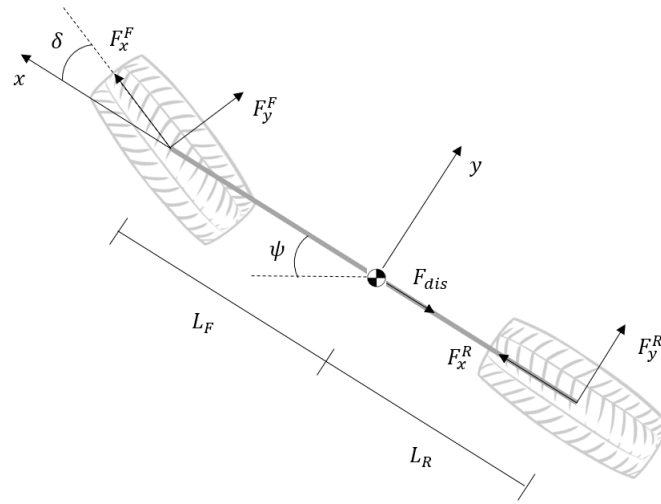
Figure 2.10: Free-body diagram for the bicycle model

From the free-body diagram and the correspondent equations, it is possible to see that a simplification was also made regarding the resistive force: although F_{dis} could exist along the x and y axes, an alignment with x was assumed.

Regarding the tire forces, the simplified Magic Formula [18] was used

$$F_x = 2D_x \sin\big(C_x \arctan(B_x\kappa)\big) \qquad [\text{N}] \qquad (2.31)$$

$$F_y = -2D_y \sin\big(C_y \arctan(B_y\alpha)\big) \qquad [\text{N}] \qquad (2.32)$$

where the factor 2 is due to the intent to model a four-wheeled vehicle and the lateral tire force is negative since it is contrary to the vehicle's movement. In this model, the slip angle α can be obtained from the car sideslip

$$\beta = \arctan\left(\frac{v_y}{v_x}\right) \qquad [\text{rad}] \qquad (2.33)$$

at the front and rear wheels through [21]

$$\alpha = \beta_w - \delta \qquad [\text{rad}] \qquad (2.34)$$

— as represented in Figure 2.11 —, in which δ is equal to zero for the rear tire and the subscript w is to denote that is at the wheel.
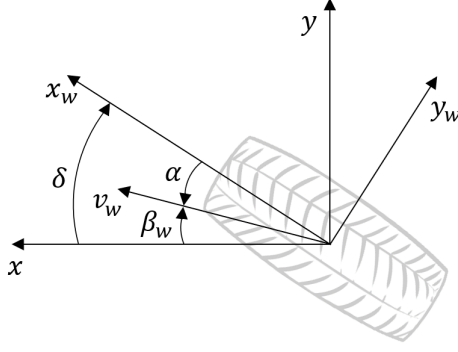
Figure 2.11: Wheel vectors. (x_w, y_w) represents the wheel referential and (x, y) the car referential

Assuming that the wheel is at a position given by $\mathbf{p}_w = [l\ 0]^\top$ with respect to the CG, where l can be either L_F or $-L_R$, the velocity components at the wheel $\mathbf{v}_w$, necessary to obtain the sideslip angles, can be achieved by [21]

$$\mathbf{v}_w = \mathbf{v} + \mathbf{\Omega} \times \mathbf{p}_w = \begin{bmatrix} v_x \\ v_y \\ 0 \end{bmatrix} + \begin{bmatrix} 0 \\ 0 \\ \dot{\psi} \end{bmatrix} \times \begin{bmatrix} l \\ 0 \\ 0 \end{bmatrix} = \begin{bmatrix} v_x \\ v_y + l\dot{\psi} \\ 0 \end{bmatrix} \qquad \text{[m/s]} \qquad (2.35)$$

which, combined with (2.33) and (2.34), allows to finally compute the slip angle as:

$$\alpha_F = \arctan\left(\frac{v_y + \dot{\psi}L_F}{v_x}\right) - \delta \qquad \text{[rad]} \qquad (2.36a)$$

$$\alpha_R = \arctan\left(\frac{v_y - \dot{\psi}L_R}{v_x}\right) \qquad \text{[rad]} \qquad (2.36b)$$

For control and estimator design, a linearisation of (2.29) and (2.30) was performed. Considering (X, Y) the position of the vehicle reference point, in the fixed frame, obtained from the integration of [33]

$$\dot{X} = v_x \cos(\psi) - v_y \sin(\psi) \qquad \text{[m/s]} \qquad (2.37)$$

$$\dot{Y} = v_x \sin(\psi) + v_y \cos(\psi) \qquad \text{[m/s]} \qquad (2.38)$$

the lateral subsystem can be represented by the following state space model [33]

$$\begin{bmatrix} \dot{Y} \\ \dot{\psi} \\ \dot{v}_y \\ \ddot{\psi} \end{bmatrix} = \begin{bmatrix} 0 & v_x & 1 & 0 \\ 0 & 0 & 0 & 1 \\ 0 & 0 & -\frac{2(C_{\alpha_F}+C_{\alpha_R})}{mv_x} & -\frac{2(C_{\alpha_R}L_R-C_{\alpha_F}L_F)}{mv_x} - v_x \\ 0 & 0 & -\frac{2(C_{\alpha_R}L_R-C_{\alpha_F}L_F)}{I_{zz}v_x} & -\frac{2(C_{\alpha_F}L_F^2+C_{\alpha_R}L_R^2)}{I_{zz}v_x} \end{bmatrix} \begin{bmatrix} Y \\ \psi \\ v_y \\ \dot{\psi} \end{bmatrix} + \begin{bmatrix} 0 \\ 0 \\ \frac{2C_{\alpha_F}}{m} \\ \frac{2L_F C_{\alpha_F}}{I_{zz}} \end{bmatrix} \delta \qquad (2.39)$$

where C_{α_F} and C_{α_R} are the cornering stiffness of the front and rear tires, assumed equal for simplicity. These parameters derive from the linearisation of the tire forces, corresponding to $B_y C_y D_y$.

16

2.2.2 Bicycle Dynamics Model in Terms of Road Errors

A dynamics model, with the lateral position and the yaw angle as degrees of freedom was presented in the previous section. However, it can be useful to define a dynamics model in terms of position and heading errors with respect to the road which, in this work, was done to obtain a model for estimator design. These errors are represented in Figure 2.12 and will be properly defined in Chapter 4.
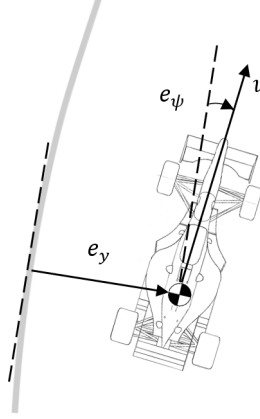
Figure 2.12: Position error e_y and heading error e_ψ in a path-following vehicle. The vehicle reference point was represented as the CG, but another location could also be considered

As the linearisation of (2.29) and (2.30) in the bicycle dynamics model — already done to obtain the state space presented in (2.39) — led to equations (2.40) and (2.41), to formulate a model in terms of road errors it is only necessary to redefine these equations in terms of such errors.

$$\dot{v}_y = -\frac{2(C_{\alpha_F} + C_{\alpha_R})}{mv_x}v_y - \frac{2(L_F C_{\alpha_F} - L_R C_{\alpha_R})}{mv_x}\dot{\psi} - v_x\dot{\psi} + \frac{2C_{\alpha_F}}{m}\delta \qquad \text{[m/s}^2\text{]} \qquad (2.40)$$

$$\ddot{\psi} = -\frac{2(L_F C_{\alpha_F} - L_R C_{\alpha_R})}{I_{zz}v_x}v_y - \frac{2(L_F^2 C_{\alpha_F} + L_R^2 C_{\alpha_R})}{I_{zz}v_x}\dot{\psi} + \frac{2L_F C_{\alpha_F}}{I_{zz}}\delta \qquad \text{[rad/s}^2\text{]} \qquad (2.41)$$

Since the inertial acceleration of the vehicle a_y have the contribution of two terms, namely the acceleration $\dot{v}_y$ due to motion along the y axis and the centripetal acceleration $v_x\dot{\psi}$, assuming steady-state conditions allows to obtain the desired acceleration as in (2.42) where $\dot{\psi}_d$ can be obtained from the turning radius R through (2.43) [28, 29].

$$a_{y_d} = v_x\dot{\psi}_d \qquad \text{[m/s}^2\text{]} \qquad (2.42)$$

$$\dot{\psi}_d = \frac{v}{R} \qquad \text{[rad/s]} \qquad (2.43)$$

With these variables defined, the errors in the lateral and yaw accelerations can be computed as [28, 29]

$$\ddot{e}_y = a_y - a_{y_d} = \dot{v}_y + v_x(\dot{\psi} - \dot{\psi}_d) \qquad \text{[m/s}^2\text{]} \qquad (2.44)$$

$$\ddot{e}_\psi = \ddot{\psi} - \ddot{\psi}_d \qquad \text{[rad/s}^2\text{]} \qquad (2.45)$$

Lastly, since it is possible to know the turning radius from the velocity and steering angle of the car and knowing the vehicle's under-steer gradient K_u and wheelbase L, the desired yaw rate can be

rewritten as [37]

$$\dot{\psi}_d = \frac{v}{L + K_u v^2}\delta \qquad \text{[rad/s]} \tag{2.46}$$

Substituting (2.44), (2.45) and (2.46) in (2.40) and (2.41) — neglecting both K_u and v_y which simplifies (2.46) — the linear state space inherent to this model can be finally obtained as [28]

$$
\begin{bmatrix} \dot{e}_y \\ \ddot{e}_y \\ \dot{e}_\psi \\ \ddot{e}_\psi \end{bmatrix} =
\begin{bmatrix}
0 & 1 & 0 & 0 \\
0 & -\frac{2(C_{\alpha_F}+C_{\alpha_R})}{mv_x} & \frac{2(C_{\alpha_F}+C_{\alpha_R})}{m} & \frac{2(C_{\alpha_R}L_R-C_{\alpha_F}L_F)}{mv_x} \\
0 & 0 & 0 & 1 \\
0 & -\frac{2(C_{\alpha_F}L_F+C_{\alpha_R}L_R)}{I_{zz}v_x} & \frac{2(C_{\alpha_F}L_F-C_{\alpha_R}L_R)}{I_{zz}} & \frac{2(C_{\alpha_R}L_R^2-C_{\alpha_F}L_F^2)}{I_{zz}v_x}
\end{bmatrix}
\begin{bmatrix} e_y \\ \dot{e}_y \\ e_\psi \\ \dot{e}_\psi \end{bmatrix}
$$
$$
+ \begin{bmatrix}
0 \\
\frac{2C_{\alpha_F}}{m} - \frac{2(C_{\alpha_F}L_F-C_{\alpha_R}L_R)}{mL} - \frac{v_x^2}{L} \\
0 \\
\frac{2C_{\alpha_F}L_F}{I_{zz}} - \frac{2(C_{\alpha_F}L_F^2+C_{\alpha_R}L_R^2)}{I_{zz}L}
\end{bmatrix} \delta \tag{2.47}
$$

2.2.3 Bicycle Kinematics Model

The last model considered from the bicycle type is the kinematics model which provides a mathematical description without considering the forces that affect the motion, meaning that the equations of motion are based purely on geometric relationships [28]. This model was used for planning since a decoupled approach was considered, treating such problem as kinematics, but respecting the adherence limits — as it will be explained in Chapter 3.

Considering a kinematics model that does not take into account slip, i.e., in which $v \equiv v_x$, the nonlinear continuous time equations that describe this model in a fixed frame are

$$\dot{X} = v\cos(\psi) \qquad \text{[m/s]} \tag{2.48}$$

$$\dot{Y} = v\sin(\psi) \qquad \text{[m/s]} \tag{2.49}$$

$$\dot{\psi} = \frac{v}{L}\tan(\delta) \qquad \text{[rad/s]} \tag{2.50}$$

from which the position of the vehicle in the fixed frame can be obtained through proper integration, as well as the heading.

2.2.4 Unicycle Model

Although the previous models present two degrees of freedom, a nonlinear model with an even greater simplicity can be obtained admitting only one dimension, in which it can only accelerate and decelerate, without turning [30].

As aforementioned, the tire forces in the bicycle dynamics model were modeled recurring to the simplified Magic Formula which, for the longitudinal component, requires the knowledge of the slip ratio. As such, the unicycle model formulated in [30] was used to obtain and control κ explicitly and not as a consequence of v_x and ω.

Knowing that electric motors spin at extremely high speeds with relatively low torques, meaning that the torque at the wheel T_w can be obtained from the motor torque T through the gear ratio r_{gear}

$$T_w = T \cdot r_{\text{gear}} \qquad [\text{N·m}] \tag{2.51}$$

from a moments balance around the y axis on a wheel — taking into account the free-body diagram presented in Figure 2.13 — it is possible to obtain the following equation

$$J_w \, \dot{\omega} = -F_x R + T \cdot r_{\text{gear}} \qquad [\text{N·m}] \tag{2.52}$$

which, combined to (2.14), leads to

$$\dot{\kappa} = \frac{1}{v_x} \left(\frac{R}{J_w} \big(T \cdot r_{\text{gear}} - R F_x \big) - \dot{v}_x (1 + \kappa) \right) \qquad [s^{-1}] \tag{2.53}$$
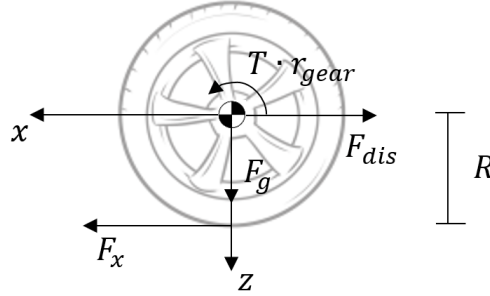
Figure 2.13: Free-body diagram for the unicycle model

2.3 Model Used for Validation

The vehicle model used for validation is an extension of the bicycle dynamics model — derived in subsection 2.2.1 — in the sense that such model allows to capture the tire-road interaction due to the introduction of the slip ratio κ as an additional state — obtained from the unicycle model. This model, summarised in equations (2.54)-(2.57), has the steering angle δ and torque T as inputs and, as states, the longitudinal v_x and lateral v_y velocities, the yaw rate $\dot{\psi}$ and the slip ratio κ.

$$\dot{v}_x = \frac{1}{m} \left(-F_y^F \sin(\delta) + F_x^R - \frac{1}{2} \rho \, C_D A_P v_x^2 \right) + v_y \dot{\psi} \qquad [\text{m/s}^2] \tag{2.54}$$

$$\dot{v}_y = \frac{1}{m} \left(F_y^F \cos(\delta) + F_y^R \right) - v_x \dot{\psi} \qquad [\text{m/s}^2] \tag{2.55}$$

$$\ddot{\psi} = \frac{1}{I_{zz}} \left(L_F F_y^F \cos(\delta) - L_R F_y^R \right) \qquad [\text{rad/s}^2] \tag{2.56}$$

$$\dot{\kappa} = \frac{1}{v_x} \left(\frac{R}{J_w} \left(T \cdot r_{\text{gear}} - R \frac{F_x}{2} \right) - \dot{v}_x (1 + \kappa) \right) \qquad [s^{-1}] \tag{2.57}$$

In these equations, the tire forces are given by the simplified Magic Formula — (2.31) and (2.32).

Chapter 3

Problem Statement and Planning Algorithms

As already stated, one of the core competencies for autonomous driving is planning, which can be categorised as global, behavioral or local — as explained in section 1.2. Being this work focused on local planning — also known as motion planning —, in this chapter the algorithms developed for path planning and obstacle avoidance will be presented. For both categories the employed strategy consists in a decoupled approach, in the sense that one algorithm guides the vehicle, accounting for the boundaries of the track — as well as the obstacles, in the obstacle avoidance scenario —, and another one regulates its speed.

For path planning, the algorithms were developed accordingly with different FS dynamical events. As such, these events will be presented first and then the procedure adopted to obtain the reference path and speed profile will be explained. For obstacle avoidance, the racing environment is maintained, but it will consist on an extrapolation of what might happen in FS competition — as it will be explained in detail in the last section. The extrapolation designation is due to the fact that, in the FS driverless category there are no other relevant actors beyond the vehicle itself and the track and the simulated obstacles are intended to represent other vehicles, which may be present in other type of racing competitions.

Regarding the algorithms, a last remark should be made: although an optimal solution or a systematic procedure can not be ensured, heuristic-based approaches were developed intending to portray the expected behaviour of a human driver and steering the solution in the correct direction.

3.1   FS Dynamic Events

As this thesis was developed on a simulation-based environment, the scenarios used for such simulation have an important role. Selecting and presenting four of the dynamic events in the FS competition, namely the acceleration, skidpad, trackdrive and autocross events [1, 38], a brief explanation will be provided in the next sections about the references used for the path and longitudinal speed, for each one of the events, as well as the why such events were chosen.

3.1.1 Acceleration

Since lateral control is the main focus of this dissertation, the acceleration event is not of a particular interest for the analysis of such behaviour. Nonetheless, it was used since it is suitable for evaluation of the longitudinal control strategy, allowing to see if such a controller — in addition to meeting the design requirements — is capable of delivering a good performance during acceleration and braking.

Assessing the vehicle's longitudinal acceleration over a seventy five metres straight, followed by a braking zone — as represented in Figure 3.1 —, this event has the velocity reference defined as a step with the first limit asymptotically coming close to $\omega_{m\,\max}$ — until the described distance is reached — and the second to $\omega_{m\,\min}$ — the stop command.
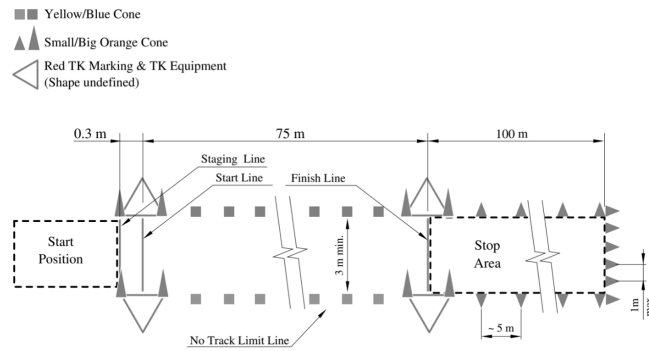
Figure 3.1: Acceleration track layout [1]

3.1.2 Skidpad

The skidpad track consists of two pairs of concentric circles in a figure of eight pattern as represented in Figure 3.2. Such event consists in the vehicle entering perpendicular to the figure eight, take two full laps on the right circle, two full laps on the left circle and then exiting perpendicular again.
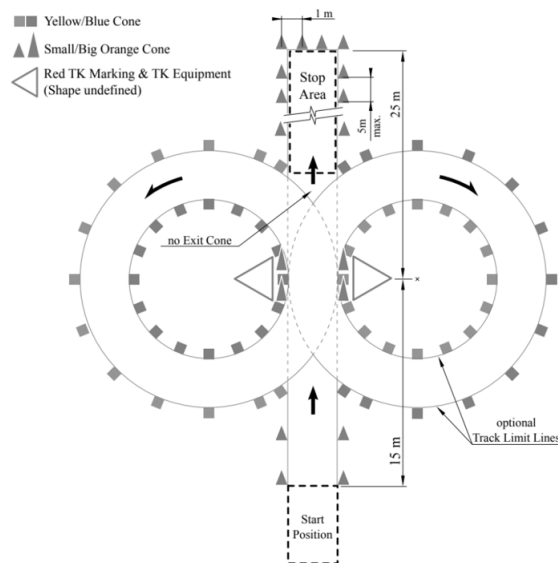
Figure 3.2: Skidpad track layout [1]

21

Since the main objective in this event is to test the lateral acceleration in stationary conditions this will be used as a preliminary evaluation of the lateral controllers, at a constant speed, using the centerline as reference path.

3.1.3 Trackdrive

More demanding than the previous ones, the trackdrive event assesses durability and reliability of the vehicle over ten laps within a given track.

Although a generic layout is presented in Figure 3.3, three specific tracks were used where the first two correspond to courses designed specially for FS driverless competitions — referred as FSG and FSI since these are from Germany and Italy competitions, respectively — and the last to a simulation track — referred as Thin since it was developed to test the performance in tight curves.
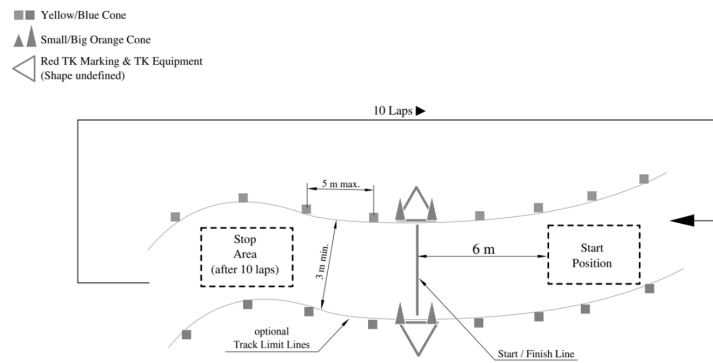
Figure 3.3: Trackdrive layout [1]

This event will be used to evaluate the combined performance of both lateral and longitudinal controllers that were developed and evaluated resorting to the previous two events. While all four events aim to minimise time, this was only consider a goal for the trackdrive event. As such — contrary to the skidpad — the centerline was not used as reference path since a considerable amount of time would be lost in curves, which could lead to significant speed decreases if the corner is sharp enough. Aiming for a more optimised reference, two approaches were developed: one resorting to a meta-heuristic algorithm — which is presented in Appendix C as it did not allow better results compared to the centerline — and another one based on the potential fields concept — which will be explained next. Regarding this solution, it should be stressed out that, although it allows the vehicle to avoid the track limits and perform a lap with indirect minimisation of distance, it can not fulfill the objective referenced, which was to finish in the minimum time possible. As such, the solution should be complemented in order to approximated the solution to the desired optimal one.

3.1.3.1 Reference Path

From the wide variety of existing algorithms and methodologies for local planning, the better known are the fictitious potential methods. Creating a representation of the space as a potential field — requiring the establishment of a danger level, for each point of the space —, such algorithms can have

22

different complexities, varying from considering only the maximum acceptable danger level [39] to taking into account both position and velocity [40] or even the dynamics of the system intended to be controlled when finding a feasible path.

In this work, the potential field concept used resorts to virtual forces, calculated considering the vehicle as a charged particle moving under the influence of repulsive potentials and attractive potentials. Since the objective is to maintain the vehicle within the track, the repulsive forces will be associated with the track boundaries, the attractive force with a target ahead and the guidance with the result of the combination of both effects.

The computation of the attractive force is quite simple since it only requires the knowledge of the actual position of the car $\mathbf{p}$ — which was obtained through the kinematics bicycle model, at a constant speed — and the selection of a target point $\mathbf{p}_{\text{target}}$. For this selection three approaches were followed where:

$\rightarrow$ a tri-dimensional space was considered in which the track has an inclination that forces the vehicle to move forward — this approach is presented in Appendix C since it was not possible to obtain feasible results from it;

$\rightarrow$ the target point is set at a fixed distance ahead, in a straight line with the vehicle orientation, in a two dimensional space, as represented in Figure 3.4 (a);

$\rightarrow$ the target point is kept at a fixed distance — by choosing a fixed number of cones ahead, which will be referenced as offset —, but lying on the centerline, as sketched in Figure 3.4 (b).

(a) Defining the target point with a straight line   (b) Defining the target point with the centerline
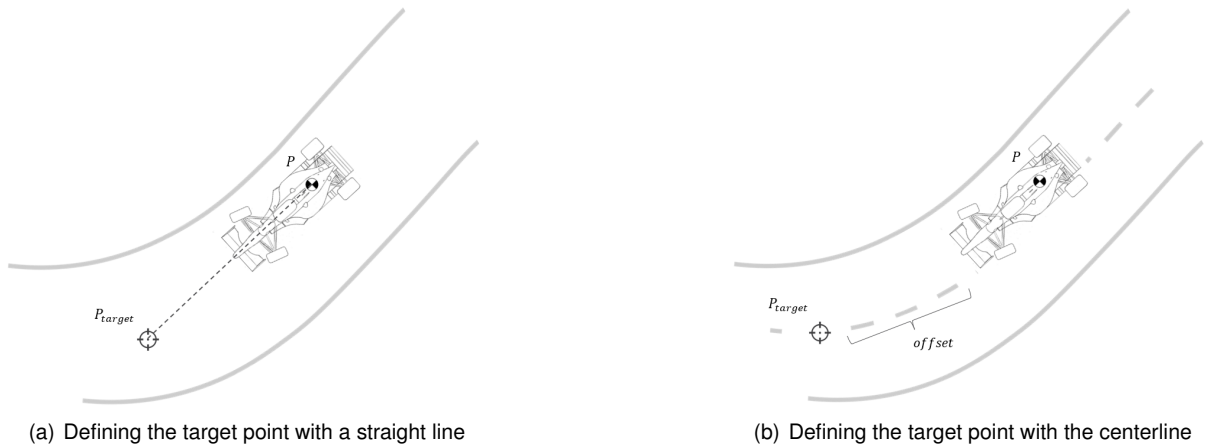
Figure 3.4: Schematics of the target point definition

This force can be mathematically described as [39]

$$\mathbf{f}_{att} = K_{att}(\mathbf{p}_{\text{target}} - \mathbf{p}) \qquad [\text{N}] \tag{3.1}$$

where K_{att} is a gain, simulating a proportional controller. This force can be thought of as similar to the popular expression "a donkey with a carrot": the target (carrot) is at a fixed distance (stick) from the car (donkey). In the situation corresponding to Figure 3.4 (a), the stick is solidary with the car, as it has no

degrees of freedom, while in situation (b) the stick has a rotation — centered on the vehicle's CG — as a degree of freedom, so that the target (carrot) can always be on the centerline. More formally, it can be seen as a spring with "infinite" stiffness since its displacement is zero.

The repulsive force, on the other hand, requires more attention as it depends on the danger level U, which is obtained from a normalised potential. This potential depends on power γ — which reflects how dangerous the boundary is, defining how fast the danger level increases in the proximity of the boundary — and on the distance between the vehicle's position and the track limits $d(X, Y)$. The danger level can be computed as [39]

$$U = \max_{k} \lim_{\gamma \to \gamma_k} \frac{d_k^{1-\gamma}(X, Y) - d_{\max}^{1-\gamma}}{d_{\min}^{1-\gamma} - d_{\max}^{1-\gamma}} \qquad [\text{-}] \qquad (3.2)$$

where $d_{\min}$ is the distance below which U will be always 1 and $d_{\max}$ the distance above which U will be always 0. Since the value of γ — which will be called decay factor — influences the potential shape — as shown in Figure 3.5 — a positive value was chosen as it allows for a better representation of the expected danger evolution.
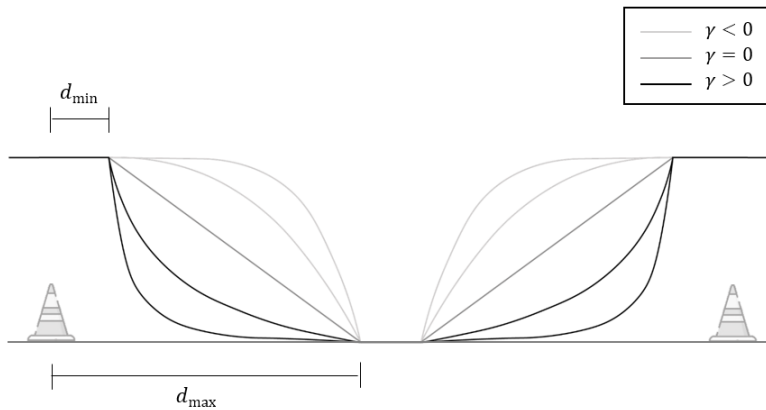
Figure 3.5: Evolution of U with d for several values of γ: the higher the value of γ the lower the danger of the boundary. In this figure, two different potential fields are represented, one for each limit. As such, U increases from bottom to top ($\uparrow$) for both limits, but d increases from left to right ($\rightarrow$) for the left limit and from right to left ($\leftarrow$) for the right limit

Analysing all the boundary points in the proximity of the vehicle, the one with the minimum distance is selected since it will present the higher danger level. From this point $\mathbf{p}_{\text{danger}}$, the repulsive force can be calculated from [39]

$$\mathbf{f}_{rep} = K_{rep} \, U \frac{\mathbf{p} - \mathbf{p}_{\text{danger}}}{\| \mathbf{p} - \mathbf{p}_{\text{danger}} \|} \qquad [\text{N}] \qquad (3.3)$$

where $\| \, . \, \|$ stands for the Euclidean norm of the respective vector and K_{rep} is a gain, as in the attractive force.

Seeing the virtual resultant force $\mathbf{f}$ direction as a desired orientation — since it minimises the potential — and knowing the current heading of the vehicle ψ, an heading error e_ψ can be defined as shown in Figure 3.6. The steering command intends to drive this error to 0 meaning that this is a regulator problem; thus, the steering command was set equal to the error. In this way, the vehicle is steered in the direction of the resultant force. This law could seem extremely simple, since it results from a unitary proportional controller, but it should be kept in mind that the reasoning behind the heading error used to

obtain this control action involves highly nonlinear calculations.
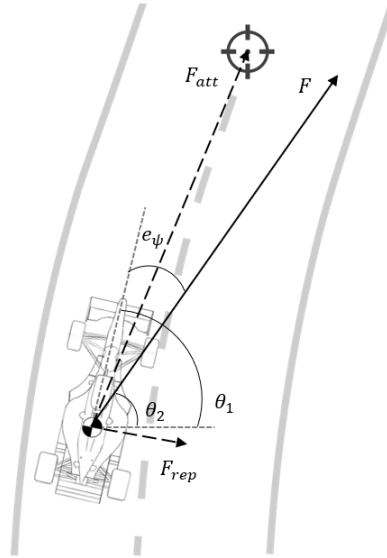
Figure 3.6: Schematic of the forces felt by the vehicle

The procedure overview is summarised in Figure 3.7.
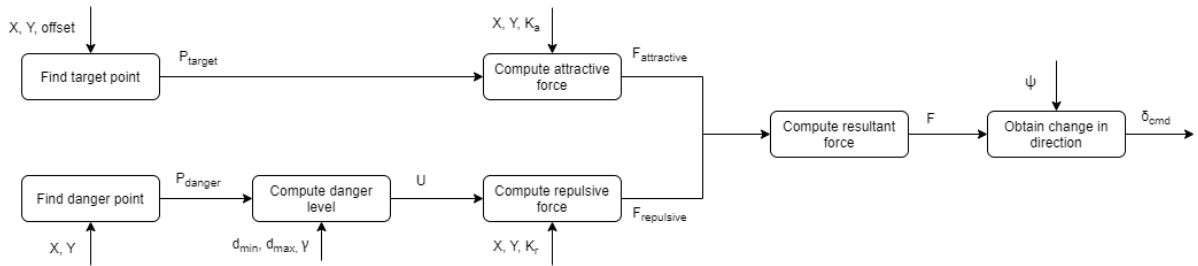
Figure 3.7: Schematic of the process based on the artificial potential field approach

From this approach different paths can be obtained, for the same track, as result of different combinations of the inherent parameters. As such, on its own, it is not able to guarantee an optimal solution, in the sense of guaranteeing the completion of the course with minimum time. To obtain such solution, the formulation of a cost function, relating parameters K_{att}, K_{rep} and γ with time, is needed. However, this requires a study on how a unitary change on each one of these parameters influences the time spent or is related with it, which can be time consuming and complex. Hence, a simpler approach was followed where the obtained solution is not optimal, but is steered in this direction: the method represented in Figure 3.4 (b) — since the one in Figure 3.4 (a) led to unsatisfactory results, as it will be presented and explained in Chapter 5 — was combined with the speed algorithm that will be presented next, in order to obtain the set of parameters that will result in a solution close to the optimal.

The procedure adopted in such search is presented in Algorithm 1, where it is possible to see that a sweep was performed for the offset, K_{rep} and γ parameters. K_{att} was left out and set to a unitary value since, although it can also be seen as parameter, it is related with the offset. Establishing, for each one of these variables, the range for analysis — which consists in all the values, with a step p, between 1

25

and a defined limit — the sweep is performed by running the simulation, i.e., generating a path, for each combination. Since some combinations of parameters can lead to unfeasible paths, the validity of the solution is checked resorting to a function that verifies if the car could navigate the path without crossing the boundaries of the track or touching the cones. Finally, for all the valid paths, the speed profile is found. This allowed to find, from all the feasible paths generated from the different combinations, the one that lead to the lowest time, which will be chosen as reference.

Algorithm 1: Sweeping procedure

Input: offset$_{\text{lim}}$, p, γ_{lim}, $K_{r_{\text{lim}}}$
Output: offset, γ, K_{rep}
for *offset* $\leftarrow 1 : p : offset_{lim}$ **do**
    for $\gamma \leftarrow 1 : p : \gamma_{lim}$ **do**
        for $K_{rep} \leftarrow 1 : p : K_{rep_{lim}}$ **do**
            path $\leftarrow$ Run Simulation;
            validity $\leftarrow$ check_validity(path, limits);
            if *validity == true* **then**
                $t \leftarrow$ speed_profile (path);
            else
                $t \leftarrow$ NaN;
            end
        end
    end
end
[offset, γ, K_{rep}] $\leftarrow$ find_parameters(t)

3.1.3.2 Speed Profile

Although approaches capable of simultaneously optimising both the path and the speed profile exist, the procedure taken was based on aiming to find a speed profile that results in complete a given fixed path — the one obtained with the artificial potential field method — in minimum time [41] respecting traction conditions and powertrain constraints.

Considering an isotropic tire, the maximum transferable force between the road and the vehicle is limited by the tire force which, using the friction circle model, can be computed from

$$F_x^2 + F_y^2 \leqslant (\mu F_z)^2 \qquad [\text{N}^2] \tag{3.4}$$

Neglecting the aerodynamic downforce, the forces in (3.4) are given by

$$F_x = ma_x + \frac{1}{2}\rho A_p C_D v_x^2 = ma_x + F_{\text{dis}} \qquad [\text{N}] \tag{3.5a}$$

$$F_y = mv_x^2 K \qquad [\text{N}] \tag{3.5b}$$

$$F_z = mg \qquad [\text{N}] \tag{3.5c}$$

where K stands for the path curvature obtained through

$$K = \frac{X'Y'' - Y'X''}{((X')^2 + (Y')^2)^{\frac{3}{2}}} \qquad [\text{m}^{-1}] \tag{3.6}$$

In (3.6), the single and double apostrophes denote the first and second derivatives, respectively, of the waypoints coordinates (X, Y) expressed in the global frame. These derivatives can be approximated using forward, backward and central differences in starting, finishing and remaining points, respectively.

Discretising the path at N steps, using a fixed step Δs in arc length s, and performing algebraic manipulation — which can be seen with more detail in [41] — of the equations for uniformly accelerated motion

$$v_x(k+1) = v_x(k) + a(k)\Delta t \qquad [\text{m/s}] \tag{3.7a}$$

$$s(k+1) = s(k) + v_x(k)\Delta t + \frac{1}{2}a(k)(\Delta t)^2 = s(k) + \Delta s \qquad [\text{m}] \tag{3.7b}$$

it is possible to obtain the following equations

$$\Delta s = \frac{v_x^2(k+1) - v_x^2(k)}{2a(k)} \qquad [\text{m}] \tag{3.8}$$

$$v_x(k+1) = \sqrt{v_x^2(k) + 2a(k)\Delta s} \qquad [\text{m/s}] \tag{3.9}$$

$$t(k+1) = t(k) + \frac{2\Delta s}{v_x(k+1) + v_x(k)} \qquad [\text{s}] \tag{3.10}$$

which will be used in the optimisation process. This optimisation is split into two passes, a backward and a forward one, both explained below.

Backward Pass

Algorithm 2: Backward pass

Input: $K(k)$, $v_{x_{\text{lim}}}$, Δs
Output: $v_{x_{\text{bwd}}}(k)$, $v_{x_{\text{max}}}(k)$
$k \leftarrow \text{length}(N)$;
$v_{x_{\text{bwd}}}(k) \leftarrow v_{x_{\text{lim}}}$;
while $k > 1$ **do**
    $v_{x_{\text{max}}}(k-1) \leftarrow$ solution of eq.(3.4) for $K(k-1)$;
    $v_{x_{\text{max}}}(k-1) \leftarrow \min(v_{x_{\text{max}}}(k-1), v_{x_{\text{lim}}})$;
    $a_{\text{lim}} \leftarrow [v_{x_{\text{max}}}^2(k-1) - v_{x_{\text{bwd}}}^2(k)]/(2\Delta s)$;   // (3.8)
    $a(k-1) \leftarrow -h(K(k), v_{x_{\text{bwd}}}(k), -1)$;   // (3.13)
    $a(k-1) \leftarrow \min(a(k-1), a_{\text{min}})$;
    $v_{x_{\text{bwd}}}(k-1) \leftarrow \sqrt{v_{x_{\text{bwd}}}^2(k) + 2a(k-1)\Delta s}$;   // (3.9)
    $k \leftarrow (k-1)$;
end

Being the first pass, the backward algorithm determines the maximum speed in turns and the necessary braking distance before each turn.

Starting from the finishing point and iterating the sampled curve in the reverse order, the maximum speed at each step is obtained from the minimum between a user-defined limit $v_{x_{\text{lim}}}$ and the maximum

speed for the previous sample $v_{x_{\max}}(k-1)$, which corresponds to the maximum admissible speed by the friction circle, i.e., the one obtained by taking the real positive solution of (3.4), solved for $K(k-1)$ and $a_x = 0$. Once the minimum between the two speeds, at step $(k-1)$, is computed, the negative acceleration required to achieve such value can be determined resorting to (3.8). However, since the maximum available braking deceleration — given by function h that will be described later — could be lower, this acceleration is also determined and the minimum of the two is applied. Having been computed both speed and acceleration, the next iteration continues by moving backward along the curve.

This pass is summarised in Algorithm 2, where it is important to note that $a(k)$ is taken as positive due to integration backward in time [41].

Forward Pass

Algorithm 3: Forward pass

Input: $K(k)$, $v_{x_{\text{bwd}}}$, Δs, v_{x_0}
Output: $v_{x_{\text{fwd}}}(k)$, $a(k)$, $t(k)$
$k \leftarrow 1$;
$t(k) \leftarrow 0$;
$v_{x_{\text{fwd}}}(k) \leftarrow v_{x_0}$;
while $k < N$ **do**
     $a_{\text{lim}} \leftarrow [v_{x_{\text{bwd}}}^2(k+1) - v_{x_{\text{fwd}}}^2(k)]/(2\Delta s)$;   // (3.8)
     $a(k) \leftarrow h(K(k), v_{x_{\text{bwd}}}(k), 1)$;   // (3.13)
     $a(k) \leftarrow \min(a(k), a_{\text{lim}})$;
     $v_{x_{\text{bwd}}}(k+1) \leftarrow \sqrt{v_{x_{\text{fwd}}}^2(k) + 2a(k)\Delta s}$;   // (3.9)
     $t(+1) \leftarrow t(k) + 2\Delta s[v_{x_{\text{bwd}}}(k+1) + V_{x_{\text{bwd}}}(k)]^{-1}$;   // (3.10)
     $k \leftarrow (k+1)$;
end

In the second pass, the forward algorithm maximises the speed and determines the optimal times of transition between acceleration and braking, allowing for the generation of the time-optimal speed $v_{x_{\text{fwd}}}(k)$ and acceleration $a(k)$ profiles. This is done reparametrising the original profile using time steps, instead of distance steps, forming a trajectory parametrised in time [41].

Beginning in the starting point, and iterating in the forward order, when the speed is below the speed profile $v_{x_{\text{bwd}}}(k)$ of the backward pass, the maximum available positive acceleration is applied to increase the speed and, once $v_{x_{\text{bwd}}}(k)$ is reached, the optimal braking is applied as in $v_{x_{\text{bwd}}}(k)$ [41]. As a result, the optimal transition times between acceleration and braking are determined to execute the track in minimum time and under acceleration constraints resulting from traction and/or powertrain. The described iterative scheme results in a bang-bang type of trajectory, applying the maximum available input at each step with a single change of input polarity per one turn [41].

The steps of this procedure are summarised in Algorithm 3.

Powertrain Constraint

From the presented algorithms, it is possible to see that both passes use a function h to determine the maximum available longitudinal acceleration in direction $d = \pm 1$, with forward represented as posi-

tive. Using K and v_x, such acceleration, based on the maximum available tire force in the longitudinal direction, is determined from (3.4) as

$$a_x = \frac{1}{m}(dF_x - F_{\text{dis}}) = \frac{1}{m}\left(d\sqrt{\mu^2 F_z^2 - F_y^2} - F_{\text{dis}}\right) \qquad [\text{m/s}^2] \qquad (3.11)$$

where Fy and Fz are given by (3.5b) and (3.5b), respectively. However, this value is further limited by the vehicle powertrain [41].

From the torque-speed curve of the motor — presented in Figure 2.2 — it is visible that the torques can be approximated as constant until entering the zero-torque/zero-power zone. So, the operational range was limited before this phenomenon and a simplification was made in which the available torque T is modelled as constant and transformed into wheel tractive force F_{trc} through

$$F_{\text{trc}} = \frac{1}{R} \sum_{i=1}^{N_{\text{mtr}}} \left(\eta_{i,trans} \cdot r_{\text{gear}} \cdot T_i\right) \qquad [\text{N}] \qquad (3.12)$$

where $\eta_{i,trans}$ is the transmission efficiency. This torque differs, however, depending on the axle and on whether the vehicle is braking or accelerating.

The maximum available longitudinal acceleration is then given by

$$h = \begin{cases} \frac{1}{m}\left[-F_{\text{dis}} + \min\left(\sqrt{\mu^2 F_z^2 - F_y^2}, F_{\text{trc}}\right) \right] & \text{if } d = 1 \\ \frac{1}{m}\left[-F_{\text{dis}} - \min\left(\sqrt{\mu^2 F_z^2 - F_y^2}, |F_{\text{trc}}|\right) \right] & \text{if } d = -1 \end{cases} \qquad [\text{m/s}^2] \qquad (3.13)$$

which is different from the one presented in [41] since the motors can work as generator, allowing for electrical braking.

3.1.4 Autocross

The last event that will be approached is autocross which, generally, consists on a five hundred meters lap over a track with straights, turns and chicanes, assessing peak driving performance. However, for the driverless category, the track's layout is the same as the one used for the trackdrive [38], meaning that it can thought as a shorter version of such event.

Since the approach followed for the trackdrive event requires an *a priori* knowledge about the track to find a more optimise path and to obtain the speed profile — which requires the path to have been previously obtained — the autocross will be used to perform the mapping. Due to the inherent complexity of performing an optimisation over a finite horizon to obtain a local optimal trajectory — that accounts for the track limits and the vehicle dynamics —, specially since no reference path obtained offline could be used, a simpler approach was followed decoupling, one again, the path and the speed profile.

With respect to the reference path, the artificial potential field was used once again since the guidance depends only on the local environment of the vehicle, which is available online. Furthermore, the smoothness of the curve obtained with potential field methods makes practical steering and speed control possible [40]. The required parameters — namely the offset, the decay factor and the repulsive gain

— can be established through a conservative guess. This guess could be "steered in the right direction", since a track walk prior to the event is performed with access to analog measurement devices, which allows to obtain information that could be used in such guess.

However, the reference for speed needs to be obtained with a different method since, as mentioned, the previous approach requires the path to have been previously found. To obtain a speed profile in an online fashion, two distinct methods were developed to replace the one already presented: one in which the speed is regulated according to the curvature of the centerline; and another one resorting to the safety zones concept. None of the approaches can guarantee the determination of an optimal solution, but they were developed in a heuristic way and based on expert knowledge, which allows to simulate the expected behaviour of a driver as it will be explained next.

Centerline Approach

In the first method, a simple approach was followed where the reference speed was obtained from a centerline point, respecting the friction circle restriction — given by equation (3.4), with the associated curvature computed from (3.6). This seemed a good initial method to obtain the speed profile since the centerline is a frequent reference in this type of competitions.

Thinking as a human driver, an anticipation is needed to regulate the speed, which is usually achieved by looking a given distance ahead. However, in an intuitive manner, this predictive distance should depend on both speed and curvature since, while turning, the tendency is to shorten such distance. Thus, the selection of the reference centerline point must be done with this in mind and the speed regulation must take into account both the curvature in the reference point set by the look-ahead distance and in the current point: if the latter is higher, that must mean that even if a straight line will follow, a turn is being made and, as such, the look-ahead distance must be decreased. The correction in this distance is made by linear interpolation — considering the current curvature and a benchmark for a straight and a tight curve — and the speed is obtained from this new reference point — as represented in Figure 3.8.
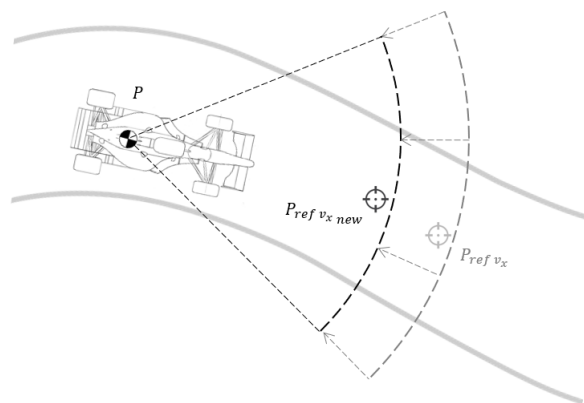
Figure 3.8: Schematics of the look-ahead decrease

Since each team has at least two runs consisting of one single lap [38], for the second run the reference speed can be obtained computing the curvatures from the path previously described — instead

of considering once again the centerline — as it will allow for a faster run due to the presence of lower curvatures.

Critical Radius Approach

Since the previous approach leads to a conservative speed profile, due to the fact that the actual described curvature can be significantly lower than the one computed from the centerline, another method was developed based on the concept of safety zones.

Taking into account that any electromechanical system has an inherent response time, the ability of a system to respond to a sudden obstacle can be derived from the concept of vehicle safety and translated into the definition of multiple zones within the system observable environment [42, 43] — which is limited by the sensors' range. Such zones are four — the observation, warning, danger and critical zones — and are represented in Figure 3.9.
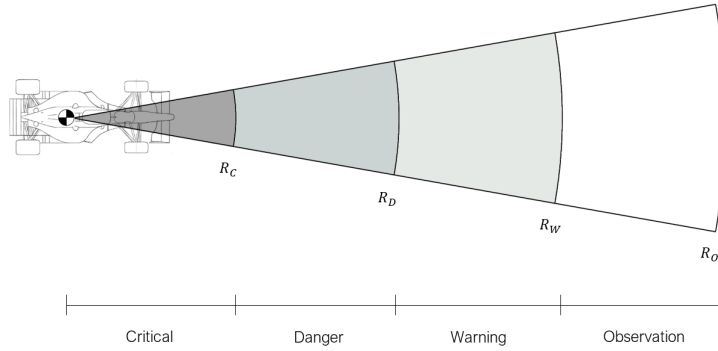
Figure 3.9: Detection zones

These regions are responsible for the velocity adjustment needed to avoid collision and a general influence of the obstacle detection in the reference velocity is represented in Figure 3.10 (a).

(a) General profile

(b) Adapted profile
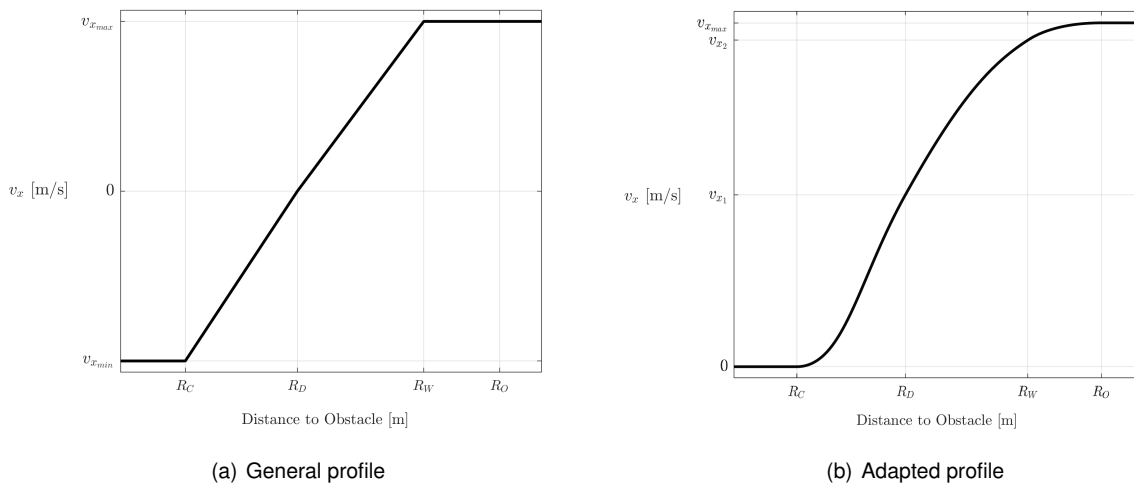
Figure 3.10: Relation between velocity and distance

From this figure, it is possible to see that the reference velocity for a distance higher than the maximum detection distance R_O, or within the observation zone, is only limited by a defined maximum

31

velocity v_{x_max}. However, below the warning radius R_W, the velocity is reduced until it becomes zero, which happens while entering in the danger zone at R_D. In this situation, the vehicle is forced to move away from the obstacle. Lastly, in the critical zone — where R_C contains the vehicle with an extra safety distance — if an obstacle is detected, the vehicle moves away at a velocity v_{x_min}.

Although the approach implemented was based on this concept [42, 43], two changes were made, regarding the velocity profile, due to the environment in which it will be used. The first change is associated with the negative reference velocity. Since this is not allowed, it requires changing the breakpoints associated with R_D and R_C. With this change, the critical zone corresponds to the region where the vehicle is forced to stop, and entering the danger zone is associated with a chosen velocity v_{x_1}. The last modification is related with the shape of the profile since a linear piece-wise reference velocity could lead to chattering. So, a cubic spline interpolation was performed allowing a smooth transition between regions. To avoid an "overshoot" in the observation zone, the breakpoint associated with R_W was slightly decreased from v_{x_max}. This will produce a slight decrease in velocity in the observation zone — which is not typical when using this concept —, but it was not considered significant if the different between the velocity of this breakpoint v_{x_2} and v_{x_max} was less or equal to 3 [m/s]. The general profile with these adaptations is presented in Figure 3.10 (b).

One last alteration, regarding the definitions of the radius, was also made. Being usually fixed, in this approach it is advantageous to have the radius changing with the velocity — taking into account that the observation radius can never be higher than the maximum distance from the sensor range — in order to allow for a higher anticipation in higher velocities.

Nevertheless, one should keep in mind that this adapted profile can be easily extrapolated to obtain the more general one and combined once again with the artificial potential fields method to be applicable in more different and generic scenarios. For that, it is only necessary to change the breakpoints used to obtain the velocity profile and consider an attractive force pointing backwards when the velocity is negative.

3.2 Obstacle Avoidance

Obstacle avoidance, the last field of path planning approached in this work, is one of the subjects with central interest in autonomous driving. Since the obstacles to be avoided are unpredictable and present dynamic behaviour in many situations, the inherent lack of certainty regarding the environment introduces the need of using local path planning techniques rather than global ones [9].

In racing situations, due to the reduced number of degrees of freedom, this problem is simplified or non-existant at all. In some competitions, like the Defense Advanced Research Projects Agency (DARPA) Challenges, when a faster vehicle overtakes a slower one, the latter is paused, allowing the faster to pass it as if it were a static obstacle, eliminating the need for the vehicles to handle the case of dynamic passing [44]; however, in FS competitions only one vehicle is allowed on track.

As in the person-driven categories of the FS competition something similar happens — where the slower vehicle is forced to swerve —, in the case of allowing for more than one vehicle to run simultane-

ously, the situation is likely to be dealt with in the same way. As such, the environment presented in this section will consist on an extrapolation of what might happen in FS competion, but is already happening in some of the racing scenarios.

Regarding the tracks used for simulation, as the ones from the FS dynamic events are relatively narrow — not allowing enough space for maneuvers —, three different tracks were created with the obstacles placed at strategic positions in order to test the robustness of the algorithm. The layout of the first track is similar to the one present in athletics tracks, being its simplicity due to the fact that such track was used to get a first insight about the functioning of the algorithm, as well as of eventual problems. The other ones were obtained from the work related with [13, 24] and resized since such tracks were originally developed for scaled prototypes.

Lastly, with respect to the approach developed, a decoupling between the guidance and acceleration was followed once again. To obtain the reference speed, the same methodology used in the autocross event — the critical radius approach — was applied. However, an addition was made since, due to the obstacles presence, it can occur that there is no possible passage and, consequently, the vehicle is forced to stop. So, if such a situation is detected, the reference speed is set to zero. For the guidance, resorting once again to potential fields methods — and being intuitive to bypass the obstacle through the widest passageway — the algorithm was built to take into account four main scenarios, namely the wider passage being free, the wider passage being obstructed, no wider passage and, lastly, no passage at all, as represented in Figure 3.11.

(a) Wider passage free   (b) Wider passage obstructed   (c) Equally wide passages   (d) No possible passage
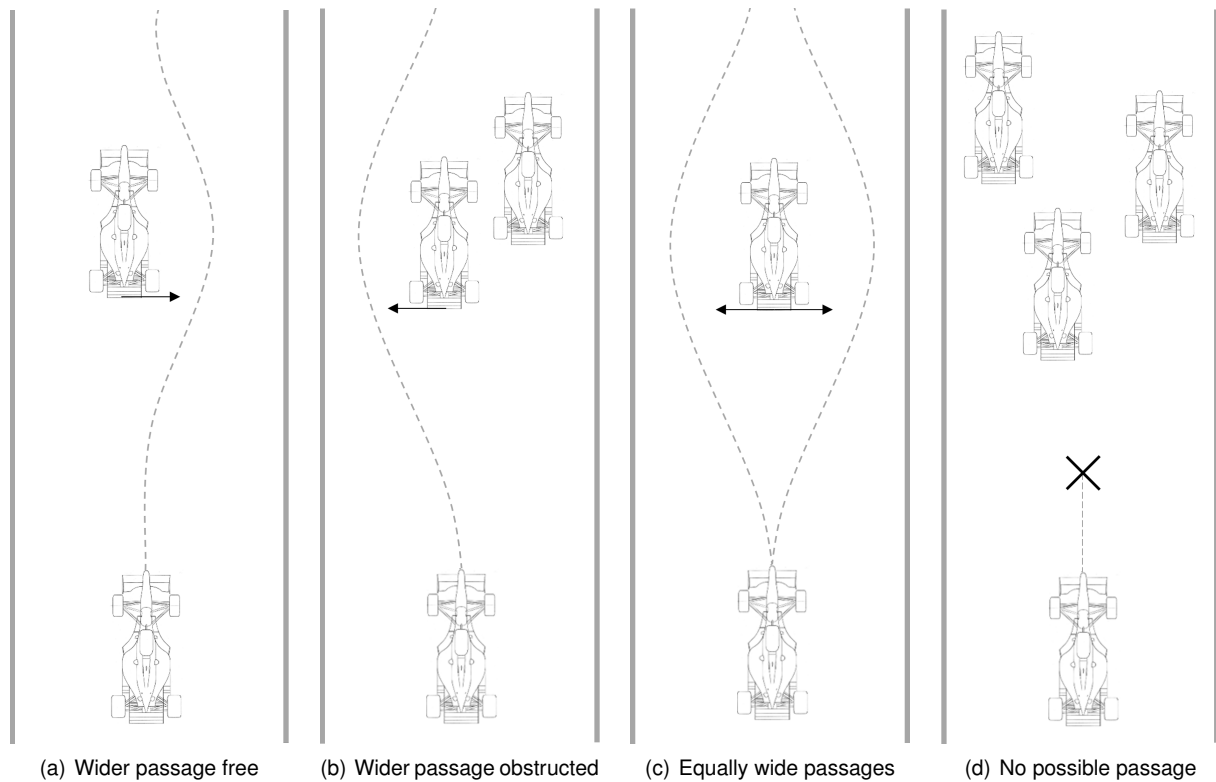
Figure 3.11: Scenarios taken into account with the obstacle avoidance algorithm

For simplification, the vehicles were modelled as rectangles. Such geometric form was selected —

33

instead of using ellipse, which could account for uncertainty regarding the position — as there is a significant resemblance between the two and the rectangle can symbolise a bounding box, providing an extra safety.

However, from the definition of the repulsive potential field — given by (3.2) — and knowing that the repulsive force will have a direction perpendicular to the potential field that originated it, some problems can be anticipated. These situations could probably be solved by a coupled approach, where the velocity direction is taken into account to define or influence the danger and/or the repulsion direction, but a method based only on distance was followed instead.

The modifications performed to the standard concept of the potential field methods will be explained next. The first two were implemented in order to anticipate any problems that could arise and the last one was implemented as a extra safety measure.

Distinction between track limits and obstacles

From (3.3) and (3.2) it is possible to see that the repulsive force is given by the maximum danger of all the accounted obstacles. However, such formulation can lead to a vehicle's response that is not sufficiently anticipatory in the face of an obstacle.

Suppose that the vehicle is at the middle of the track — meaning that there is no repulsion felt from the limits — and some obstacle exists ahead. The obstacle will only be prioritised — to compute the repulsive force — when the distance thereto will be less than half of the track width, which may lead to not enough anticipation to guarantee a collision-free overtake. As such, a distinction between the track limits and the remaining obstacles — intended to simulate other vehicles — must be made. For that, two threshold distances — one for the track limits and another for the obstacles — were implemented, "switching" the prioritising between them. Due to this decoupling, the parameters associated with (3.2) — $d_{\max}$, $d_{\min}$ and γ — and (3.3) — K_{rep} — were set to different values for the limits and the obstacles.

Changing the direction of repulsion on obstacles

In the usual potential field approach, the repulsive force direction is perpendicular to the contour lines from the different danger levels around the obstacles. This could lead to oscillatory behaviour when the vehicle and the obstacle are aligned — as represented in [39]. To prevent this problem, the direction of the repulsive force associated with the obstacles was changed and set parallel to the closest edge — as mentioned, the vehicles were approximated to rectangles — pointing towards the wider passage and in the opposite direction in the case of obstruction. In addition to prevent the referenced problem, this modification — which is represented in Figure 3.12 — also allows to simulate the behaviour of a human driver in a more realistic way since, when encountering an obstacle, it is expected to dodge it by going around it.

Regarding the repulsive force direction, another situation should be taken into account since the need to perform a multiple overtake could arise due to the presence of multiple obstacles that are relatively close and in opposite sides regarding the centerline. In this scenario, the vehicle's response may not have the necessary anticipation — once again due to the repulsive potential field formulation — as it will

34

only consider the obstacle in front as a reference for repulsion when the distance to the obstacle behind is higher. As such, the algorithm should also be able to detect if the first obstacle is already behind in order to use the second to perform the computation of the repulsive force, even if it is far away. To check if the first detected obstacle is behind, two different reference points could be used, namely the CG of the car or the middle point of the rear axle, where the latter could be seen as a more conservative approach. With any of these points, an obstacle can be considered to have already been passed if the chosen point is after the foremost part of the obstacle or after a given distance from it. In this work the CG was used and a given obstacle was considered as passed when the CG was ahead of all the edges, as represented in Figure 3.13.

(a) Typical repulsive force direction　　　(b) Modified repulsive force direction
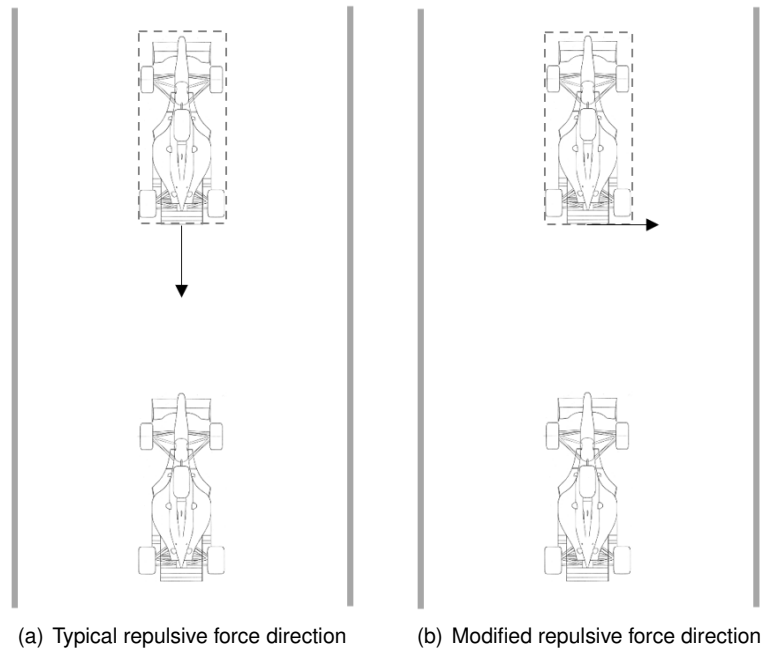
Figure 3.12: Change in the repulsive force direction
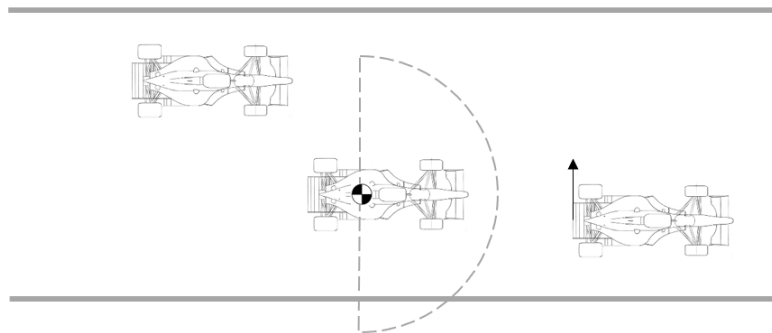
Figure 3.13: Schematic of the verification if some obstacle is already behind

This ability to check if a given obstacle can be seen as already behind was implemented to prevent possible problems related with anticipation in a scenario where multiple obstacles were detected, but its use is not exclusive of such scenario. However, in the case where only one obstacle is detected, if such obstacle have been passed, the repulsive force will be computed using the track limits.

Gains variation

The last modification implemented was relative to the gains K_{att} and K_{rep} associated with the attractive and repulsive forces, respectively, and it was done as an extra safety measure.

Using the potential field approach developed, the guidance of the vehicle results from the combination of both repulsive and attractive effects. However, such effects are weighted — through K_{rep} and K_{att} — meaning that a situation may arise where the proportion between the two is not enough to prevent collision or ensure that the vehicle remains inside the track. As such, some mechanism should be implemented to try to avoid it, adapting the weights that, for the path planning algorithm, were set as constant. This adaptation is intended to mimic the expected behaviour of a vehicle steered by a pilot and it was thought under two different scenarios, namely possible collision and multiple obstacle detection.

With respect to the possible collision scenario, thinking in a person-driven situation, if a human driver foresees a collision, then he will turn the steering wheel more. As such, to simulate this in a driverless vehicle, the algorithm must project the current trajectory a fixed distance ahead d_{pred} and check if this projection collides with the obstacle— as represented in Figure 3.14 —; if it will, K_{rep} must be increased in order to push the vehicle further away from the obstacle, as increasing this gain will result in a higher steering command. Nonetheless, K_{att} should also be decreased since setting the target — used in the computation of the attractive force — in a centerline point could lead to the vehicle being pulled along the direction of the obstacle, closer back to the center of the track. Thus, decreasing this gain allows the direction of the resultant force to be closer to the direction of the repulsive force, pushing the vehicle away from the obstacle.
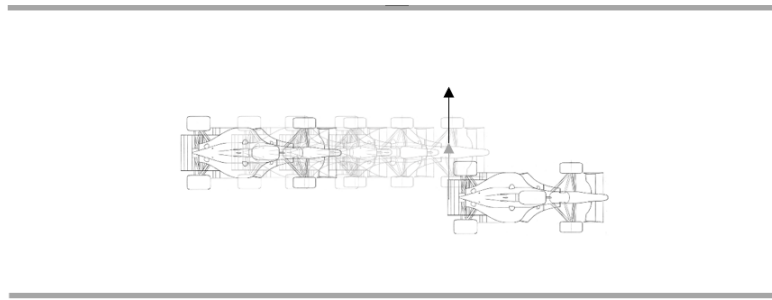
Figure 3.14: Situation in which the projected trajectory collides with the obstacle and the repulsive force is consequently increased

Regarding the detection of multiple obstacle, this will influence K_{att}, as this parameter is indirectly related with the vehicle environment that is taken into account. When a human driver is faced with a more demanding scenario, such as to overtake multiple obstacles, the overall environment that he considers to make a decision decreases, since he is more focused on what is in his vicinity. This behaviour can be achieved, in the autonomous driving algorithm, through a decrease in K_{att}, which decreases the weight of the attractive force and, consequently, increases the weight of the repulsion component in the resultant force.

Chapter 4

Decoupled Control Approach

From the models presented in Chapter 2, it is possible to observe a coupling between the longitudinal and lateral subsystems. However, the linearisation of the vehicle model that captures the tire-road interaction — which can be found in [30] —, results in a decoupling of these two subsystems where: the motor torque T directly influences the tire slip ratio κ which, in turn, influences the longitudinal speed v_x; the steering angle δ directly affects the lateral speed v_y and the yaw rate $\dot{\psi}$. This suggests, for control purposes, a decoupled approach, in the sense that the lateral and longitudinal controllers could be developed independently, which was the approach followed in this work. However, as the lateral control is the main focus of this dissertation, only one longitudinal controller was implemented by opposition to lateral control, where several different strategies were tested.

Since some of the necessary variables for control are not readily available from sensors, the first section of this chapter will be dedicated to provide an insight about which variable can be measured — and how — and which variables need to be estimated. The following section will explain the design of the estimators needed to get access to the inaccessible states. After all the necessary information about the states has been provided, both lateral and longitudinal controllers will be addressed. For lateral control the strategies developed were Pure Pursuit, Linear Quadratic Gaussian, Alice controller, Kinematics Lateral Speed and Modified Sliding Mode; for longitudinal control a cascade architecture based on proportional control [30] was implemented. For each one of the controllers, a brief explanation on the underlying theoretical principles is presented, as well as the respective control laws and block diagrams in order to provide a better understanding of the implementation structure.

4.1   Available Sensors and Required Estimations

The different control strategies that will be described in this chapter require information — that can be obtained either through measurement or estimation — about some of the states of the realistic model, presented in Chapter 2, in order to fulfil the objective of controlling the vehicle. Therefore, an insight about which states can be accessed — and how — and which states need to be estimated must be provided considering a realistic scenario for simulation.

Generally, with respect to guidance, the control relies mainly on the detection of the plastic cones used to define the limits of the race track, which could then be used to generate the path for the vehicle to follow. Such detection is usually achieved through cameras, LiDAR sensors or a combination of both to compensate for individual shortcomings and achieve a positive redundancy. In this thesis, two different scenarios were developed regarding the planning: one in which the reference trajectory is generated offline; and another one where it was generated online. For the second scenario it was assumed that the cameras and LiDAR sensors can provide the information needed to allow the navigation of the vehicle in the track outlined by the cones. For the first scenario, information about some states regarding a fixed coordinate system should be included. Thus, it was assumed that the position of the vehicle in the global frame (X_P, Y_P) could be accessed with the aid of a GPS system, and its orientation ψ resorting to an appropriate compass or gyroscope. However, it should be stressed out that usually the GPS system does not have the precision required so it was assumed that the information needed was obtained from an ideal GPS or sensor fusion between this system and other sensors. Lastly, some of the control strategies used in this scenario will still require some additional information, such as the rate of change of the lateral error $\dot{e}_y$, the lateral velocity v_y and the yaw rate $\dot{\psi}$. Although, to obtain the latter, an inertial measurement unit (IMU) could be used, the same simulation scenario as in [33] was adopted, meaning that this sensor was not available. As such, all these three states need to be estimated.

Regarding the sensors mentioned, a remark should be made. As this thesis does not cover sensor modelling, its functioning was only emulated converting the variables in the global frame, obtained from the simulator, into the local frame — which are the ones provided by the sensors. Considering (X, Y) and (x, y) the coordinates of a given set of point — which could represent, for example, plastic cones — in the global and local frames respectively, the relation between them can be expressed through

$$\begin{bmatrix} X \\ Y \end{bmatrix} = \begin{bmatrix} X_P \\ Y_P \end{bmatrix} + \begin{bmatrix} \cos(\psi) & -\sin(\psi) \\ \sin(\psi) & \cos(\psi) \end{bmatrix} \begin{bmatrix} x \\ y \end{bmatrix} \qquad \text{[m]} \qquad (4.1)$$

where (X_P, Y_P) stands for the coordinates of the local frame origin expressed in the global frame. Thus, from the knowledge of the vehicle's position (X_P, Y_P) and orientation ψ, obtained from simulation, the required transformation to obtain a given point in the local reference frame can be obtained by inverting the rotation matrix in (4.1) and solving for (x, y).

When it comes to velocity control, the strategy used will require the feedback of the yaw rate $\dot{\psi}$, longitudinal speed v_x and slip ratio κ which are not available from sensors. Although an accelerometer or a speedometer could provide useful information, v_x cannot be obtained from any of these sensors: the accelerometer is sensitive and noisy, so obtaining the longitudinal speed through integration is inaccurate; due to the presence of longitudinal slip, the angular speed obtained from the speedometer will not correspond directly to the longitudinal speed of the vehicle. Hence, as no sensor could provide information about the slip ratio, both v_x and κ are not available and should be estimated. However, since the lateral control is the main focus of this thesis, the estimation of these two states will not be covered and, as such, it was assumed that the variables of interest were available for feedback.

4.2 Observer

Some of the control strategies that will be used assume that all the necessary variables are available. However, as already stated, such assumption may not be realistic, as some of these states may be impossible or impractical to measure becoming, in these cases, necessary to design an estimator. As such, in this section, the theoretical background inherent to an estimator will be presented and the implementation approach described.

An estimator — also referred to as state observer — provides a state estimation $\hat{\mathbf{x}}(t)$ of the system states $\mathbf{x}(t)$, using information regarding the system outputs $\mathbf{y}(t)$ and inputs $\mathbf{u}(t)$. A block diagram for such structure is presented in Figure 4.1, representing the general architecture of a linear state space observer, in which $\mathbf{L_O}$ stands for the observer gains, responsible for the correction of the estimated states. As less accurate estimations can be obtained if the stochastic nature of the signals is not considered in the observer design, a Kalman-Bucy filter was implemented, since this observer also takes into account the measurement noise.
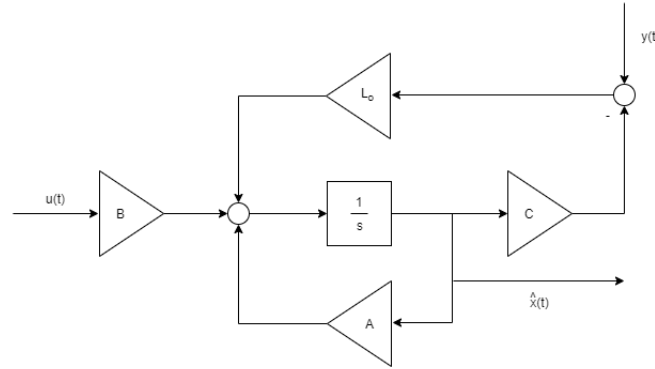
Figure 4.1: Block diagram for a linear state space observer

Considering $\mathbf{A}$ the system dynamic matrix, $\mathbf{B}$ and $\mathbf{C}$ the input and output matrix and $\mathbf{D}$ the direct input-output matrix, the state space equations are

$$\dot{\mathbf{x}}(t) = \mathbf{A}\mathbf{x}(t) + \mathbf{B}\mathbf{u}(t) + \mathbf{w}(t) \tag{4.2a}$$

$$\mathbf{y}(t) = \mathbf{C}\mathbf{x}(t) + \mathbf{D}\mathbf{u}(t) + \mathbf{v}(t) \tag{4.2b}$$

where $\mathbf{w}(t)$ stands for the process disturbances and $\mathbf{v}(t)$ represents the noise in the measurements provided by the sensors. By defining the estimation error $e(t)$ as the difference between the system real state $x(t)$ and the estimated one $\hat{x}(t)$, it is possible to determine the dynamics of the observer estimation error as

$$\dot{\mathbf{e}}(t) = (\mathbf{A} - \mathbf{L_O}\mathbf{C})\,\mathbf{e}(t) + \mathbf{w}(t) - \mathbf{L_O}\,\mathbf{v}(t) \tag{4.3}$$

Since the principle of this observer is to combine the *a priori* information — from the system model — with the *a posteriori* information — from the measurements — in order to obtain an asymptotically stable error dynamics, the problem resorts in finding the gains $\mathbf{L_O}$ that minimises the variance of the

steady-state estimation error. If the pair $(\mathbf{A}, \mathbf{C})$ is observable, such gains can be computed from [45]

$$\mathbf{L_O} = \mathbf{P_0}\mathbf{C}^\top\mathbf{R_0}^{-1} \tag{4.4}$$

in which $\mathbf{P_0}$ stands for the symmetric positive-definite solution of the *Algebraic Riccati Equation*

$$\mathbf{A}\mathbf{P_0} + \mathbf{P_0}\mathbf{A}^\top + \mathbf{Q_0} - \mathbf{P_0}\mathbf{C}^\top\mathbf{R_0}^{-1}\mathbf{C}\mathbf{P_0} = 0 \tag{4.5}$$

where $\mathbf{Q_0}$ and $\mathbf{R_0}$ are the process and sensor noise covariance matrices, respectively. Being the process noise covariance difficult to estimate and taking into account that, although the sensor noise covariance could be known in advance it could also be experimentally obtained, both covariances may be seen as design parameters, needing to be tuned, despite their inherent stochastic meaning. Since the relative difference between them affects both the convergence speed of the estimations and the bandwidth of the filter — and, consequently, the amount of noise filtered —, a compromise must be made while tuning.

Regarding its implementation and need, recapitulating what was mentioned in the previous section: for the longitudinal controller, the slip ratio κ, longitudinal speed v_x and yaw rate $\dot{\psi}$ are not accessible; from the lateral controllers, the Linear Quadratic Gaussian (LQG) and the Modified Sliding Mode (MSM) will require knowledge about the lateral velocity v_y, yaw rate $\dot{\psi}$ and rate of change of the lateral error $\dot{e}_y$, which can not be obtained from sensors. However, being the vehicle's guidance the main focus of this work, only the ones related with the lateral control were effectively implemented. With respect to the estimators implemented, an important remark must be made. Since the dynamics models of the system that will be used — namely the ones given in (2.39) and (2.47) — are time variant when the longitudinal velocity is not constant, the models and gains related with the observer need to be updated online in order to take this into account. Although one of the possible approaches is to calculate such gains online — solving the *Albegraic Riccati Equation* at each instant of simulation —, a different one was followed, namely a gain scheduling, since it is computationally less demanding. In this method, the gains are calculated offline for the speed operating range and then obtained from a neighborhood table containing these values.

Taking the mentioned updates into account, a general block diagram of the observer implemented can be represented as in Figure 4.2 where the terms model, input, output and estimations are specified in Table 4.1 for each one of the controllers. This figure represents the underlying structure of the block designated as 'Observer' in the block diagrams that will be presented in the next section.

Table 4.1: Specifications of the terms present in Figure 4.2 for each one of the controllers

	LQG	MSM
Model	(2.39)	(2.47)
Input	δ_{cmd}	δ_{cmd}
Output	Y, ψ	e_y, e_ψ
Estimations	$v_y, \dot{\psi}$	$\dot{e}_y$
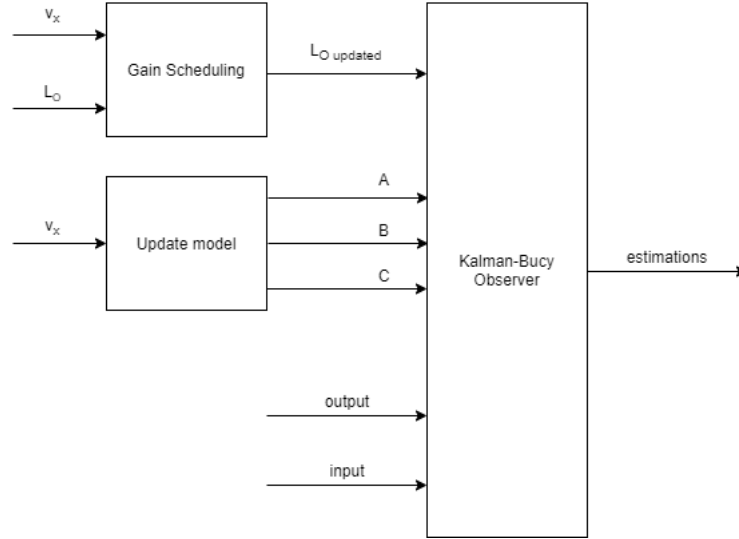
Figure 4.2: Overall block diagram for the system observer

4.3 Lateral Control

Now that all the necessary information about the states needed for control was provided, lateral control will be addressed, which is related with the ability to steer the vehicle to a different lateral position. This guidance mechanism frequently relies on the knowledge of the vehicle's pose regarding the track, or in relation to a given reference path, resorting to variables typically called path-following errors, since they consist on a comparison between some particular pose of the vehicle and how this same pose should be, according to the track or the reference path [33].

Due to the importance of these path-following errors in this topic, a subsection was created to formally define and formulate them, which will be presented next. The control strategies that use these variables will be described in the following subsection.

4.3.1 Cross-track and Heading Errors

In autonomous driving it is essential to know the vehicle pose relative to the track in order to allow the control algorithm to correct possible errors. These can be related with a distance — like the cross-track error — or with an angle — which the heading error is an example of. Hence, it is of fundamental importance to provide a proper definition for such errors.

Considering two reference points, namely the closest point to the vehicle on the path — denoted by $\mathbf{p}_{RP}$ — and the vehicle position — denoted by $\mathbf{p}$ —, the cross-track error can be defined as the distance between these two points; however, the definition of the heading error is not unique: it can concern the angle between the tangent of the path at the reference point $\mathbf{t}_{RP}$ and the direction ψ of the vehicle or the angle between the referenced tangent and the vehicle's velocity vector $\mathbf{v}$. From these two possibilities — represented in Figure 4.3 —, with regard to the calculation of the heading error, the latter was used, as it will be advantageous in the minimisation of this error when the vehicle is moving in the global reference

frame with a lateral velocity v_y different from zero, causing sideslip, i.e., a misalignment between $\mathbf{v}$ and ψ [33].

(a) Heading error considering the direction of the vehicle

(b) Heading error considering the vehicle's velocity
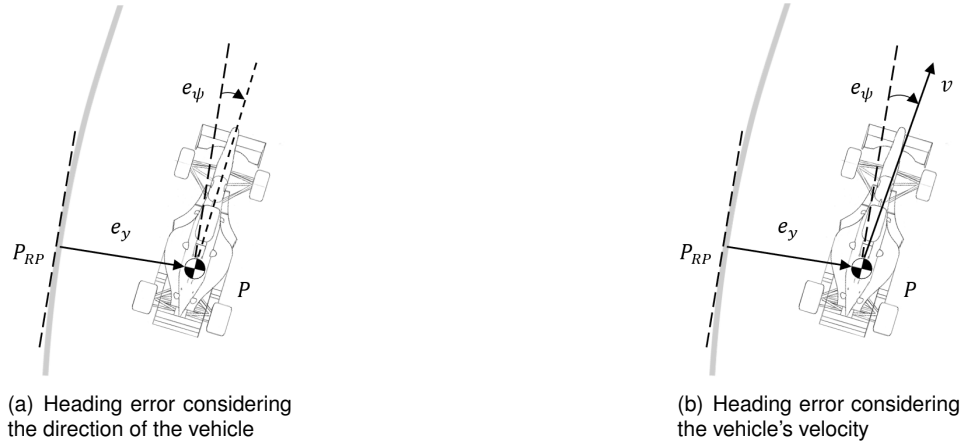
Figure 4.3: Cross-track and heading errors

The mathematical formulation of these errors will be derived in this subsection and an explanation about how they were used in the implementation stage will be presented. Since, for control purposes, the errors were computed under the assumption that the waypoints are connected by polynomial functions, whereas, for performance evaluation, the metrics use a distinction between line segments and circumference arcs, the computation under the three assumptions will be presented.

Regarding the computation of these path-following errors a last remark should be made. In most of the situations that required vehicles to follow a given reference path, the use of a look-ahead distance may present itself as beneficial, since it allows for a timely correction of the errors, providing an anticipatory capability. As such, this logic will be introduced here and, although it can be applied to any of the cases of waypoint connections mentioned, it was only applied to the scenario used for control: using polynomial functions to curve fit the waypoints of a course.

4.3.1.1 Path-following Errors Using Line Segments

The first assumption considers a straight-line connection between waypoints, which can pose some problems as there is no continuity of the first derivative of the path due to the fact that, most of the time, the waypoints are not aligned with each other. As such, it was only used as a safety mechanism for control — in case the assumption used for control is no longer applicable due to the vehicle being too far out of the path — and for performance evaluation.

Defining $\mathbf{d}_{1,2} = \mathbf{p}_{\mathsf{WP}_2} - \mathbf{p}_{\mathsf{WP}_1}$ as the displacement vector between two waypoints and $\mathbf{d}_{1,P} = \mathbf{p} - \mathbf{p}_{\mathsf{WP}_1}$ as the displacement between the first waypoint and the reference point in the car, the errors — which are represented in Figure 4.4 — can be defined as [33]

$$\mathbf{e}_y = \frac{\mathbf{d}_{1,2} \times \mathbf{d}_{1,P}}{\parallel \mathbf{d}_{1,2} \parallel} \qquad \text{[m]} \qquad (4.6a)$$

42

$$\mathbf{e}_\psi = \arcsin\left(\frac{\mathbf{d}_{1,2} \times \mathbf{v}}{\parallel \mathbf{d}_{1,2} \parallel \cdot \parallel \mathbf{v} \parallel}\right) \qquad \text{[rad]} \tag{4.6b}$$

where $\parallel . \parallel$ stands for the Euclidean norm of the respective vector, $\times$ denotes the cross-product between two vectors and the cross-track error is considered positive when the vehicle is on the right-side of the reference path. However, it should be noticed that, being both errors based on the cross-product between vectors in the XY plane, in a tri-dimensional space only the Z component of the equations (4.6) will be considered for the error computation, as it is the only non-null component. This holds true for the remaining expressions of these errors that will be obtained when the waypoints are assumed to be connected by circumference arcs or polynomial functions.
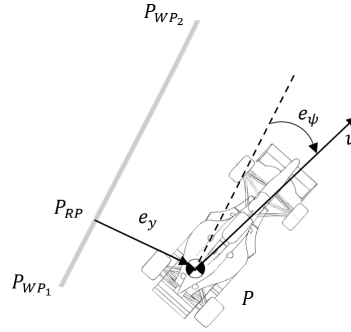
Figure 4.4: Cross-track and heading errors for a line segment

Regarding the present and subsequent figures, an observation should be made: although the vehicle reference point is represented in such figures as the CG, it can be in other locations, being usual to consider the middle of the rear axle.

4.3.1.2 Path-following Errors Using Circumference Arcs

The second situation where path-following errors can be defined is when the connection between two waypoints is done resorting to circumference arcs, which requires taking into account the fact that such points can be part of two different circumferences, for a fixed radius R, since the center C can be at the right or at the left relatively to the waypoints — as exemplified in Figure 4.5. As such, it is necessary to attribute a sign to the radius in order to uniquely define its center and correctly compute the necessary errors [33]. The radius will be considered as positive when the center is placed at the right of the segment and negative otherwise.

In addition to leading to a constant change in the reference point $\mathbf{p}_{\mathsf{RP}}$, when navigating close to an arc the tangent of the circumference will also be altered. As such, the expressions for both errors should take this into account. Defining the distance of the vehicle reference point to the center of the circumference as $\parallel \mathbf{d}_{\mathsf{PC}} \parallel$ and the orthogonal vector $\mathbf{d}_{\mathsf{PC}_\perp}$ as the tangent to the path — which can be given by $[d_{\mathsf{PC}_Y} \ -d_{\mathsf{PC}_X} \ 0] = [Y_C - Y_P \ X_P - X_C \ 0]$ where d_{PC_X} and d_{PC_Y} are the coordinates of the original displacement vector going from P to C — the errors can be computed from [33]

$$e_y = \mathsf{sign}(R) \cdot \left(|R| - \parallel \mathbf{d}_{\mathsf{PC}} \parallel \right) \qquad \text{[m]} \tag{4.7a}$$

43

$$\mathbf{e}_\psi = \text{sign}(R) \cdot \arcsin \left(\frac{\mathbf{v} \times \mathbf{d}_{\text{PC}_\perp}}{\| \mathbf{v} \| \cdot \| \mathbf{d}_{\text{PC}_\perp} \|} \right) \qquad \text{[rad]} \qquad\qquad (4.7b)$$

(a) Reference arc with positive R (b) Reference arc with negative R

Figure 4.5: Cross-track and heading errors for a circumference segment

4.3.1.3 Path-following Errors Using Polynomial Functions

The last assumption — overcoming the disadvantages of previous approaches regarding the discontinuity of the first derivative and the requirement of the knowledge about the radii — assumes that a given number of n waypoints can be curve fitted by a polynomial function where such curve fitting can be made "online", obtaining a polynomial to be used as a reference path as the vehicle moves along several waypoints, discarding the ones behind it and using new ones in front [33]. In this work, such function was chosen to be a second-order polynomial defined by a minimal of 5 points — the adjacent to the vehicle and 4 in front, as represented in Figure 4.6 and suggested in [33] — since, when resorting to a look-ahead, the number of points could be higher.
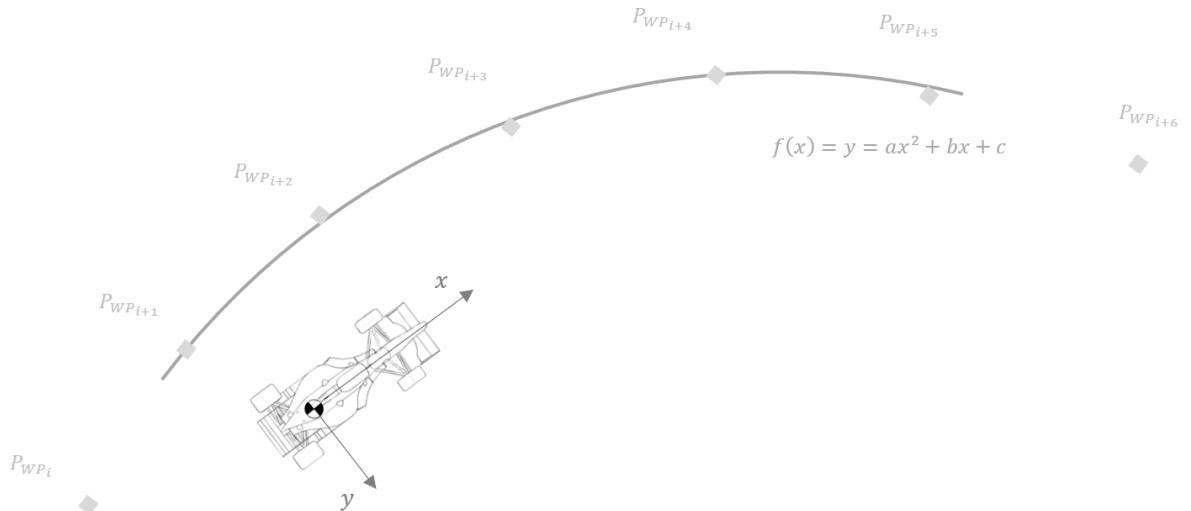
Figure 4.6: Schematics of polynomial curve fitting by least squares

As mentioned, since this is the only connectivity assumption used for control purposes — requiring

the knowledge of the reference point $\mathbf{p}_{RP}$ and the tangent vector at this point $\mathbf{t}_{RP}$, which can be obtained from the derivative of the polynomial function —, the computation of the path-following errors under this assumption must be presented in the absence or presence of a look-ahead distance L_{lad}. In the absence of a look-ahead distance, $\mathbf{p}_{RP}$ will be the real closest solution, with respect to the vehicle, of a third order equation resulting from the intersection between the second-order polynomial function and a line orthogonal to the tangent vector that passes through $\mathbf{p}$; on the other hand, when employing a look-ahead distance, $\mathbf{p}_{RP}$ will be the real positive solution of a fourth-order equation resulting from the intersection between the polynomial function and a circumference centered at the vehicle reference point with radius equal to the look-ahead distance. Both systems of equations are thoroughly explained in [33]. The errors in both scenarios are represented in Figure 4.7.

(a) Without a look-ahead distance   (b) With a look-ahead distance
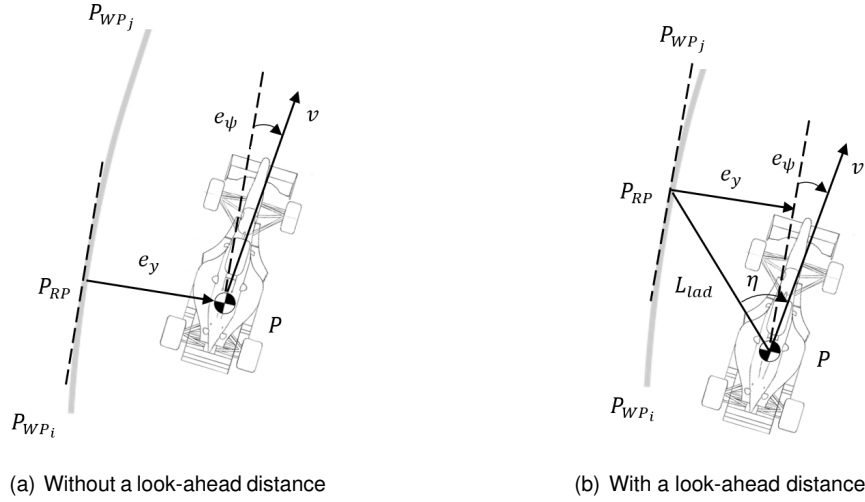
Figure 4.7: Cross-track and heading errors for a generic polynomial function

Since the only difference between using or not using a look-ahead distance is the location of the reference point $\mathbf{p}_{RP}$ — and consequently, the tangent at this point $\mathbf{t}_{RP}$ —, the mathematical expression for the cross-track and heading errors is the same regardless of the situation. Such computation can be given by

$$\mathbf{e}_y = \frac{\mathbf{p}_{RP} \times \mathbf{t}_{RP}}{\| \mathbf{t}_{RP} \|} \qquad \text{[m]} \tag{4.8a}$$

$$\mathbf{e}_\psi = \arcsin \left(\frac{\mathbf{t}_{RP} \times \mathbf{v}}{\| \mathbf{t}_{RP} \| \cdot \| \mathbf{v} \|} \right) \qquad \text{[rad]} \tag{4.8b}$$

An additional error parameter can also be defined, as it will be used in one of the controllers presented in the next subsection. Denoting it by η, it consists of the angle between the look-ahead vector — which can be obtained once the reference point has been established since its elements will be equal to the coordinates of such point in the local frame — and the velocity vector, as shown in Figure 4.7 (b). This variable can be computed as

$$\eta = \arcsin \left(\frac{\mathbf{v} \times \mathbf{p}_{RP}}{\| \mathbf{v} \| \cdot \| \mathbf{p}_{RP} \|} \right) \qquad \text{[rad]} \tag{4.9}$$

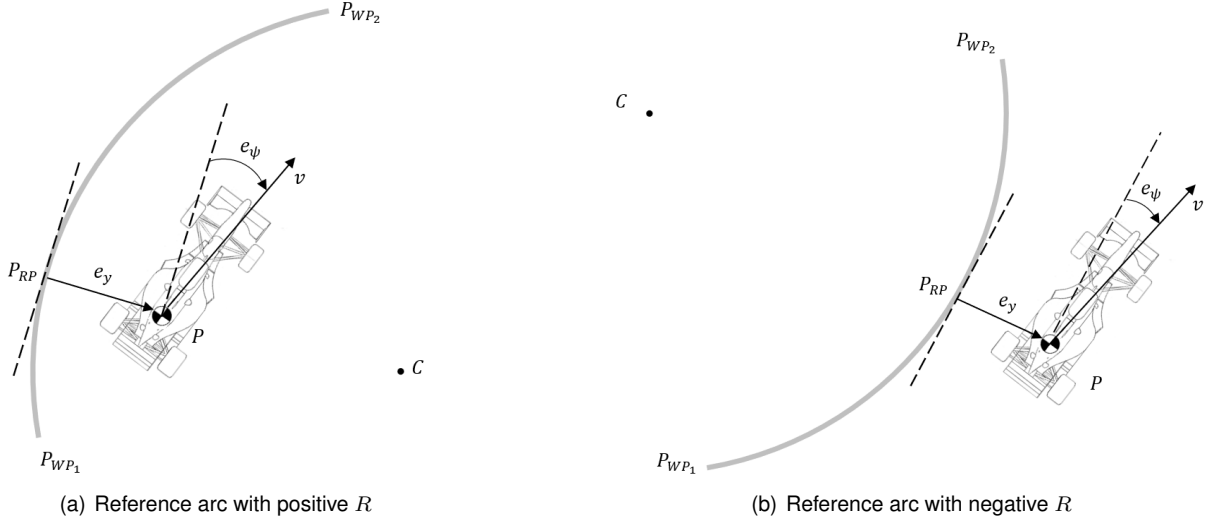where, similarly as before, only the z component will have a non-null value.

Lastly, it is important to mention that although for the line segment and circumference arc scenarios the waypoints are expressed in the global frame — since the path-following error will be only used as a validation tool —, in this scenario the waypoints used in the polynomial curve fitting by least squares must be expressed in the local frame, as if a driver would use them to effectively steer the car. Hence, the proper reference frame transformation must be applied in order to obtain $\mathbf{p}_{RP}$ in the correct frame. This transformation is the one explained in section 4.1.

4.3.2 Control Strategies

In the previous subsection, several path-following error strategies were presented being, as mentioned, the one where the waypoints of the path are curve fitted by a second-order polynomial — in a coordinate system centered on the vehicle — chosen for control purposes since it will result in smoother error curves in time, providing smoother command inputs to the steering angle [33].

Hence, in this subsection the different control strategies implemented that resort to such path-following errors will be presented. However, due to its complex and lengthy nature, only a brief explanation will be presented, as well as the final control law and the block diagrams. The reasoning that allowed to obtain such law will be only cited for interested readers. Since performing a stability analysis for each one of the control laws — which is usually done resorting to Lyapunov, linearisation or numerical methods — is out of the scope of this work, this information can be found on the provided references or with further research.

4.3.2.1 Pure Pursuit

The first path-following strategy to be successfully implemented was the Pure Pursuit (PP) controller [46] which consists of a nonlinear control strategy where only one parameter is used as error — the angle η, represented in Figure 4.7 (b).

Assuming a kinematics vehicle model, and using a circular arc to connect the rear axle of the vehicle to an imaginary point moving along the desired path — which can be thought as a pseudo target —, this controller calculates the required steering angle from the curvature of such arc — which can be obtained geometrically as shown in [46] — through the following law

$$\delta_{cmd} = \arctan\left(\frac{2L\sin(\eta)}{L_{lad}}\right) \quad \text{[rad]} \tag{4.10}$$

where, although only one error parameter is used, as mentioned, the information of both cross-track and heading errors is incorporated since η will increase when the vehicle is further from the path as well as when it has a larger difference in orientation.

The block diagram of a Pure Pursuit controller is presented in Figure 4.8, being fairly simple as this controller only requires the establishment of a look-ahead distance L_{lad} and the knowledge about the vehicle's pose X, Y, ψ and the waypoints $\mathbf{p}_{WP}$.

Lastly, more information can be found in [46] — where the computation of the curvature and the

algebraic manipulation required is explained in detail — or even in [47], since there is a considerable resemblance in the logic behind the PP and L1 controllers, leading to similar control laws.
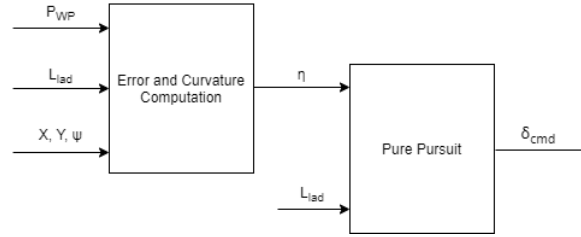
Figure 4.8: Block diagram for the Pure Pursuit controller

4.3.2.2 Linear Quadratic Gaussian

The second controller to be applied at the problem at hand is the Linear Quadratic Gaussian (LQG) controller, since the linear control strategy inherent to a Linear Quadratic Regulator (LQR) controller was used with a Kalman-Bucy observer — which was explained previously on this chapter.

The LQR approach consists on minimising the quadratic performance index presented in (4.11), which penalises how far the final state of the system is from zero at the end of a finite time horizon t_h and the state and control authority evolution during the same time horizon t_h.

$$J = \mathbf{x}^\top(t_\mathsf{h})\mathbf{P}(t_\mathsf{h})\mathbf{x}(t_\mathsf{h}) + \int_0^{t_\mathsf{h}} \left(\mathbf{x}^\top(t)\mathbf{Q}\mathbf{x}(t) + \mathbf{u}^\top(t)\mathbf{R}\mathbf{u}(t)\right)dt \tag{4.11}$$

In this index, $\mathbf{Q}, \mathbf{R}$ and $\mathbf{P}(t_\mathsf{h})$ are tuning parameters of the optimal control design.

In order to solve the LQR problem, three requirements need to be satisfied, namely the pair $(\mathbf{A}, \mathbf{B})$ needs to be controllable — where $\mathbf{A}$ stands for the dynamic matrix and $\mathbf{B}$ for the input matrix associated with a linear state space representation, meaning that first the system needs to be linearised as this is a linear control strategy — [45], the cost matrices related with the penalty of the state need to be symmetric positive semi-definite and the matrix related with the actuator authority needs to be symmetric positive definite. With these requirements being met, the gains that enable the control action to minimise the performance index (4.11) can be determined solving a *Matrix Differential Riccati Equation* (MDRE) leading to a time-varying state feedback control law.

However, as time horizon approaches infinity, the solution of such differential equation converges to a positive definite or semi-definite value. Hence, a simpler equation can be solved which allows to obtain a significantly good approximation of the optimal solution consuming considerably less computational resources. In this case, the initial performance index (4.11) can be rewritten as

$$J = \int_0^\infty \left(\mathbf{x}^\top(t)\mathbf{Q}\mathbf{x}(t) + \mathbf{u}^\top(t)\mathbf{R}\mathbf{u}(t)\right)dt \tag{4.12}$$

where $\mathbf{Q}$ penalises the deviation of $\mathbf{x}(t)$ from zero, $\mathbf{R}$ penalises the actuator authority and $\mathbf{u}(t)$ stands for the solution that minimises this index. The resulting sub-optimal solution is given by the state feedback

control

$$\mathbf{u}(t) = -\mathbf{K}\mathbf{x}(t) \tag{4.13}$$

with $\mathbf{K} = \mathbf{R}^{-1}\mathbf{B}^{\top}\mathbf{P}$. The matrix $\mathbf{P}$ needed to compute the gains $\mathbf{K}$ corresponds to a stationary solution of the original MDRE, which can be obtained from the *Albegraic Riccati Equation* (ARE)

$$0 = \mathbf{A}^{\top} + \mathbf{P}\mathbf{A} - \mathbf{P}\mathbf{B}\mathbf{R}^{-1}\mathbf{B}^{\top}\mathbf{P} + \mathbf{Q} \tag{4.14}$$

In the domain of this linear control strategy an LQR controller with a Kalman-Bucy filter considering the bicycle dynamics model provided on (2.39) was implemented. The need for an observer is due to the fact that only e_y and e_ψ can be obtained from the information provided by sensors, meaning that states v_y and $\dot{\psi}$ must be estimated. The control law (4.13) can be written as [33]

$$\delta_{cmd} = -(K_y^{LQG}e_y + K_\psi^{LQG}e_\psi + K_{v_y}^{LQG}v_y + K_{\dot{\psi}}^{LQG}\dot{\psi}) \qquad \text{[rad]} \tag{4.15}$$

where $K_y^{LQG}, K_\psi^{LQG}, K_{v_y}^{LQG}$ and $K_{\dot{\psi}}$ are the gains obtained from the ARE. Since the model used is parameterised as a function of longitudinal velocity, these gains will be velocity dependent making it necessary to update them accordingly. As such, a gain scheduling solution was implemented, once again, instead of solving equation (4.14) at each instant of simulation — similar to what was mentioned for the observer's gains. The block diagram for the LQR controller is presented in Figure 4.9.
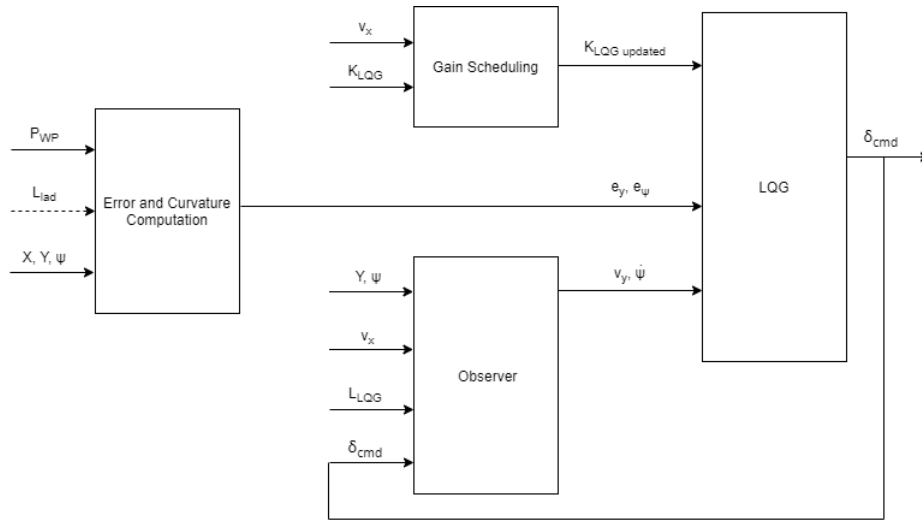
Figure 4.9: Block diagram for the LQG controller

Regarding Figure 4.9 three brief remarks must be made. Firstly, this strategy is significantly more complex in terms of implementation, when compared to the previous one, due to the presence of a gain scheduling and an observer. Secondly, regarding this estimator, the respective block also has an inherent gain scheduling, since the models of the system used are linear time variant when the longitudinal velocity is not constant — as it was explained in the previous section. Lastly, the input L_{lad} in the block 'Error and Curvature Computation' was represented with a dashed arrow since, for this controller, the use of a look-ahead distance is not mandatory, but could be beneficial due to the inherent

anticipation capability.

More information can easily be found, as this is a widely studied subject in the literature, being suggested [29, 33, 45].

4.3.2.3   Alice controller

The third implemented controller — which will be addressed as Alice since it was developed by Team Caltech for the 2005 DARPA Autonomous Vehicle Challenge and implemented in the Alice autonomous car — uses the Ackermann steering principle, the kinematics of the bicycle model and the look-ahead concept to obtain the steering angle.

In this nonlinear proposed control strategy, the real vehicle is projected orthogonally onto the closest point of the reference trajectory $\mathbf{p}_{RP}$ and the heading of the arising virtual vehicle is aligned with the tangent of the trajectory at the closest point. The front wheels of the projected vehicle are then turned in a way that its turning radius coincides with the curvature of the reference trajectory at $\mathbf{p}_{RP}$, thus keeping it on the reference trajectory [48] — as represented in Figure 4.10. The inherent control law can be formulated as [49]

$$\delta_{cmd} = \arctan\left(\frac{-\cos(e_\psi)e_y - (L + L_{lad})\sin(e_\psi)}{L - (L + L_{lad})\cos(e_\psi) + \sin(e_\psi)e_y}\right) \qquad \text{[rad]} \qquad (4.16)$$

where the cross-track error e_y stands for the distance between the rear axle and the nearest point of the reference path — instead of considering the point obtained from the look-ahead distance [49].
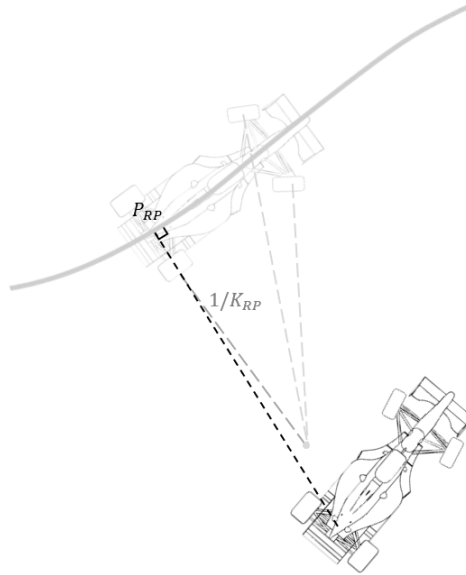
Figure 4.10: Graphical illustration of the Alice control strategy

Although the expression of the control law has some complexity, the block diagram of the Alice controller — presented in Figure 4.11 — is simple because, as in the case of the PP controller, it only requires the establishment of a look-ahead distance L_{lad} and the knowledge about the vehicle's pose X, Y, ψ and the waypoints $\mathbf{p}_{WP}$.
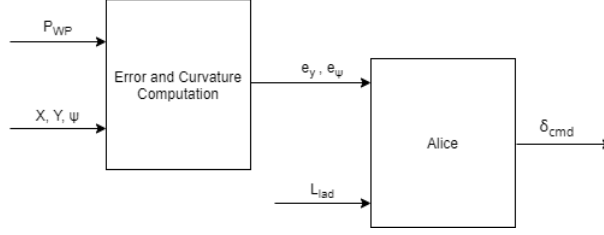
Figure 4.11: Block diagram for the Alice controller

Lastly, since it was hard to find relevant information regarding this controller, only [48, 49] — the main sources used in this work — are suggested for further reading.

4.3.2.4 Kinematics Lateral Speed

The fourth path-following strategy implemented was the Kinematics Lateral Speed (KLS) controller [46], in which the rear lateral distance and the heading error are controlled by controlling the rate of change of the cross-track error $\dot{e}_y$ through a kinematic control law.

This controller — as well as the next one that will be presented — resorts to a bicycle vehicle model formulated with respect to the reference path. Such model has the cross-track error e_y, the heading error e_ψ and the curvilinear abscissa s of the closest point $\mathbf{p}_{RP}$ to the vehicle along the path as states [46]. The linearisation of this model allows to obtain a general expression — that can be found in [46] — for the steering angle which is then used to obtained the control law that will be provided for this controller and the next one.

Defining the desired rate of change of the cross-track error $\dot{e}_{y_d}$ as the speed at which the rear axle must approach the line tangent to the path at $\mathbf{p}_{RP}$ [46], this controller bases itself on the distance between the vehicle and the reference path and on how such distance should influence $\dot{e}_{y_d}$: if the car is far from the reference line, it is required to make it get closer at higher rate than it would if it was close [46]. As such, $\dot{e}_{y_d}$ can be defined as proportional to the cross-track error e_y, with negative sign. In order to reduce the error between the desired and actual rates of change, the controller must steer the car accordingly with [46]

$$\delta_{cmd} = \arctan\left(L\left(-K_\psi^{KLS} \sin(e_\psi) - \frac{K_\psi^{KLS} K_{e_y}^{KLS} e_y}{v_x} + \frac{k_{RP}\cos(e_\psi)}{1 - k_{RP}e_y} \right) \right) \qquad \text{[rad]} \qquad (4.17)$$

where K_ψ^{KLS} and $K_{e_y}^{KLS}$ are positive constants and k_{RP} denotes the curvature of the path at the reference point $\mathbf{p}_{RP}$. However, since, for control purposes, the waypoints are expressed in the local frame and to compute the path-following errors a second-order polynomial was used to curve fit a given set of such waypoints, the curvature can be obtained from a different definition to the one presented in (3.6). Considering x_i and y_i the coordinates expressed in the local frame of the n curve fitted points for the reference path generation and $f(x) = y = ax^2 + bx + c$ the function describing the second-order polynomial used — as represented in Figure 4.6 —, k_{RP} can be computed as

$$k_{RP} = \frac{2a}{(1 + (2ax_{RP} + b)^2)^{\frac{3}{2}}} \qquad \text{[m}^{-1}] \qquad (4.18)$$

50

where the lower letter k was used since it is with respect to the local frame.

The block diagram of this approach is represented in Figure 4.12, where a direct influence of the path curvature and vehicle's longitudinal speed on the steering angle command can be seen, which was not present with the previous approaches.
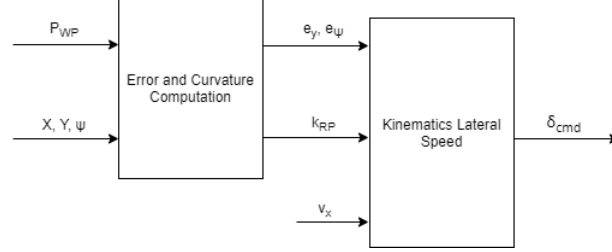
Figure 4.12: Block diagram for the Kinematics Lateral Speed controller

Further details regarding the deduction of the control law presented can be found in [46].

4.3.2.5   Modified Sliding Mode

The last control strategy used resorts to a Modified Sliding Mode (MSM) controller which has the advantage of not requiring a precise model of the system [46].

Having been developed since 1950s, sliding mode control strategy is recognised as one of the most promising techniques to generate robust control algorithms that are invariant — in the sense that the system remains insensitive to certain types of disturbances and uncertainties — under certain conditions. However, due to the discontinuous nature of its control action — caused by the typical switching that is applied in order to guarantee convergence to a given imposed dynamics (sliding surface) — this type of control usually leads to oscillations that are commonly designated as chattering [50]. Such phenomenon is a consequence of the high speed of the system trajectory when reaching the switching surface and the switch inertia, but it can be weakened or eliminated. This can be achieved through the use of smooth functions to describe the approach to the sliding surface — instead of the discontinuous function sign — or the use of higher order sliding mode. As such, defining a sliding surface σ as [46]

$$\sigma = K_{e_y} e_y + K_{e_\psi} e_\psi \tag{4.19}$$

— where K_{e_y} and K_{e_ψ} are weighting coefficients — and resorting to the controller

$$\dot{\sigma} = -K_\sigma \sigma \tag{4.20}$$

— that ensures stability without chattering [46] —, a modified sliding mode control law [46] can be written as

$$\delta_{cmd} = \arctan\left(L\left(\frac{C_1}{v_x} + k_{RP} \frac{\cos(e_\psi)}{1 - k_{\mathsf{RP}} e_y} \right) \right) \qquad \text{[rad]} \tag{4.21}$$

In (4.21), k_{RP} stands for the curvature at the reference point, which can be computed from (4.18), and

C_1 is given by

$$C_1 = -\frac{K_\sigma^{MSM} K_{e_y}^{MSM} e_y + K_\sigma^{MSM} K_{e_\psi}^{MSM} e_\psi + K_{e_y}^{MSM} \dot{e}_y}{K_{e_\psi}^{MSM}} \qquad (4.22)$$

The block diagram of this robust control law is presented in Figure 4.13 where the need for an observer is due to the fact that the rate of change of the lateral error $\dot{e}_y$ is not accessible — as explained in the previous section.
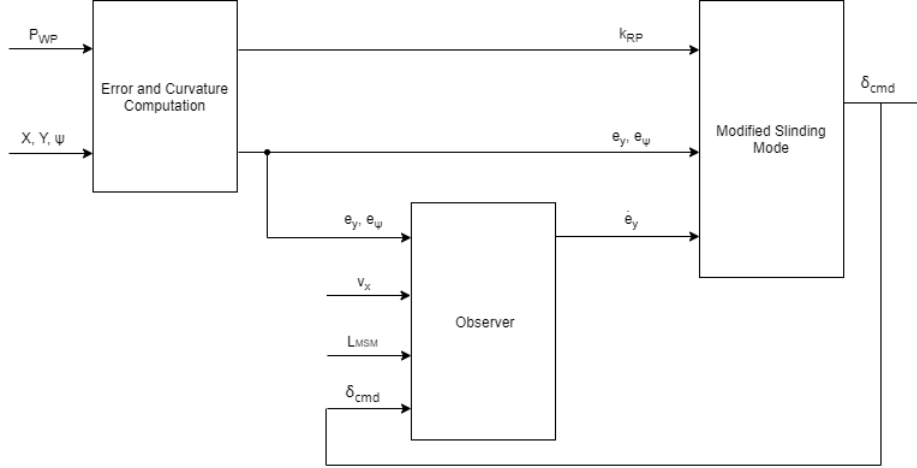
Figure 4.13: Block diagram for the Modified Sliding Mode controller

More information about the used control law can be found in [46]. However, a better understanding of the theory and concepts can be achieved through [50].

4.4 Longitudinal Control

As it was proposed in [30], a cascade control architecture with proportional gains was used. Such structure was chosen as it allows to control the coupled variables — namely the slip ratio and the longitudinal speed — separately and perform a direct saturation of the physical quantities that must be limited. In this structure, the inner and outer loops variables are the slip ratio κ and the longitudinal speed v_x, respectively, since the former has a faster dynamics.

Vertical load transfers must be taken into account, as they behave differently under acceleration and under braking: on one hand, when accelerating, the mass is transferred to the rear axle; on the other hand, it transfers to the front one, when braking. Thus, the gains should be different according to the situation, in order to be able to guarantee that the requested torque is higher on the most loaded wheels.

With this in mind, a switch control was thought as a possible approach. Since this type of control is only stable if all individual subsystems are stable and the switching is sufficiently slow, allowing the transient effects to dissipate after each switch, the computation of the dwell time is usually required [51]. However, due to the complexity in obtaining the Lyapunov function needed to compute the dwell time, a simpler approach was implemented using only one set of gains for both situations — acceleration and braking — since an analysis of both approaches — which will be presented in Chapter 5 — shows that this implementation leads to a satisfactory behaviour, without creating undesired effects in the system.

Such effects could be wheel lock, occurring if the applied braking force exceeds a critical value, stopping the wheel, or wheel spin, which can occur at any point when there is excess driving power or poor traction conditions [30].

It is still important to mention that the load transfer described above is not the only one worth considering since, when the vehicle is turning, a lateral transfer also occurs. To take this effect into account, enabling to create a lateral asymmetry in torque command, the variable κ_{diff} given by [30]

$$\kappa_{\text{diff}} = K_{\dot{\psi}}(\dot{\psi}_{\text{ref}} - \dot{\psi}) \qquad \text{[-]} \tag{4.23}$$

was introduced allowing the computation of the motor torques through

$$T_i = K_\kappa^i\big(\kappa_{\text{ref}} - \kappa_i - (-1)^i \kappa_{\text{diff}}\big) \qquad \text{[N·m]} \tag{4.24}$$

where the superscript i in K_κ denotes that such gain is different for front and rear axles and κ_{ref} can be computed through

$$\kappa_{\text{ref}} = K_{v_x}(v_{x\text{ref}} - v_x) \qquad \text{[-]} \tag{4.25}$$

The block diagram for the controller developed is presented in Figure 4.14.
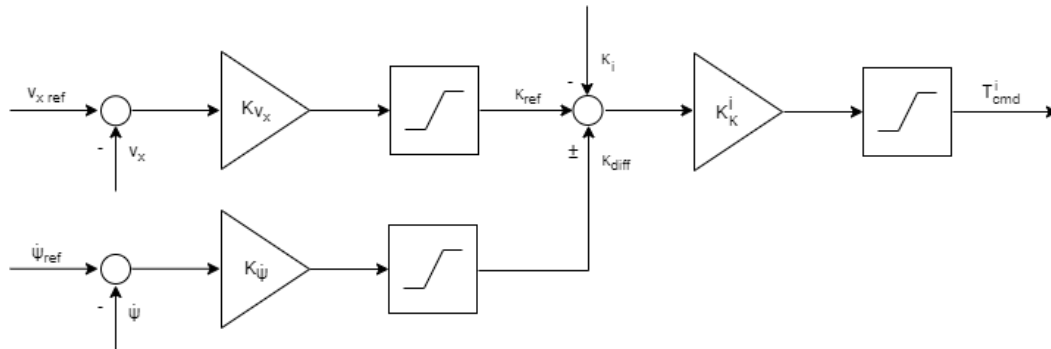
Figure 4.14: Block diagram for proportional longitudinal controller with the plus in κ_{diff} for the wheels $i = \{1,3\}$ and the minus for wheels $i = \{2,4\}$. From the third summation point forward, this diagram should be reproduced four times, one for each wheel, taking into account the proper signs for κ_{diff} and that K_κ^i it will be equal for wheels of the same axle, but different for the two axles

Regarding the gains related with speed and slip ratio, a two-step procedure was followed in order to obtain them. Designing firstly the inner loop, a known and constant slip ratio reference was assumed and the gains K_κ were chosen so that the torque was the required for that slip ratio reference being smooth, continuous and consistent with the sign of κ_{ref} [30]. Then, considering an ideal inner loop, the outer loop gain K_{v_x} was obtained in order to meet settling time, maximum overshoot and stationary error specifications. With respect to the gain related with the yaw rate $K_{\dot{\psi}}$, the value selected was the one which allowed to simultaneously meet specifications similar to the ones mentioned for the cascade gains and to obtain a lower slip in the inner wheels — when compared to the outer wheels slip — while curving at a constant speed, subject to a unitary yaw rate reference.

However, it should be stressed out that the above approach could be seen as equivalent to perform

first an estimation of the vertical load in each wheel and then establishing a gain proportional to this force, which it would have been a more systematic procedure. This was, in fact, tried by [30] using simplified models, but the estimations of the vertical forces obtained were not adequate. So, three possibilities were considered: increase the complexity of the simplified models used; assume that such forces could be measured through tire deformation by a linear potentiometer and use directly the realist model; or, finally, adopt another strategy. From the three, the latter was the one select by [30], and the intuitive approach described above was followed.

Lastly, one additional remark should be made. As referenced in section 2.1, the model used through this work was adapted from [31], modelling the vehicle as 4WD instead of RWD. This was done mainly for three reasons, namely: the behaviour while accelerating; the behaviour when braking; and the real car. Regarding the acceleration scenario, it can be said that, in order to have a satisfactory response with only two motors, the gains needed were too high leading to a constant saturation of the system; with respect to braking, since the hydraulic brake is only used in case of emergency, not for deceleration, being RWD means that the brake is performed only with the rear wheels which, as mentioned, can lead to undesired behaviour. Finally, although at this moment the autonomous vehicle is rear-driven only, future models will be four-wheel-driven meaning that, with this adaptation, the model will simulate more accurately future FS prototypes.

Chapter 5

Results and Discussion

In this chapter — which is divided into two sections, as explained in the next paragraph — the algorithms developed in Chapter 3 and the multiple controllers implemented in Chapter 4 will be evaluated. It should, however, be stressed out that a decision was made, regarding the results, choosing only to present those that derive from the realistic model. This was made since the simplified models represent merely a step in the process of providing a solution, being useful for obtaining a first insight about eventual problems, an understanding about the influence of some of the controllers' gains in the system response and, of course, to verify if a given solution — being related with planning or control — works.

The structure of this chapter is similar to the one presented in Chapter 3. As such, the results regarding the FS dynamic events will be presented in the first section and the ones related with obstacle avoidance in the second section. The parameters related with simulation, planning and control that led to the obtained results are presented in Appendix A.

5.1 FS Dynamic Events

This section concerns the results regarding path planning, which will be presented resorting to FS dynamic events. The first two events — acceleration and skidpad — are relevant instances for separately evaluate the longitudinal and lateral performance and the last two — trackdrive and autocross — for combined performance, being more generic and complex.

5.1.1 Acceleration

As mentioned in Chapter 4, the design parameters — K_{v_x}, K_κ^F, K_κ^R, and K_ψ — of the longitudinal control were tuned in a scenario where traction is the limiting factor for performance, i.e, in which motor torque saturation is not significant or present. For that purpose, a velocity step from 0 to 10 [m/s] was selected as instance. However to evaluate and validate the controller, a more demanding instance — in the sense that torque saturation strongly influences performance — was used: the acceleration event.

From the conversion of motor angular speed into vehicle linear speed, obtained through

$$\omega_m = \frac{v_x}{R} \, r_{\text{gear}} \qquad [\text{rad/s}] \tag{5.1}$$

the reference speed for such event can be given by

$$v_{x_{\text{ref}}} = \begin{cases} 29 & \text{if X<75 [m]} \\ 0.5 & \text{if X} \geq \text{75 [m]} \end{cases} \qquad [\text{m/s}] \tag{5.2}$$

since 29.4 [m/s] corresponds to the maximum vehicle speed due to hardware limits and a non-zero lower bound must be established as, due to the high motor inefficiency at low speeds, they are not adequate to fully stop the vehicle, being necessary to switch off the motors or to engage the hydraulic braking system before reaching a null speed [30].

The time response requirements, for both situations, are presented in Table 5.1. These requirements cover the typical dynamic goals for a FS prototype: responding fast, accurately, with a non-oscillatory behaviour to a longitudinal speed command [30]. The decelerating distance was established due to competition regulations [1, 38]. From the actual system response — which is provided in the same table and graphically shown in Figure 5.1 — it is possible to see that all the requirements were met.

Table 5.1: Longitudinal performance requirements and respective response

Notation	Description	Requirement		Response		Units
		Step	Acceleration	Step	Acceleration	
t_s	Settling time	<2	<5	1.80	4.53	s
e_{ss}	Steady-state error	<0.5	<1	0.04	0.26	m/s
PO	Percentage overshoot	<5	<5	0	0	%
d_{dec}	Decelerating distance	–	<100	–	58.84	m
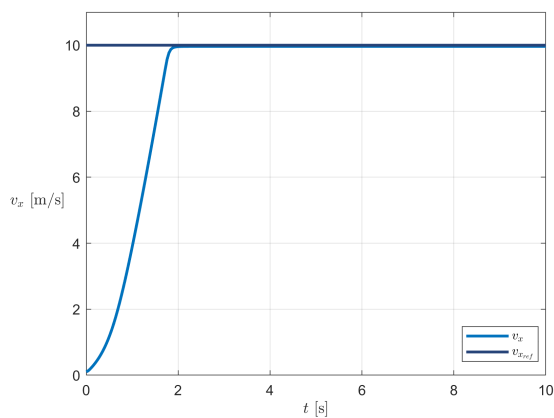
(a) Step
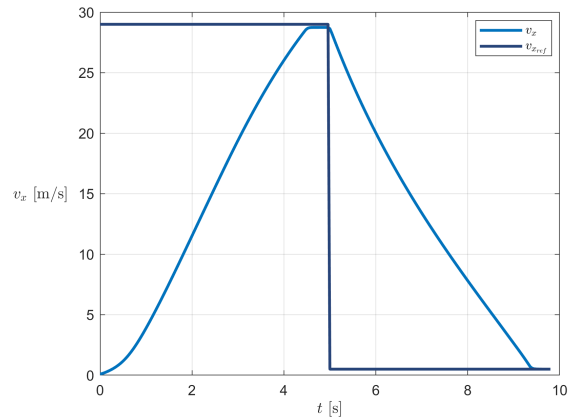
(b) Acceleration event

Figure 5.1: Longitudinal speed responses for design and validation scenarios

Analysing now the tire slip ratios and motor torques responses for the acceleration event — which are provided on the left side subfigures of Figure 5.2 — two comments must be made. Regarding the tire slip ratios it can be seen that, as expected, the values are different for wheels with different axles and that the qualitative relationship between them in acceleration is the inverse of the one found in deceleration. With respect to motor torques, the high motor inefficiency at low speeds stands out which, although facilitating the beginning of the acceleration event, also creates a substantial discrepancy between the torque command and the effective value.
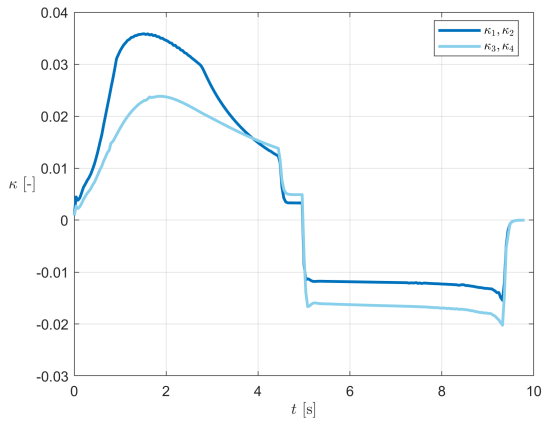
(a) Tire slip ratios for acceleration event
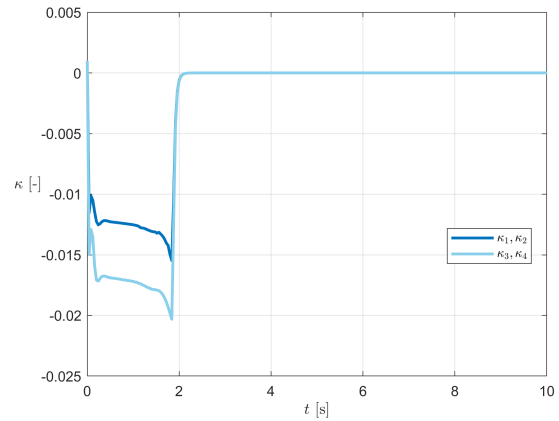
(b) Tire slip ratios for a braking step
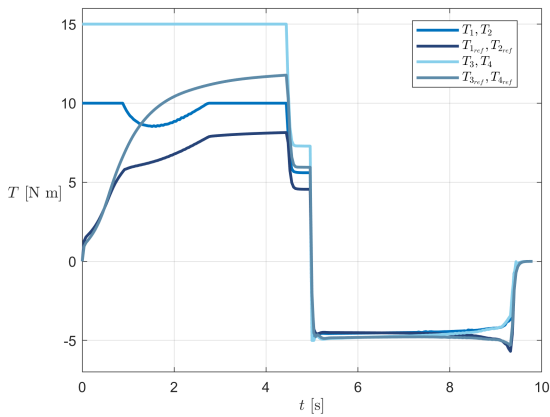
(c) Motor torques for acceleration event
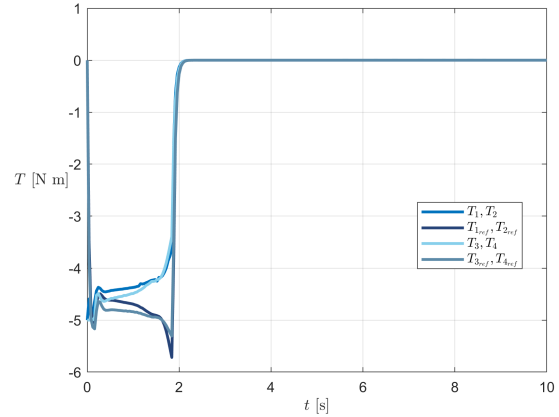
(d) Motor torques for a braking step

Figure 5.2: Tire slip ratios and motor torques for the acceleration event (left) and a braking step (right)

Lastly, a remark regarding the brake is still needed since, as mentioned in Chapter 4, a qualitative analysis was done in order to understand the effects of using only one set of gains instead of a switching control. Considering the results shown in Figure 5.2 — which were obtained for the acceleration event and a -10 [m/s] step — and analysing the torque response, it is possible to see that, although the higher values, in absolute value, correspond to the less loaded wheels, the difference is not significant. By combining this with the response of the slip ratios — where both values are adequate as they are in the ascendant part of the force-slip curve —, it is possible to conclude that this approach leads to a safe control. Keeping in mind that the second part of the acceleration event corresponds to a somehow

extreme situation of deceleration — and yet the load transfer is not enough to have a clearly higher slip ratio in the rear wheels —, since the vehicle will operate mostly in less demanding decelerations, it can be assumed that using only one set of gains, instead of switching, is indeed a suitable approach.

Now that three of the longitudinal gains, namely K_{v_x}, K_κ^F and K_κ^R are obtained, the tuning can proceed in order to set the gain related with the lateral component, $K_{\dot\psi}$. Since it was noted that any non-zero value allowed to verify the qualitative requirement — referenced in Chapter 4 — related with the relation between the inner and outer slip ratios while curving, the design was complemented with meeting the time response requirements presented in Table 5.2. The rise time and the steady state error were chosen as metrics since the former captures the speed of the transient response, while the latter ensures adequate tracking of a constant yaw rate reference, as suggested in [30].

Table 5.2: Lateral performance requirements and respective response

Notation	Description	Requirement	Response	Units
t_r	Rise time	<0.30	0.25	s
e_{ss}	Steady-state error	<0.01	0.008	rad/s

Similarly to what was previously done, the results are graphically shown in Figure 5.3 and in Table 5.2, from which it is possible to see that all the requirements were met. The final gains are presented in Appendix A as well as the values for the saturations used — which were establish as the ones suggested in [30].
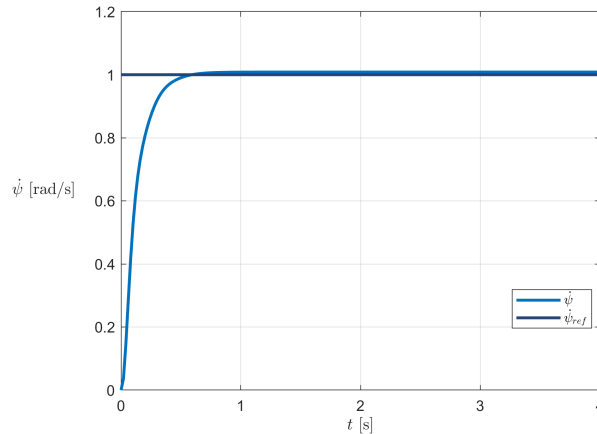
Figure 5.3: Yaw rate step for a constant speed of 9 [m/s]

Lastly, regarding the saturations, it is important to comment about the symmetry and asymmetry related with κ_{diff} and κ, respectively. The minimum and maximum slip ratio differences should be equal, in absolute value, as there is no preferential turning side. However, due to regenerative braking constraint, and considering the maximisation of the acceleration performance as more important than deceleration, a conservative lower bound can be chosen making the slip ratio range asymmetric.

5.1.2 Skidpad

As mentioned before, the skidpad consists of an event that assesses the pure lateral performance in a steady-state cornering manoeuvre. Hence, it will be used as a preliminary basis for observer and controller designs, which will be both presented in the next subsections.

5.1.2.1 Observer

Some of the control strategies require feeding back variables that are not accessible, such as the lateral velocity v_y and the yaw rate $\dot{\psi}$ for the LQG controller and the rate of change of the cross-track error $\dot{e}_y$ for the MSM controller. Therefore, it is necessary to develop estimators to provide the referenced variables.

Using the models provided in (2.39) and (2.47), two Kalman-Bucy observers were implemented, having the respective covariances presented in Appendix A. In order to validate the estimators, one of the skidpad circumference was described at two different constant speeds, namely 5 and 8 [m/s], where this last value was chosen since 9 [m/s] represents the limit speed at which such circumference can be performed, as it will be explained in the next section. Defining the error for a given variable as the difference between its actual value and its estimation, the mean and root mean square (RMS) of such error is shown in Table 5.3, for both velocities and for all the three states. For the lower speed, the variable and its estimation are also shown graphically in Figure 5.4.

Table 5.3: Estimation results

v_x [m/s]	Variable	Simplified Model		Realistic Model		Units
		mean	RMS	mean	RMS	
5	e_{v_y}	-0.001	0.013	-0.036	0.043	m/s
	$e_{\dot{\psi}}$	-0.001	0.020	-0.021	0.043	rad/s
	$e_{\dot{e}_y}$	0.001	0.026	-0.032	0.101	m/s
8	e_{v_y}	-0.011	0.030	-0.144	0.159	m/s
	$e_{\dot{\psi}}$	-0.006	0.055	-0.061	0.126	rad/s
	$e_{\dot{e}_y}$	-0.006	0.069	-0.150	0.275	m/s

Regarding the results for 5 [m/s], it can be seen from Table 5.3 that the tracking is almost perfect in both models, being slightly worse in the realistic one were some differences between the estimation and the real value exist — which are more easily detected in Figure 5.4. These differences can be attributed to nonlinearities since, although both simplified and realistic models are nonlinear, the former represents a far less complex model and, as such, the consequences of this effect are more evident in the latter. Nevertheless, the observer still manages to portray the general tendency of the state being estimated.

Comparing the results for both speeds, it is easily seen that the error increases with velocity, which was expected as it must be kept in mind that, although a gain scheduling was implemented in order to help the estimator to keep up with the variations created by velocity and to try to mitigate the effect of nonlinearities, it still continues to be based on linear models.

Nonetheless, based on the results shown, the observers implemented were considered adequate for control purposes.
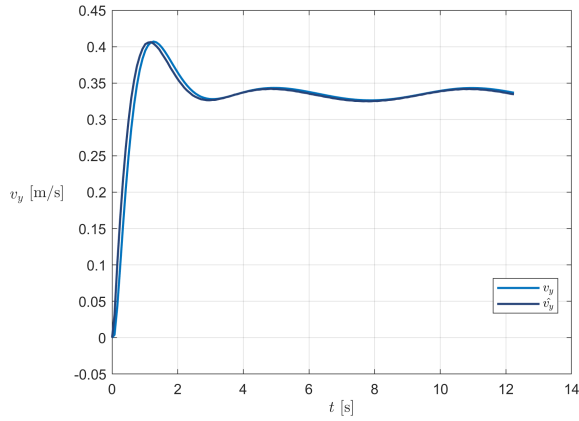
(a) Lateral velocity in simplified model
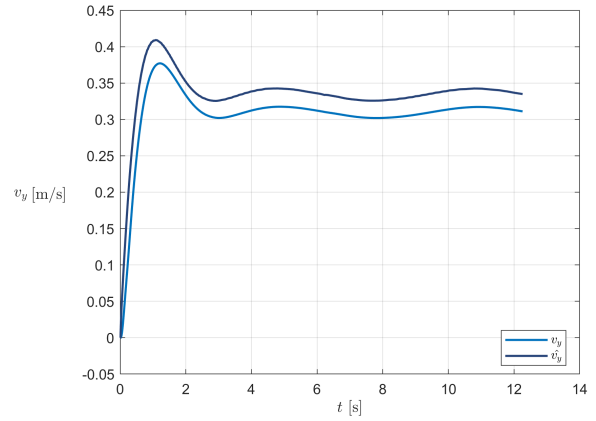
(b) Lateral velocity in realistic model
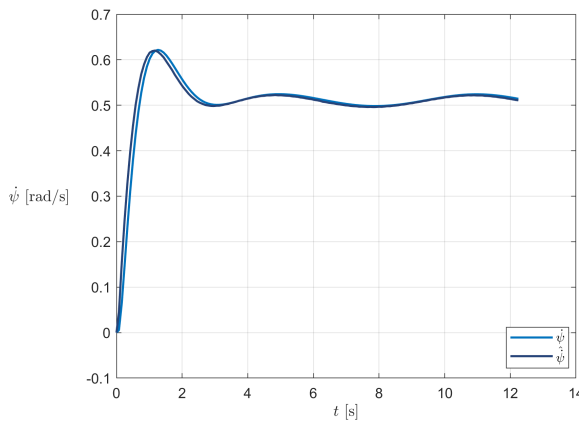
(c) Yaw rate in simplified model
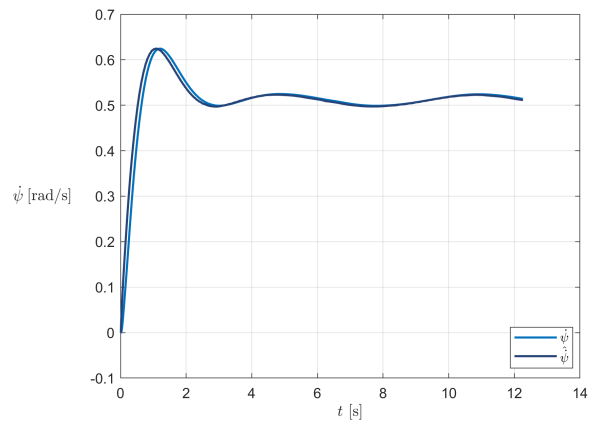
(d) Yaw rate in realistic model
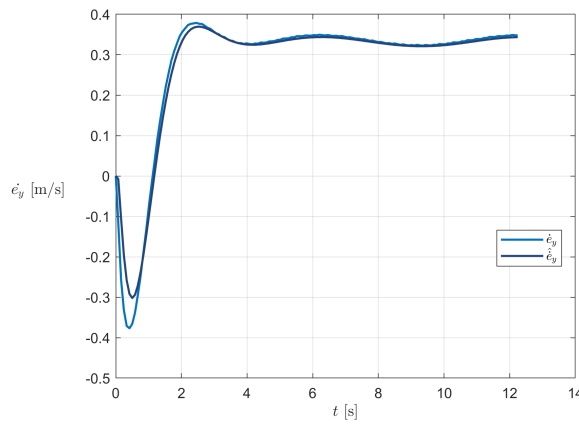
(e) Rate of change of the lateral error in simplified model
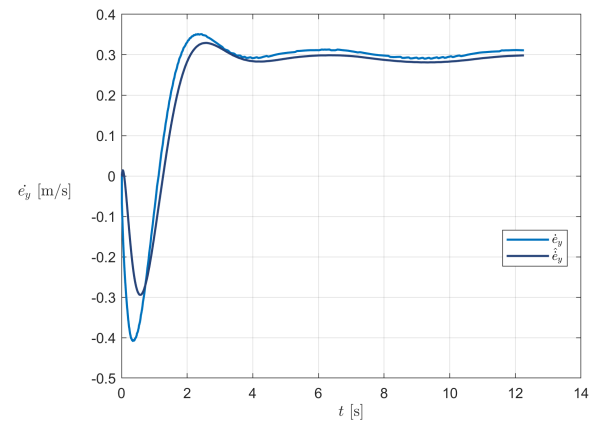
(f) Rate of change of the lateral error in realistic model

Figure 5.4: Comparison between the variables and their estimation for the simplified and realistic models for a longitudinal speed of 5 [m/s] where the hat ˆ denotes the estimated variable

5.1.2.2 Controllers

Following the presentation of the observers' implementation, the development of the lateral control strategies will be now addressed. Since the path used as reference was the centerline — which does not correspond to an optimal solution, as a circumference with lower radius could be used to obtain a faster lap — the time was the only criterion used to evaluate the performance and the cross-track error was considered adequate if it allowed to complete the course without touching the plastic cones. From the time, the corresponding score given by [38]

$$\text{Score} = 71.50 \left(\frac{\left(\frac{t_{\max}}{t} \right)^2 - 1}{1.25} \right) \tag{5.3}$$

was also computed, where — adapting to the present concept — $t_{\max}$ is 1.5 times the time of the fastest controller and t is the time for the controller in question.

The results are presented in Table 5.4 in which a look-ahead was used for three of the controllers, namely the PP, Alice — which, for these controllers, is mandatory — and the LQG — which, although being optional, was beneficial allowing to perform the skidpad at a higher speed when compared with the scenario where no look-ahead was used. The look-ahead analysis will be performed for the trackdrive since this distance, varying with speed, is more relevant in the context of such event, influencing the cross-track error, which was not considered to evaluate the performance here.

Table 5.4: Skidpad results

Controller	Best t [s]	Score
PP	6.29	65.83
LQG	6.39	62.01
Alice	8.28	13.80
KLS	6.29	65.83
MSM	6.15	71.50

From the results presented it is clear that the minimum time was achieved by the MSM controller. The reason for the discrepancy, comparing it with the remaining, is due to the cross-track error since, being higher, allowed to describe a circumference with a lower radius. It is, however, important to mention that the referenced error could be decreased with fine tuning, having been possible to obtain a time of 6.28 [s], which is very close to the values of the remaining controllers. Nevertheless, this was not done since the intention was to obtain a global set of parameters for each controller — in the sense that the same set could be used for the skidpad and trackdrive events — and the ones used to achieve the values presented in Table 5.4 allowed for a better performance in the trackdrive event — which was considered more important as the possible scores for this event are higher in the FS competition. Additionally, taking in consideration, once again, the fact that the reference path used was not optimal, how well the reference was followed was not considered as extremely relevant.

Regarding the worst performance, obtained with the Alice controller, it can be explained by the lon-

gitudinal speed at which the event was completed, since this controller was only able to perform the skidpad at 7 [m/s] while the others performed at 9 [m/s]. This means that, from the robustness point of view, they are all very similar excluding Alice. However, it is important to understand that the upper bound of 9 [m/s] at which the controllers were able to finish the skidpad event was not related to the robustness of the controllers, but due to a loss of traction instead — as it can be seen from Figure 5.5.

(a) Described path at $v_x = 9$ [m/s]

(b) Described path at $v_x = 10$ [m/s]

(c) Slip angles at $v_x = 9$ [m/s]

(d) Slip angles at $v_x = 10$ [m/s]

(e) Lateral force at $v_x = 9$ [m/s]

(f) Lateral force at $v_x = 10$ [m/s]
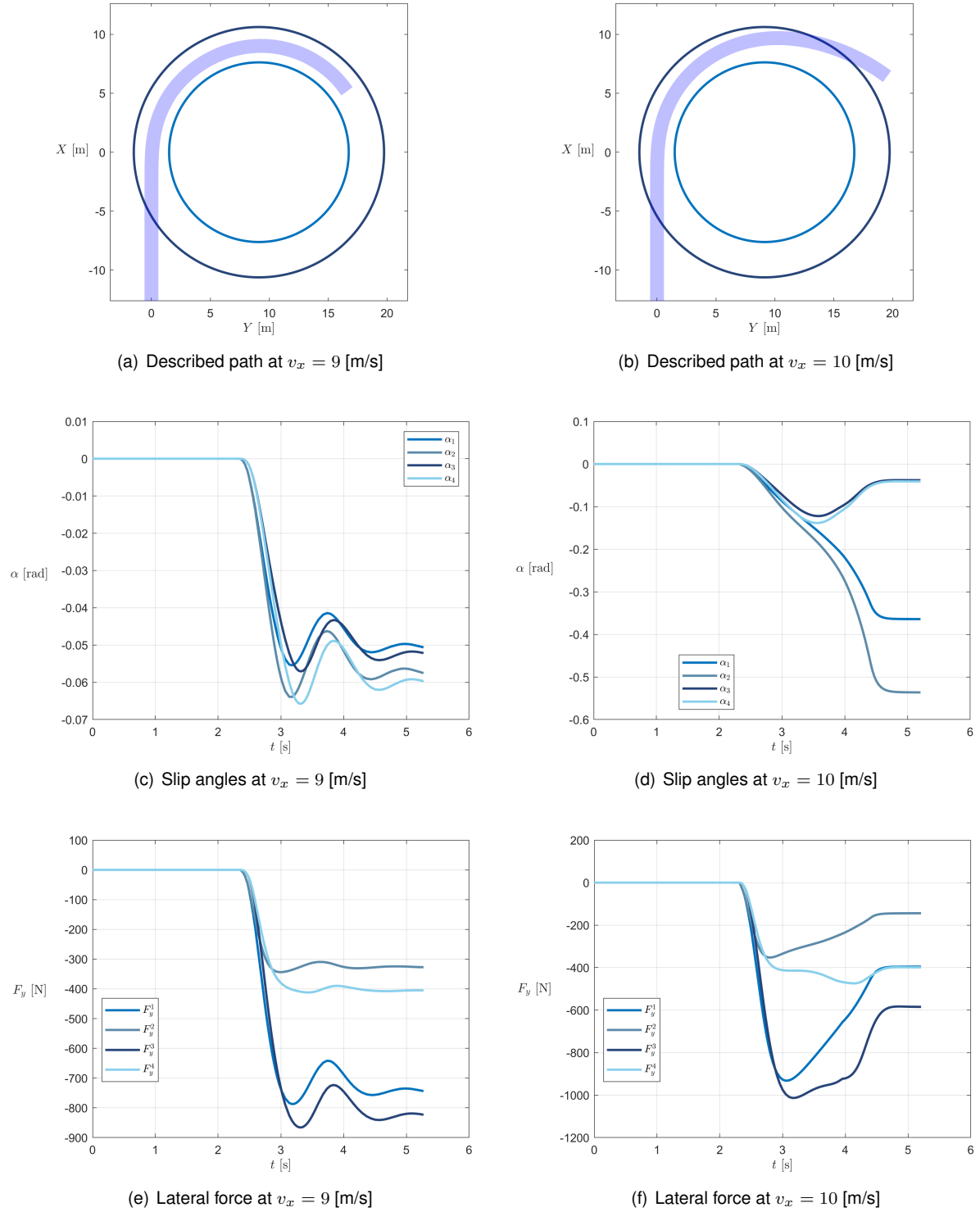
Figure 5.5: Part of the described path and corresponding slip angles and lateral forces for the skidpad event at two different speeds

Analysing the slip angles and the corresponding lateral forces for a higher longitudinal speed — which are provided in Figure 5.5 for a value of 10 [m/s] —, the referred loss of traction can be easily detected. From Figure 5.5 (d) it is possible to see that, for the front wheels, the slip angles are significantly larger than 0.1 [rad] — value corresponding to the maximum force — meaning that the force will decrease abruptly which is, indeed, visible in Figure 5.5 (f). So, even if the slip ratio is within the proper limits — which it is as there is an active control of such variable — the slip angles are leading to a loss of traction. So, one of two alternatives has to be done, namely reducing the speed or reducing the steering angle. Being the latter not possible in order to complete the event, the longitudinal speed must be decreased. As, for a value of 9 [m/s], the behaviours of the slip angles and lateral forces are according to what is expected, it was concluded that, due to traction, this corresponds to the admissible limit for the longitudinal speed in the skidpad event.

Concerning the relation between the slip angles for both front wheels another remark can be made. From Figure 5.5 (d) it can be easily perceived that, in terms of stability, the inner front wheel ($i = 2$) is the critical one, as it is the first to destabilise, meaning that the steering was too high. Since, due to the tire model used, the Ackermman kinematic steering was implemented — which does imply a higher steering angle in the inner front wheel ($i = 2$), relatively to the outer front wheel ($i = 1$) —, such results suggest a possibility of achieving better performance using another tire model that allows for the implementation of the anti-Ackermman geometry. However, such analysis is out of the scope of this work.

Lastly, it should be stressed out that the reference path could be changed, as mentioned, in order to be closer to the inner cones which, in a real scenario, will allow better performance as, for the same speed, the decrease of distance leads to a decrease of time. However, this was not done since, bearing in mind that this improvement in performance would occur for all controllers and that the analysis was done on a comparative basis, no further enrichment would be achieved.

5.1.3 Trackdrive

Representing a traditional approach to racing, the trackdrive event has, as its goal, the minimisation of the lap time around a generic race track, which can be achieved with two different approaches: considering the optimisation of the path and the speed profile simultaneous or individually. Being the latter the one followed in this work, the reference path was obtained resorting to artificial potential fields, where the attractive force was simulated through two different methodologies — schematically represented in Figure 5.6. However, as it can be seen from Figure 5.7, just the one that selects the target point from the centerline led to satisfactory results.

The behaviours described by both approaches can be easily understood through Figure 5.6. Comparing both situations, it becomes clear that, due to the attractive force direction, the vehicle will be more repelled in (a), as in (b) some of the attractive force will counteract the repulsive force. Seeing that, in the proximity of the other track limit, this phenomenon resurfaces, an oscillatory behaviour is induced in (a) — until the dissipation of kinetic energy occurs, similar to what happens in water slides — while in (b) the vehicle tends to cut corners — since the direction of the attractive force can be such that, in addition

to counteracting the repulsive force, it still forces the car to climb the potential hill. These behaviours can also be explained from a control point of view: the establishment of the target in (a) only depends on the present moment — as it is obtained from the current direction — whilst in (b) the information about the track is introduced which allows to account with what will happen next. From a control perspective, this introduces a feedforward term which enables a predictive behaviour. Due to what was mentioned, only the approach (b) was used in the sweep procedure to obtain the reference path.

(a) Defining the target point with a straight line

(b) Defining the target point with the centerline
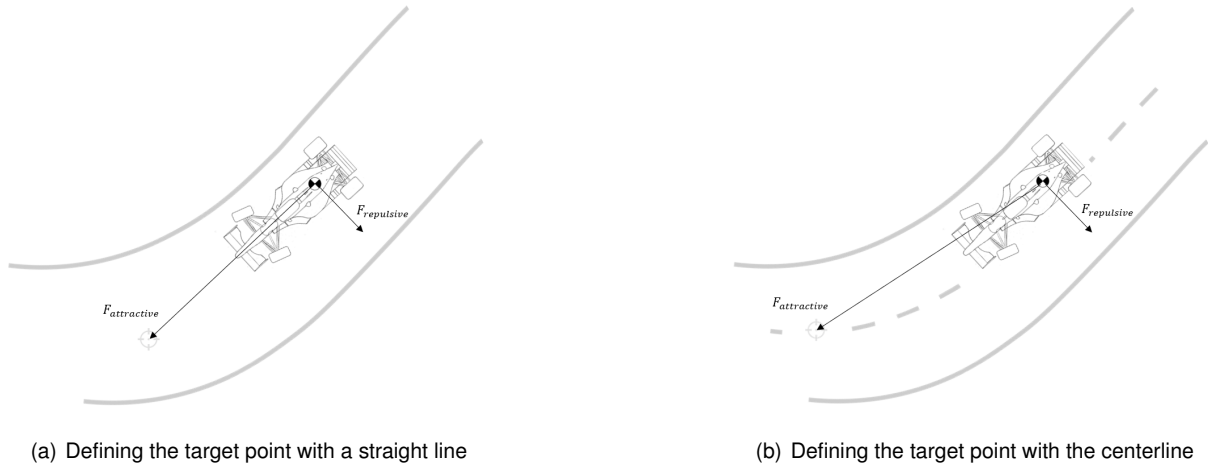
Figure 5.6: Schematic of the two different attractive forces

(a) Defining the target point with a straight line

(b) Defining the target point with the centerline
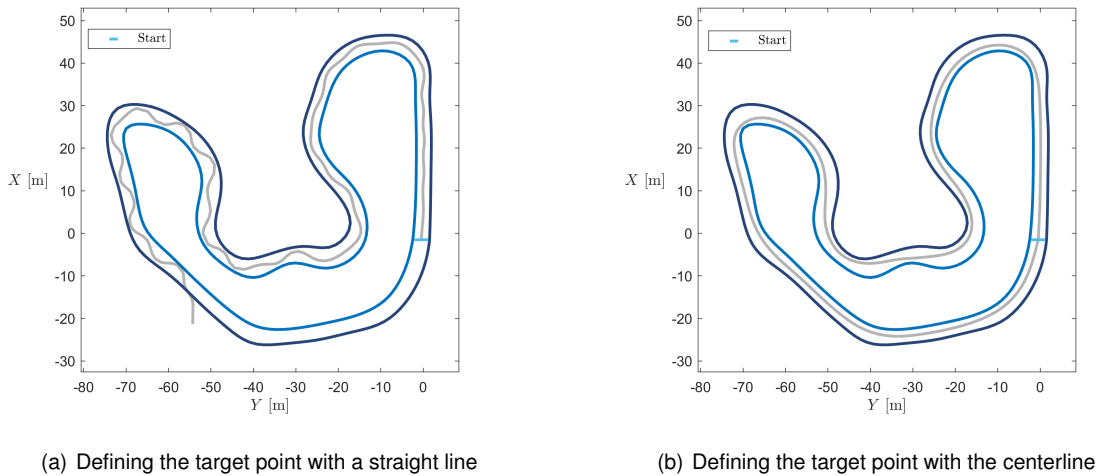
Figure 5.7: Results for FSG track for the two methods related with the attractive force

With respect to the speed profile, four remarks must be made. Firstly, the stand still configuration was defined with a initial speed of 0.1 [m/s], instead of a null value, in order to avoid the software singularity configuration, as the models are based in non-null speeds. Secondly, to ensure not entering in the zero-torque/zero-power zone, the speed upper bound was not defined as the actual maximum speed of the vehicle, but as 26.5 [m/s] instead — obtained from establishing 18 000 [rpm] as maximum motor speed, which allows to preserve the powertrain. Thirdly, the efficiency was set to a moderate value of 70 [%] to take into account that not all losses were modelled. Lastly, it should be also stressed out that the algorithm only provides speeds for waypoints. Thus, to obtain a smoother and more continuous profile,

the vehicle position is projected on the path and a reference speed between waypoints is obtained by weighting the speeds provided by the algorithm at the two closest waypoints.

With the parameters needed to obtain both references presented in Appendix A, the results can be found in Figure 5.8 and Table 5.5.

(a) FSG reference trajectory

(b) FSG curvature comparison

(c) FSI reference trajectory

(d) FSI curvature comparison

(e) Thin reference trajectory

(f) Thin curvature comparison
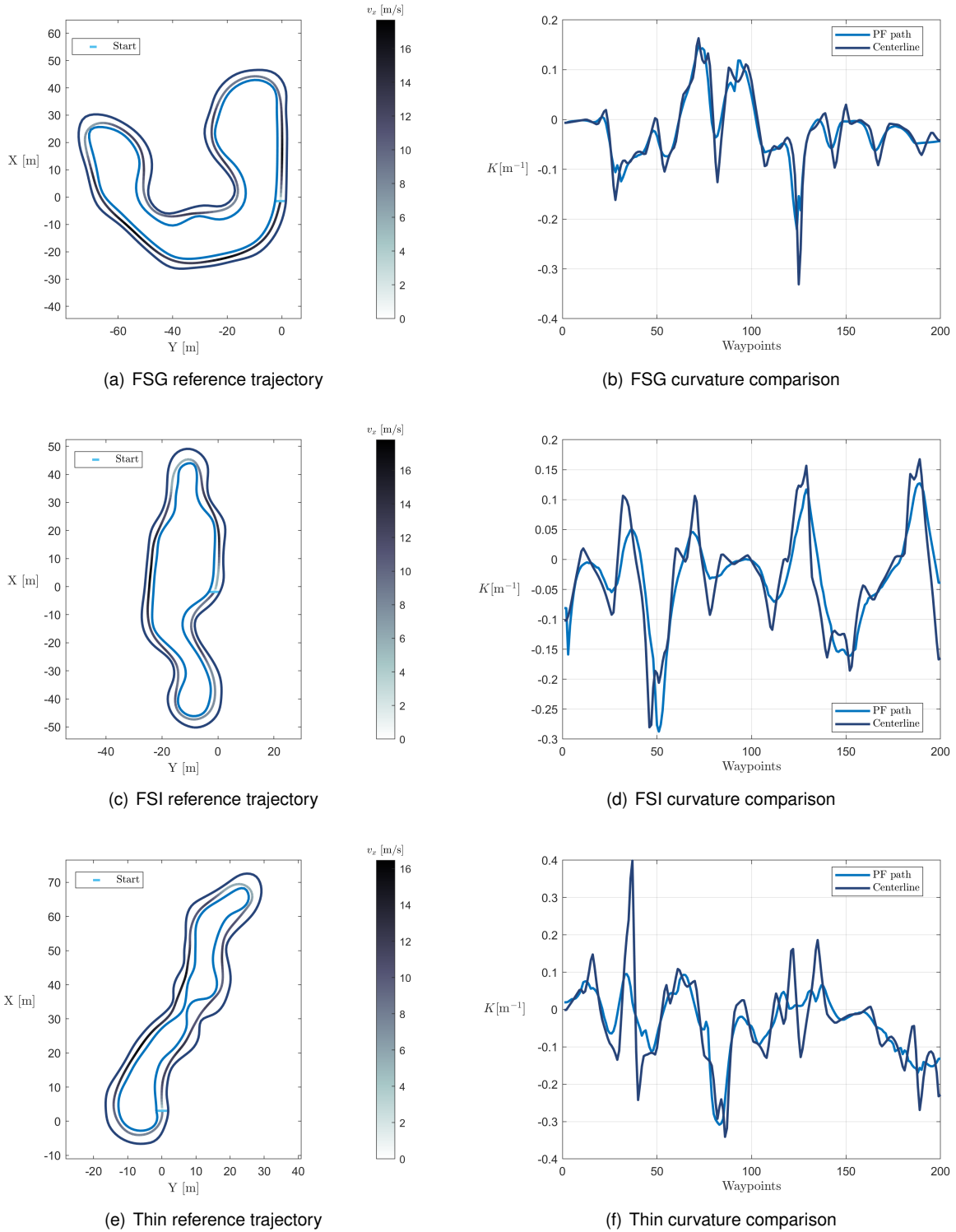
Figure 5.8: Reference trajectory and curvature comparison for each track. In the former, the color indicates the reference speed of the racecar with the respective values presented in the colorbar: the darker the color, the higher the reference speed will be

65

Table 5.5: Comparison between the time spent to travel the centerline and the solution obtained by the artificial potential field (PF) method for each track

| Track | Centerline | PF path | Improvement | |
			s	%
FSG	30.86	27.00	3.86	12.50
FSI	24.43	21.59	2.84	11.63
Thin	22.91	18.15	4.76	20.78

From Table 5.5 — where a comparison with the centerline was made as this corresponds to a common reference path — it is clear what was mentioned about the centerline solution: it leads to a significant loss of time in turns since in the PF solution, where the vehicle tends to cut corners like a human driver, a decrease in the lap time occurs. This effect is more notorious in the Thin track — in which the solution found can improve the lap time by almost two times more than for the remaining ones — since this is the most intricate of the three tracks, so the decrease in the reference path curvature is higher — as it can be seen from Figure 5.8 (f).

From the trajectory shown in Figure 5.8, it is visible that the vehicle cuts corners while driving slower in corners and faster on straights, so the final solution captures well the expected behaviour of a human driver. Since, from the referenced figure, the validity of the solutions obtained is not clear — in the sense that the distance between the path and the limits cannot be perceived adequately — a complementary information is given in Table 5.6 where the minimum distance to the inner and outer limits is shown. These results prove that it is possible for the vehicle to perform the path without touching the plastic cones, as all values are higher than half of the track width of the car. Lastly, it should be noted that, if a more conservative path is desired — increasing the distances presented —, this can be easily obtained by changing the parameters related to the sweep performed in the potential field approach — offset, γ, K_{rep} — or even the minimum distance in the potential shape — $d_{\min}$.

Table 5.6: Minimum distance between the path obtained and the track limits

| Track limit | Distance | | | Units |
	FSG	FSI	Thin	
Inner	0.82	0.87	0.78	[m]
Outer	0.92	1.15	0.92	[m]

With both reference path and speed profile obtained, the controllers performance in the trackdrive event can be evaluated recurring to suitable metrics. Considering that the reference path is intended to represent a solution closely to an optimal, the cross-track error is an important factor to take into account and, as such, the RMS of the cross-track error was used as an evaluation parameter. Distinguishing a line from an arc of circumference if the curvature of the path between two waypoints has an absolute value below 0.002 $[\text{m}^{-1}]$, this error can be computed by

$$e_y = \begin{cases} \frac{\mathbf{d}_{i,i+1} \times \mathbf{d}_{i,P}}{\|\mathbf{d}_{i,i+1}\|} & \text{if } |K_{i,i+1}| < 0.002 \\ \text{sign}(R_{i,i+1}) \cdot \left(|R| - \| \mathbf{d}_{\text{PC}} \| \right) & \text{otherwise} \end{cases} \quad \text{[m]} \tag{5.4}$$

The second metric concerns the steering, consisting in the RMS of the difference between the actual steering and the same values smoothed by a median filter, since this control action should be smooth in order to drive the vehicle gently and to avoid undesirable oscillation, which could be harmful for the car's components. The third and last metric consists in the lap time, since the main objective in such event is finishing it as fast as possible. Derived from the time, the score was computed according to [38]

$$\text{Score} = 150 \left(\frac{t_{\text{max}}}{t} - 1 \right) \tag{5.5}$$

where — adapting to the present concept — t_{max} is 2 times the time of the fastest controller and t is the time for the controller in question. However, a remark should be made. Although, as stated in Chapter 3, this event consists in performing ten laps of the autocross track, only the first lap is considered for analysis, as it is more demanding in terms of traction control due to the stand-still start. It is expected that, if there is no drastic change in traction condition and the first lap was completed without driving off-track, the remaining nine should be quite similar, as the reference trajectory is not updated online [30].

Lastly, remembering that some of the implemented control strategies require — as in the case of PP and Alice controllers — or could benefit from — in the case of the LQG controller — the use of a look-ahead distance, and keeping in mind that such distance should change with the longitudinal speed, the performance for such controllers was evaluated for two types of look-ahead profiles, namely a linear [52] and a parabolic [53] one, both present in (5.6).

$$L_{lad_1} = L_{lad}^{\text{const}} + t_{\text{react}} v_x \quad \text{[m]} \tag{5.6a}$$

$$L_{lad_2} = L_{lad}^{\text{ref}} \left(\frac{v_x^2}{v_{x_{\text{ref}}}^2} \right) \quad \text{[m]} \tag{5.6b}$$

The parameters used in both profiles are presented in Appendix A.

The results for this event are presented in Table 5.7 where two columns were added to provide additional information. The first contains the mean of the look-ahead distance $\overline{L_{lad}}$ whereas the second qualitatively informs if, in the path actually described, the vehicle touched the cones, but still managed to remain in the track — being signaled a penalty — or if the vehicle did not finish the course — which will be shown as DNF.

Beginning the analysis with the cross-track error, it can be highlighted that the PP, LQG and KLS controllers present a similar performance in all of the tracks being the difference between the MSM and these controllers not significant and possibly diminished with further tuning. However, the Alice controller stands out, once again, with low performance, having the higher cross-track error. This could be attributed to the inherent environment where such controller was developed, as in the DARPA challenge

the road had a large width and the cross-track error was not a factor of interest [44]. Nevertheless, a more detailed analysis was carried out in order to try to explain the reason.

Table 5.7: Trackdrive results

Track	Controller	L_{lad}	$\overline{L_{lad}}$ [m]	RMS(e_y) [m]	RMS(e_δ) [°]	t [s]	Score	Penalty
FSG	PP	1	3.57	0.05	0.015	27.62	146.67	–
		2	4.68	0.07	0.013	27.59	150.00	–
	LQG	1	3.66	0.04	0.009	27.69	148.92	–
		2	–	–	–	–	–	DNF
	Alice	1	3.57	0.36	0.044	28.40	141.44	–
		2	4.89	0.45	0.043	28.55	139.91	–
	KLS	–	–	0.05	0.027	27.67	149.13	–
	MSM	–	–	0.10	0.022	27.62	149.67	–
FSI	PP	1	3.17	0.07	0.037	22.15	149.73	–
		2	3.43	0.12	0.038	22.19	149.19	–
	LQG	1	3.32	0.05	0.017	22.26	148.25	–
		2	–	–	–	–	–	DNF
	Alice	1	3.21	0.30	0.047	22.81	141.06	–
		2	3.84	0.79	0.052	23.84	128.48	YES
	KLS	–	–	0.05	0.046	22.13	150.00	–
	MSM	–	–	0.11	0.046	22.13	150.00	–
Thin	PP	1	3.23	0.08	0.018	18.72	150.00	–
		2	–	–	–	–	–	DNF
	LQG	1	3.35	0.05	0.010	18.79	148.88	–
		2	–	–	–	–	–	DNF
	Alice	1	–	–	–	–	–	DNF
		2	–	–	–	–	–	DNF
	KLS	–	–	0.08	0.034	18.82	148.41	–
	MSM	–	–	0.10	0.023	18.76	149.36	–

Since both Alice and PP are geometric controllers, a comparison between the linearised version of such controllers was performed. Linearising (4.16) and (4.10) — where, for the latter, the case following a straight line was used [47] and combined with the expression of $\dot{e}_y$ obtained from (2.44) in order to have the equation written with respect to the cross-track and heading errors — the following expressions can be obtained:

$$\delta_{\text{Alice}} = \frac{L + L_{lad}}{L_{lad}}e_\psi + \frac{1}{L_{lad}}e_y \qquad \text{[rad]} \tag{5.7}$$

$$\delta_{\text{PP}} = \frac{2L}{L_{lad}}e_\psi + \frac{2L}{L_{lad}^2}e_y + \frac{2L}{L_{lad}}\frac{v_y}{v_x} \qquad \text{[rad]} \tag{5.8}$$

The first noticeable difference between the above expressions is the additional term present in the PP controller. Comparing this term with (2.33) it can be seen that it corresponds to a linear version of the sideslip angle which means that, contrary to the Alice controller, the PP controller takes into account the slip. Nevertheless, the gains related with the path-following errors are different, so it is necessary to see if this additional term is the only reason for the discrepant behaviour or if the performance is also influenced by the evolution of such gains with the look-ahead. Considering the variation of the look-ahead mean presented in Table 5.7, a numerical substitution was performed within a range of [3, 5] [m] and the ratio between the gains associated with the error analysed, being the results presented in Figure 5.9. Since both errors are fed back, the ratio between the cross-track and heading errors is related to the inverse of the derivative time constant. So, from the figure, it can be concluded that, although the evolution is similar in both controllers, the Alice presents a higher derivative time constant which means that this controller is more reactive, having a higher bandwidth and, consequently, being less robust, which could explain the lower performance that was found.
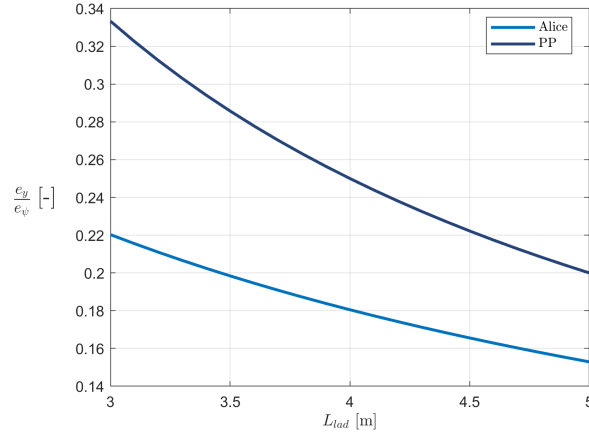
Figure 5.9: Inverse of the derivative time constant for the PP and Alice controllers

Returning to a more general analysis — in the sense that all the controllers are considered once again — some tests were performed using the centerline as reference path. Although these tests are not presented, it was noticed that the cross-track error increased which can be explained by the general increase of the curvature — which can be seen from Figure 5.8 — making it harder to track with the same precision as in the path used.

With respect to the metrics concerning the steering, the values obtained are extremely low due to the time constant τ_{SA} used in (2.12), which allows to obtain a smooth control action. Using an additional decimal place in order to give further information about the comparison between the different controllers, it can be seen that the LQG is usually the one with the lowest value by opposition to the Alice controller which typically presents the highest value.

Regarding the look-ahead analysis, the most clear conclusion is that the linear profile enables all controllers to finish all tracks — except Alice in the Thin track — and allows for a better performance, with respect to the cross-track error. This can be explained by how the speed influences this predictive distance. As it can be perceived through Figure 5.10, the variation in the parabolic profile is considerably

more significant, which means that it will result in higher values for the distance, leading the controllers to correct their position prematurely and, consequently, losing part of the benefit associated with this concept. This occurrence is in accordance with what usually happens in the behaviour of a driver: being the predictive distance dependent not only on speed, but also on curvature, it is usually smaller for larger curvatures, which can be better achieved with the linear profile used as it presents, in general, lower values. Lastly, comparing the PP and Alice controllers with the LQG, it is clear that the latter is more sensitive, or less robust, to the changes in the look-ahead distance, as it was the one that was not able to finish any of the tracks with the parabolic profile.
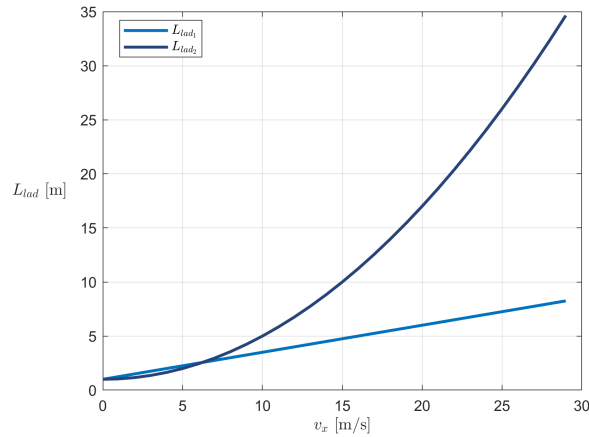
Figure 5.10: Look-ahead profiles

Weighting all comments and results presented, it was considered that, with the exception of the Alice controller, the different control strategies implemented correspond to adequate solutions for vehicle guidance.

5.1.4 Autocross

As mentioned before, the approach developed for the trackdrive event requires knowledge about the track layout, due to the offline optimisation performed. However, to do so, a track mapping is needed, which can be performed during the autocross event since, in the driverless competition, the same track is used for both [38].

The control strategy used in this event is not based on typical variables such the cross-track and heading errors, but rather on artificial potential fields. As such, from the lateral subsystem point of view, the control is made without a reference path, meaning that the guidance is an exclusive and direct result of virtual forces. However, the same can not be said for the longitudinal subsystem, where two different methods were developed to obtain a reference speed: the centerline and the critical radius approaches. From those, the latter requires the establishment of "dynamic breakpoints" — in the sense that the radius defining the different zones should change with speed — to perform a cubic interpolation. The points used are shown in Table 5.8, where $v_{x_{\max}}$ was set to 15 [m/s] — roughly half of the actual maximum speed of the vehicle — for safety reasons as, without knowledge of the track layout, a more conservative stance is needed.

Table 5.8: Points used for cubic spline interpolation

Radius	Distance [m]	Velocity [m/s]
R_O	$1.5\ v_x$	$v_{x_{max}}$
R_W	$1.2\ v_x$	$v_{x_{max}} - 2$
R_D	$0.9\ v_x$	$\dfrac{v_{x_{max}}}{2}$
R_C	$1.5\ L$	0

To directly compare the two approaches — similarly to what was done in previous events — a score given by [38]

$$\text{Score}_i = 90\left(\frac{t_{\max} - t}{t_{\max} - t_{\min}}\right) \tag{5.9a}$$

$$\text{Score} = \max(\text{Score}_1,\ \ \text{avg}(\text{Score}_1 \dots \text{Score}_n)) \tag{5.9b}$$

was computed, where — adapting to the present concept — $t_{\max}$ is the time for driving the lap at a speed of 4 [m/s], $t_{\min}$ the time of the fastest approach and t_i is the time of run i in the approach in question.

Having each time at least two runs [38], and remembering that the centerline approach benefits from a second run — since the path described in the first can be used to obtain the reference speed in the second —, two runs were simulated for the centerline approach and only one for the critical radius approach. This was done as, for the last approach, a second run is expected to be performed at approximately the same amount of time if there is no drastic change in traction condition. The results are presented in Table 5.9.

Table 5.9: Autocross results

Track	Approach	Run	t [s]	$t_{v_x=4}$ [s]	Score
FSG	Centerline	1	43.94		68.81
		2	42.77	73.99	
	Critical Radius	1	33.92		90
FSI	Centerline	1	35.01		60.79
		2	31.57	50.76	
	Critical Radius	1	24.90		90
Thin	Centerline	1	35.44		49.76
		2	30.00	43.62	
	Critical Radius	1	23.91		90

From the information in Table 5.9, the critical radius approach presents itself as the best solution, allowing for a significant faster lap. Furthermore, analysing the score column and the curvatures associated with the path described in each track — which have the relation $\text{RMS}(K_{\text{FSG}}) < \text{RMS}(K_{\text{FSI}}) < \text{RMS}(K_{\text{Thin}})$ — it is possible to establish that the performance divergence between the approaches increases with the curvature, as expected. A more detailed analysis can be performed resorting to Table 5.10, where the time improvement from the second run of the centerline approach and from the critical

radius approach over the first run are shown, as well as the increase of time of both approaches over the trackdrive event performed with the PP controller using a linear look-ahead profile.

Table 5.10: Comparison between the approaches used in autocross and between these and the one used in trackdrive event

Track	Approach	Run	Improvement		Increase	
			s	%	s	%
FSG	Centerline	1	–	–	16.33	37.15
		2	1.17	2.66	15.15	34.49
	Critical Radius	1	10.03	22.82	6.30	18.58
FSI	Centerline	1	–	–	12.86	36.73
		2	3.44	9.83	9.42	26.90
	Critical Radius	1	10.11	28.89	2.75	11.03
Thin	Centerline	1	–	–	16.71	47.16
		2	5.44	15.34	11.28	31.82
	Critical Radius	1	11.53	32.54	5.18	21.68

Beginning the analysis with the first column of Table 5.10, a sight decrease in time can be verified, as expected, in the second run of the centerline approach since the curvatures used for speed computation are lower. This decrease grows with the number and tightness of the curves present in the centerline, as the artificial potential field tends to cut corners. On the other hand, the significant reduction in time, when comparing both approaches, can be explained by subfigures related with the g-g diagram in Figure 5.11. As these diagrams are useful to understand the dynamic vehicle behaviour in terms of accelerations a_x and a_y — which are typically expressed in [g], with 1 [g] $= 9.81$ [m/s^2] — from the referred subfigures a more demanding diagram can be seen for the critical radius method, which implies a more demanding speed profile. This can be justified by the fact that the actual described curvature can be significantly lower than the one computed from the centerline and/or by the decrease in the look-ahead distance used for speed computation in the centerline approach, as such reduction can occur in excess or even unnecessarily, leading to a more conservative reference.

Regarding the comparison with the trackdrive event, as expected, both approaches present a worse performance and more conservative speed profiles. However, the FSI track stands out with a significant lower increase — when compared with the remaining tracks — which can be explained by the track layout, as it is more elongated then the others. Since, at this event, a more general approach was intended, the parameters were set equal in all tracks — except the offset, that was chosen to provided more or less the same distance in all tracks. As such, the path itself used in the autocross and trackdrive events was not the same; however, being the difference not significant, the decrease in performance was mainly due to a more conservative speed profile.

Lastly, from the subfigures related with the control action, in Figure 5.11, it is visible that both approaches present a noisier response over the one obtained in the trackdrive event, which can be explained by the control action sensitivity to discontinuities. Although the discontinuities associated with

72

the track limits are equal in all the approaches, the ones related with the reference speed are not.
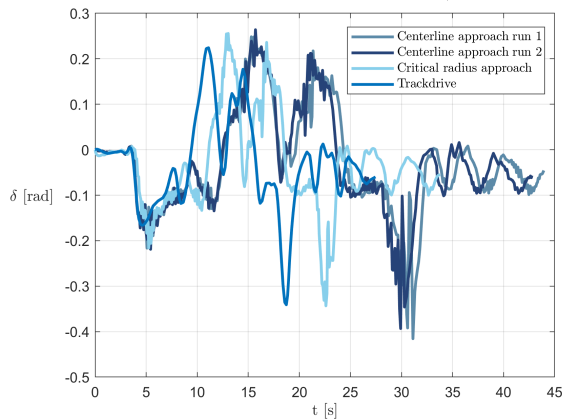
(a) Control action in FSG
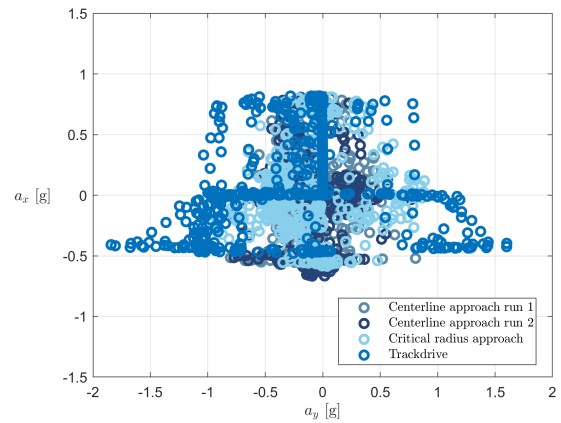
(b) g-g diagram in FSG
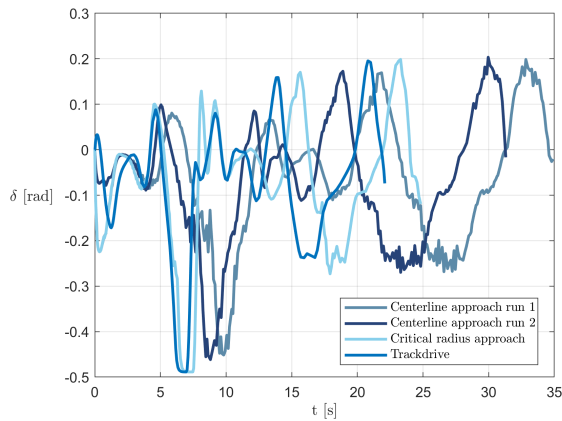
(c) Control action in FSI
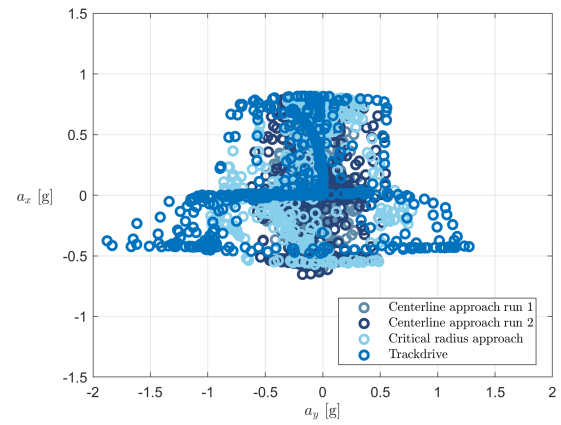
(d) g-g diagram in FSI
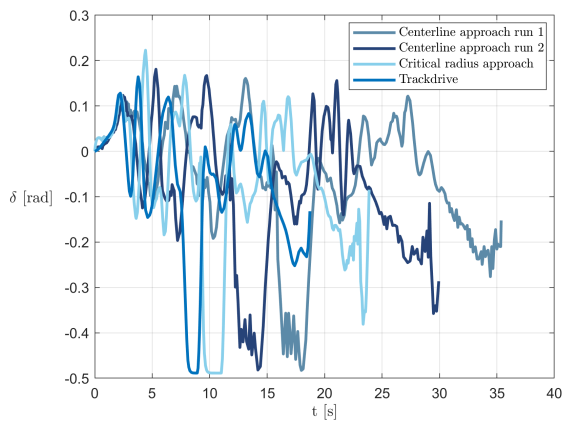
(e) Control action in Thin
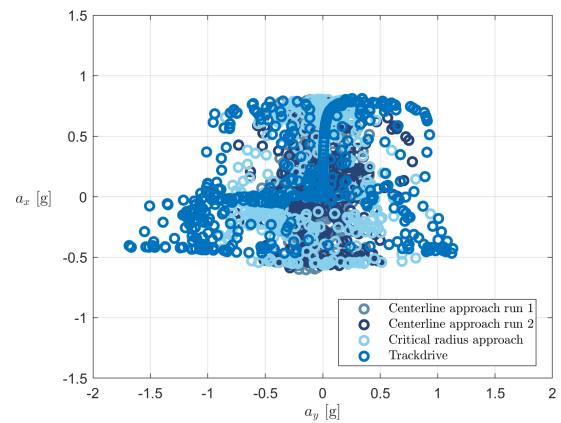
(f) g-g diagram in Thin

Figure 5.11: Control action and g-g diagram comparison for online (centerline and critical radius) and offline (two passes algorithm) approaches in the three tracks

Since the reference speed is obtained directly from curvature computation, in the centerline approach, this is the more discontinuous reference of all three, which will result in a noisier lateral control action, as shown. On the other hand, the critical radius approach allows for a more continuous reference as

it is obtained from a cubic spline interpolation; nevertheless, one should keep in mind that a situation can occur where the limits can be detected and not detected in a short period of time leading to some discontinuities. Being an unusual situation, the discontinuities are less frequent than the ones present in the centerline approach so a less noisier control action was expected which, in fact, happens. Finally, since in the offline approach, used in the trackdrive event, the reference speed is continuous — resulting from the projection of the car's position in the path and weighting the speeds in the nears waypoints — this leads to a better response in terms of noise. Aiming to diminish the noise present in the online approaches, a Butterworth filter was initially developed, but it was found that the consequent phase distortion led to a response lag which, in turn, led to system instability. Although this phenomenon could be mitigated by decreasing the filters order or by bandwidth increase, it is important to take into account the dichotomy between filter's and control abilities and the impact that these measures will have. As such — and since the vehicle itself will also be capable of filtering — the Butterworth filter was not implemented and the control action behaviour was considered satisfactory enough for the current purpose.

5.2   Obstacle Avoidance

Being the last topic addressed in this dissertation an hypothetical scenario in the FS environment — but already existing in other competitions — three tracks were created, for simulation purposes, since the ones related with the FS events are quite narrow, not allowing much room for maneuvering. As stated in Chapter 3, the first track used has a layout similar to the one found in athletic tracks and the other two were obtained by resizing tracks related with [13, 24]. The obstacles, on the other hand, were placed at strategic positions to test for algorithm robustness.

Similarly to what was done in the section related with the trackdrive event, the parameters used are presented in Appendix A and the described trajectory was plotted with the track limits — and, in this case, the obstacles —, changing the line color accordingly with the speed. Such plots are shown in Figure 5.12, where it is possible to see that the system responses regarding steering and speed are much alike to what is expected from a human driver. From a steering point of view, the vehicle is still able to portray quite well what can be considered as an expected path, but some "clumsy" movements can be detected — mainly in track 3. However, this occurs mostly in tight curves and the vehicle still manages to perform them and remain within the track. On the other hand, the behaviour regarding speed presents less flaws, since the speed is decreased in the proximity of an obstacle or in a curve, but increased in straights, as expected. This speed profile was obtained with the critical radius approach as in the autocross event; however, although the maximum speed was set to 15 [m/s], the breakpoints related with the warning and danger zones were shifted down to allow for a slightly higher decrease in the observation zone, but maintaining more or less the relation established in the remaining zones. The points used for the cubic spline interpolation are provided in Table 5.11.

Regarding the path described, comparing Figures 5.8 and 5.12, a greater tendency to approach the centerline is visible when no obstacles are near, which can be easily explained by the offset distance

used to compute the attractive force and the value of the decay factor. As the simulations were intended to represent an unpredictable environment — in the sense that both track limits and obstacles are not known —, the spacing between the points used to compute the centerline was smaller, which leads to a smaller magnitude of $\mathbf{f}_{att}$. Combining this with the value of the γ used, which obliges to a greater distance from the limits due to the decrease in the potential slope, the tendency to cut corners is decreased.
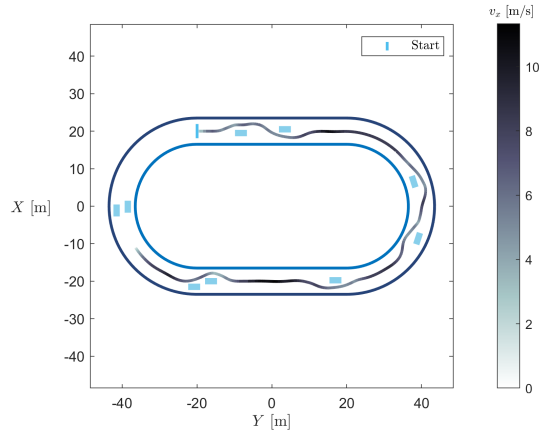
(a) Track 1 reference trajectory
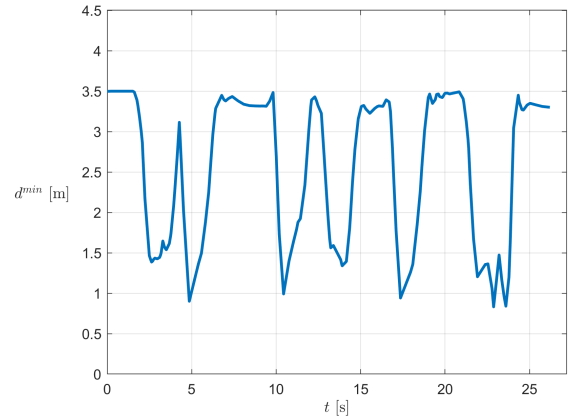
(b) Track 1 minimum distance to track limits or obstacles
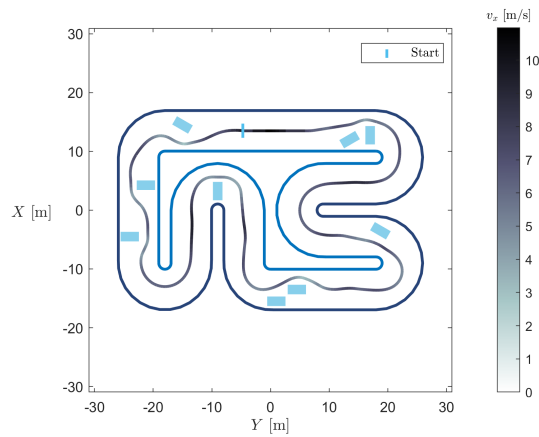
(c) Track 2 reference trajectory
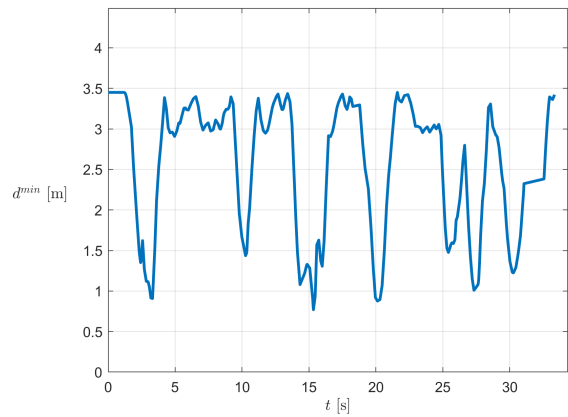
(d) Track 2 minimum distance to track limits or obstacles
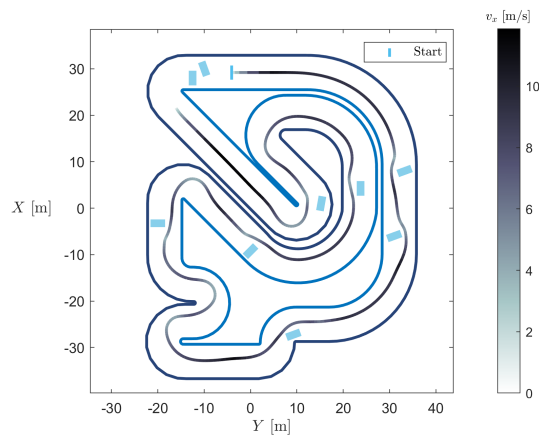
(e) Track 3 reference trajectory
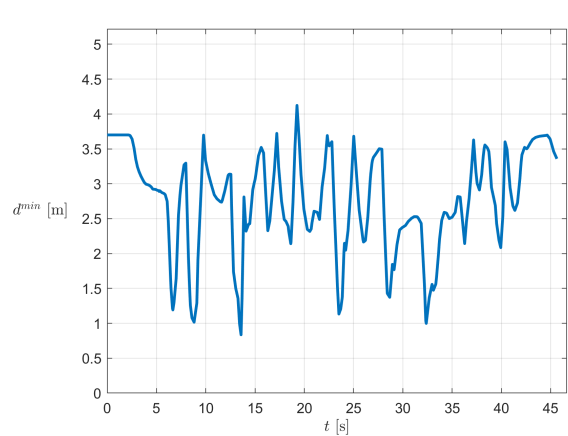
(f) Track 3 minimum distance to track limits or obstacles

Figure 5.12: Reference trajectory and minimum distance to track limits or obstacles for each track

Table 5.11: Points used for cubic spline interpolation in obstacle avoidance

Radius	Distance [m]	Velocity [m/s]
R_O	$1.5\,v_x$	v_{x_max}
R_W	$1.2\,v_x$	$v_{x_\text{max}} - 3$
R_D	$0.9\,v_x$	$\dfrac{v_{x_\text{max}}}{2} - 1$
R_C	$1.5\,L$	0

Caused by the difficulty in assessing the validity of the solution obtained — in the sense that it can be perceived that the vehicle is able to perform a trajectory without crossing the limits or colliding with obstacles —, additional information was provided graphically and resorting to a table. Considering simultaneously both limits and the obstacles, in the right sided subfigures of Figure 5.12 the minimum distance to any of them is shown, where the validity of the solution can be detected, almost always, without a doubt. In order to eliminate any remaining doubts, aroused from some dubious situations, the minimum distance to each one of the limits and to the obstacles is provided separately in Table 5.12. From this table there is no room for uncertainty regarding the validity of the solution, as all the presented distances are higher than half of the track width. However, it is possible to see that the vehicle comes considerably close to the obstacles whereas, in the case of the limits, the vehicle could have come closer and there would still be a satisfactory safety distance. This means that the gains and potentials defined could be further tuned, forcing a higher distance from the obstacles and allowing the vehicle to come closer to the limits. Additionally, the method used to check if some obstacle can be considered as already behind could be changed — to the one where the chosen reference point on the vehicle must be a given distance ahead of the foremost part of the obstacle — to provide an extra safety distance.

Table 5.12: Minimum distance between the trajectory described and the track limits and obstacles

	Distance			Units
	Track 1	Track 2	Track 3	
Inner limit	1.32	1.22	1.98	[m]
Outer limit	1.54	1.58	1.46	[m]
Obstacles	0.79	0.73	0.77	[m]

Regarding the applicability of the developed algorithm to different scenarios, a remark should be made. Although the presented track layouts and obstacles positions were diversified, a difficulty in guaranteeing a trajectory without collision must be acknowledged, meaning that there is an awareness that the developed algorithm is difficult to generalise. So, the possibility of obtaining better results with a coupled approach —— regarding the steering and the velocity, as in [42, 43] — must be recognised since two aspects must be kept in mind: one is that the same steering command leads to different results if the vehicle is at different speeds; the other one is that the danger could be perceived differently, regardless of the distance, accordingly with the vehicle's direction.

Finally, it is important to mention that, even though it has not happened, the changes made to the

standard potential fields method could have led to instabilities due to the switches. Usually, it has to be ensured that the control action is a continuous function of, at least, class C^1 or C^2 and, even then, problems can arise.

Notwithstanding, the developed algorithm provided an intuitive and satisfactory solution for the problem at hand, providing a basis for future solutions: identifying the limitations of a solution is an important and necessary step for the characterisation and evolution of that same solution.

Chapter 6

Conclusions

From the various simulations performed to test the planning and control approaches developed in Chapters 3 and 4, respectively — using the FST vehicle model described in Chapter 2 — an extensive analysis of the results was performed in the previous chapter. Now, some conclusions about what was achieved in this dissertation will be drawn and notes about what should follow it will be provided.

6.1 Achievements

Analysing the results documented in the previous chapter, it can be concluded that the objectives of this work, stated in the Chapter 1, were accomplished. Such accomplishments were possible resorting to a simulation environment, in which a sufficiently complex vehicle model was used in order to adequately capture the desired dynamics and to guarantee reliable results. Thus, it was first necessary to devote some time to the understanding of the vehicle's dynamics.

Regarding path planning, the adopted approaches do not guarantee optimality, but allow for an improvement relatively to the typical baseline solution, currently used by FST team — in which the center-line is taken as reference path — portraying quite well the expected behaviour of a human driver since the vehicle showed a tendency to cut corners while driving slower in corners and faster on straights. Both online and offline provided solutions have proven to be robust in a wide range of racing scenarios. Lastly — although out of the FS scope —, an algorithm to provide a base solution to avoid static obstacles — which, in the present context, were intended to simulate other vehicles — was also developed. In this environment, the decoupling between the planning for lateral and longitudinal subsystems did not prove to be the best approach, as it was difficult to obtain a robust solution, not being applicable to a broad-spectrum of scenarios. Notwithstanding, it led to satisfactory results in different layouts and obstacles configurations, providing the proper basis for further development.

With respect to control, from a lateral point of view, different strategies were implemented, tested and compared with the one currently used in the real car — the Pure Pursuit controller —, which allowed to provide different possible solutions for the FST team. Since some of these strategies rely on or benefit from the use of a look-ahead distance for path-following error computation, two different mechanisms

were successfully implemented, which could be further tuned to attain better results. However, this was not done since combining it with all the other varying parameters would result in an even larger number of simulations which, in turn, could result in a loss of focus on the scope of this thesis. From the longitudinal point of view, the implemented control architecture is conceptually simple, but capable of taking into account longitudinal tire slip and dynamic mass transfers. Hence, the decoupled approach followed, in which the longitudinal and lateral controllers were tuned separately, has proven to be a robust solution to autonomously drive the vehicle in different scenarios.

Therefore, taking into account the results that have been obtained and all the comments above provided, it can be said that the objectives initially stipulated were effectively met, although some limitations were encountered.

6.2 Future Work

From the notes regarding the achievements of this work and the limitations encountered, suggestions about future research on this topic and what may follow this dissertation should be made.

Regarding path planning, minimum lap time formulations could be investigated in order to obtain a reference that simultaneously optimises the path and speed profile accounting for the vehicle dynamics and constraints. In addition, if such reference is obtained in an offline fashion, some mechanism to allow for an online update should be present since the actual conditions may not match those expected when the reference was generated. In the obstacle avoidance scenario, other approaches that allow a coupling between the lateral and longitudinal subsystems should be analysed — as in [24, 42, 43] — and the subject further developed to be able to deal with dynamic obstacles.

With respect to control, some additional strategies could be studied — like the MPC and MPCC, two examples already mentioned in this work — which could involve adaptive capabilities — from machine learning or neural networks algorithms, for example. These capabilities would certainly prove themselves useful in a racing scenario due to the repetitive environment created by the fact that multiple laps are to be taken. Furthermore, according to [24], from a control perspective, the fundamental building blocks for automatic racing can be grouped into three categories, namely drift control, reference tracking, and path planning, where the research associated with the first group focuses on gaining a better understanding of the behaviour of the car near the friction limit. Due to the loss of traction found in the skidpad event, after a certain speed, it could be beneficial to study control at the limits of handling or, as stated in the analysis of such phenomenon, study other tire models and steering geometries.

From a simulation point a view, several aspects regarding a more realistic environment should also be accounted for in future work — such as including an accurate modelling of the electrical powertrain components, some realistic models for the sensors and a mechanism that simulates the perception algorithms —, in order to evaluate the performance of the best solutions with a more truthful simulation.

Lastly, a reduced-scale model could also be developed, with the objective of verifying the reliability of the results obtained, assessing if the planning and control strategies implemented are applicable in a real-world situation, beyond simulation.

Bibliography

[1] *FSG Competition Handbook 2021*, June 2021.

[2] G. Klančar, A. Zdešar, S. Blažič, and I. Škrjanc. *Wheeled Mobile Robotics: From Fundamentals Towards Autonomous Systems*. Butterworth-Heinemann, 1st edition, 2017. ISBN:978-0128042045.

[3] M. H. Amoozgar. Development of fault diagnosis and fault tolerant control algorithms with application to unmanned systems. Master's thesis, Concordia University, 2012.

[4] S. Pendleton, H. Andersen, X. Du, X. Shen, M. Meghjani, Y. Eng, D. Rus, and M. Jr. Perception, planning, control, and coordination for autonomous vehicles. *Machines*, 5:6, 02 2017. doi: 10.3390/machines5010006.

[5] J. Van Brummelen, M. O'Brien, D. Gruyer, and H. Najjaran. Autonomous vehicle perception: The technology of today and tomorrow. *Transportation Research Part C: Emerging Technologies*, 89, 03 2018. doi: 10.1016/j.trc.2018.02.012.

[6] S. Grigorescu, B. Trasnea, T. T. Cocias, and G. Macesanu. A survey of deep learning techniques for autonomous driving. *ArXiv*, abs/1910.07738, 2020.

[7] D. Gonzalez Bautista, J. Pérez, V. Milanes, and F. Nashashibi. A review of motion planning techniques for automated vehicles. *IEEE Transactions on Intelligent Transportation Systems*, pages 1–11, 11 2015. doi: 10.1109/TITS.2015.2498841.

[8] W. Schwarting, J. Alonso-Mora, and D. Rus. Planning and decision-making for autonomous vehicles. *Annual Review of Control, Robotics, and Autonomous Systems*, 1, 05 2018. doi: 10.1146/annurev-control-060117-105157.

[9] J.-F. Duhé, S. Victor, and P. Melchior. Contributions on artificial potential field method for effective obstacle avoidance. *Fractional Calculus and Applied Analysis*, 24(2):421–446, 2021. doi: 10.1515/fca-2021-0019.

[10] M. Laurenza, G. Pepe, D. Antonelli, and A. Carcaterra. Car collision avoidance with velocity obstacle approach: Evaluation of the reliability and performace of the collision avoidance maneuver. In *2019 IEEE 5th International forum on Research and Technology for Society and Industry (RTSI)*, pages 465–470, 2019. doi: 10.1109/RTSI.2019.8895525.

[11] M. Gerdts, S. Karrenberg, B. Müller-Beßler, and G. Stock. Generating locally optimal trajectories for an automatically driven car. *Optimization and Engineering*, 10:439–463, 12 2009. doi: 10.1007/s11081-008-9047-1.

[12] R. Solea and U. Nunes. Trajectory planning and sliding-mode control based trajectory-tracking for cybercars. *Integrated Computer-Aided Engineering*, 13:1–15, 01 2006. doi: 10.3233/ICA-2007-14104.

[13] A. Liniger. *Path Planning and Control for Autonomous Racing*. PhD thesis, ETH Zurich, 2018.

[14] K. Kritayakirana and J. Gerdes. Autonomous vehicle control at the limits of handling. *Int. J. of Vehicle Autonomous Systems*, 10:271 – 296, 01 2012. doi: 10.1504/IJVAS.2012.051270.

[15] C. V. Samak, T. V. Samak, and S. Kandhasamy. Control strategies for autonomous vehicles. *ArXiv*, abs/2011.08729, 11 2020.

[16] h. TIAN, J. NI, and J. HU. Autonomous driving system design for formula student driverless race-car. In *2018 IEEE Intelligent Vehicles Symposium (IV)*, pages 1–6, 2018. doi: 10.1109/IVS.2018.8500471.

[17] L. Andresen, A. Brandemuehl, A. Honger, B. Kuan, N. Vodisch, H. Blum, V. Reijgwart, L. Bernreiter, L. Schaupp, J. Chung, M. Bürki, M. Oswald, R. Siegwart, and A. Gawel. Accurate mapping and planning for autonomous racing. In *2020 IEEE/RSJ International Conference on Intelligent Robots and Systems (IROS)*, pages 4743–4749, 10 2020. doi: 10.1109/IROS45743.2020.9341702.

[18] J. Kabzan, M. I. Valls, V. Reijgwart, H. F. C. Hendrikx, C. Ehmke, M. Prajapat, A. Bühler, N. Gosala, M. Gupta, R. Sivanesan, A. Dhall, E. Chisari, N. Karnchanachari, S. Brits, M. Dangel, I. Sa, R. Dubé, A. Gawel, M. Pfeiffer, A. Liniger, J. Lygeros, and R. Siegwart. Amz driverless: The full autonomous racing system. *ArXiv*, abs/1905.05150, 2020.

[19] R. Lot and F. Biral. A curvilinear abscissa approach for the lap time optimization of racing vehicles. In *IFAC Proceedings Volumes (IFAC-PapersOnline)*, volume 19, 08 2014. doi: 10.3182/20140824-6-ZA-1003.00868.

[20] A. Rucco, G. Notarstefano, and J. Hauser. Computing minimum lap-time trajectories for a single-track car with load transfer. In *2012 IEEE 51st IEEE Conference on Decision and Control (CDC)*, pages 6321–6326, 2012. doi: 10.1109/CDC.2012.6426265.

[21] A. Antunes. Sideslip estimation of formula student prototype. Master's thesis, IST, 2017.

[22] R. De Angelis Cordeiro, J. Azinheira, E. Paiva, and S. Bueno. Dynamic modeling and bio-inspired lqr approach for off-road robotic vehicle path tracking. In *2013 16th International Conference on Advanced Robotics (ICAR)*, pages 1–6, 11 2013. ISBN 978-1-4799-2722-7. doi: 10.1109/ICAR.2013.6766549.

[23] P. Torino. Combined lateral and longitudinal control for autonomous driving based on model predictive control. Master's thesis, Politecnico Di Torino, 2019.

[24] A. Liniger, A. Domahidi, and M. Morari. Optimization-based autonomous racing of 1:43 scale rc cars. *ArXiv*, abs/1711.07300, 2017.

[25] P. Polack, F. Altché, B. d'Andréa Novel, and A. de La Fortelle. The kinematic bicycle model: A consistent model for planning feasible trajectories for autonomous vehicles? In *2017 IEEE Intelligent Vehicles Symposium (IV)*, pages 812–818, 2017. doi: 10.1109/IVS.2017.7995816.

[26] J. Kong, M. Pfeiffer, G. Schildbach, and F. Borrelli. Kinematic and dynamic vehicle models for autonomous driving control design. In *2015 IEEE Intelligent Vehicles Symposium (IV)*, pages 1094–1099, 2015. doi: 10.1109/IVS.2015.7225830.

[27] J. L. Vázquez, M. Brühlmeier, A. Liniger, A. Rupenyan, and J. Lygeros. Optimization-based hierarchical motion planning for autonomous racing. *2020 IEEE/RSJ International Conference on Intelligent Robots and Systems (IROS)*, pages 2397–2403, 2020.

[28] R. Rajamani. *Vehicle Dynamics and Control*. Springer, 2nd edition, 2012. ISBN:978-1461414322.

[29] A. Boyali, S. Mita, and V. John. A tutorial on autonomous vehicle steering controller design, simulation and implementation. *ArXiv*, abs/1803.03758, 03 2018.

[30] A. Barroso. Traction control of a formula student prototype. Master's thesis, IST, 2021.

[31] R. Cordeiro. Modelagem e controle de trajetória de um veículo robótico terrestre de exterior. Master's thesis, UNICAMP, 2013.

[32] *AMK Racing Kit*. AMK GmbH, 2015/26 edition, 2015.

[33] A. Athayde. Path following and control for autonomous driving of a formula student car. Master's thesis, IST, 2021.

[34] M. Veneri and M. Massaro. The effect of ackermann steering on the performance of race cars. *Vehicle System Dynamics*, 59:1–21, 02 2020. doi: 10.1080/00423114.2020.1730917.

[35] H. B. Pacejka and E. Bakker. The magic formula tyre model. *Vehicle System Dynamics*, 21(sup001): 1–18, 1992. doi: 10.1080/00423119208969994.

[36] *Continental Formula Student Tire: Competition Tire 2019 (C19) - Documentation*. Continental AG, 2019.

[37] J. Antunes. Torque vectoring for a formula student prototype. Master's thesis, IST, 2017.

[38] *FSG Rules 2020*, 2020. URL `https://www.formulastudent.de/fsg/rules/`.

[39] D. Valério and J. Costa. *An Introduction to Fractional Control*. The Institution of Engineering and Technology, 2013. ISBN:978-1-84919-546-1.

[40] B. Metoui, P. Melchior, S. Najar, M. Abdelkrim, and A. Oustaloup. Robust path planning for dynamic environment based on fractional attractive force. In *2009 6th International Multi-Conference on Systems, Signals and Devices*, pages 1–8, 2009. doi: 10.1109/SSD.2009.4956793.

[41] J. Filip. Trajectory tracking for autonomous. Master's thesis, Czech Technical University in Prague, 2017/2018.

[42] T. Andrade. Radar vs lidar for obstacle detection and collision avoidance. Master's thesis, IST, 2020.

[43] A. Ferreira. Teleoperation with force feedback: Easing unmanned vehicles operation in unknown scenarios. Master's thesis, IST, 2015.

[44] M. Montemerlo, H. Dahlkamp, D. Stavens, A. Aron, J. Diebel, P. Fong, J. Gale, M. Halpenny, G. Hoffmann, K. Lau, C. Oakley, M. Palatucci, V. Pratt, P. Stang, S. Strohband, C. Dupont, L.-E. Jendrossek, C. Koelen, and P. Mahoney. Stanley: The robot that won the darpa grand challenge. *J. Field Robotics*, 23:661–692, 01 2006.

[45] K. Ogata. *Modern Control Engineering*. Prentice Hall, 5th edition, 2009. ISBN 9780136156734.

[46] S. Dominguez, A. Ali, G. Garcia, and P. Martinet. Comparison of lateral controllers for autonomous vehicle: Experimental results. In *2016 IEEE 19th International Conference on Intelligent Transportation Systems (ITSC)*, pages 1418–1423, 2016. doi: 10.1109/ITSC.2016.7795743.

[47] S. Park, J. Deyst, and J. How. A new nonlinear guidance logic for trajectory tracking. In *In Proceedings of the AIAA Guidance, Navigation and Control Conference*, 08 2004. ISBN 978-1-62410-073-4. doi: 10.2514/6.2004-4900.

[48] M. Linderoth, K. Soltesz, and R. Murray. Nonlinear lateral control strategy for nonholonomic vehicles. In *2008 American Control Conference*, pages 3219 – 3224, 07 2008. doi: 10.1109/ACC.2008. 4586988.

[49] L. Chen, N. Liu, Y. Shan, and L. Chen. A robust look-ahead distance tuning strategy for the geometric path tracking controllers. In *2018 IEEE Intelligent Vehicles Symposium (IV)*, pages 262–267, 2018. doi: 10.1109/IVS.2018.8500623.

[50] C. Kunusch, P. Puleston, and M. Mayosky. *Fundamentals of Sliding-Mode Control Design*. Springer London, 1st edition, 2012. ISBN:9781447124306.

[51] D. Liberzon. *Switching in Systems and Control*. Springe, 1st edition, 2003. ISBN:9780817642976.

[52] K. Jalali, S. Lambert, and J. McPhee. Development of a path-following and a speed control driver model for an electric vehicle. *SAE International Journal of Passenger Cars - Electronic and Electrical Systems*, 5:100–113, 05 2012. doi: 10.4271/2012-01-0250.

[53] Ö. B. Bilen. Path control algorithms for autonomous steering and braking of heavy vehicles. Master's thesis, Chalmers University of Technology, 2010.

[54] M. Gendreau and J.-Y. Potvin. *Handbook of Metaheuristics*. Springer Publishing Company, Incorporated, 2nd edition, 2010. ISBN 1441916636.

Appendix A

Parameters

In this appendix the parameters used throughout this dissertation are presented, being divided into three major categories namely simulation, planning and control.

Being the more encompassing, the simulation section presents the values of all the parameters required for, as the name suggests, simulation. Such parameters are related with the models developed — both the simplified and realistic — and with the initial conditions used for the realistic model. Regarding the planning section, the parameters related with the potential field method — for both FS events and obstacle avoidance scenarios — as well as the ones related with the algorithm used for obtaining the speed profile are presented. Lastly, with respect to the control section, the gains for all the developed controllers and observers are shown, together with the range for which the longitudinal controller was developed and the parameters used for the look-ahead profiles.

A.1   Simulation

Table A.1: Environment parameters

Notation	Description	Value	Units
ρ	Air density	1.2	kg/m^3
μ	Coefficient of friction	1.5	–
g	Gravitational acceleration	9.807	m/s^2

Table A.2: Aerodynamic coefficients

Notation	Description	Value	Units
C_D	Aerodynamic drag coefficient	1.27	–
C_L	Lift coefficient	3.11	–

Table A.3: Vehicle model parameters

Notation	Description	Value	Units
m	Mass	256	kg
I_{xx}	Moment of inertia around x	39.00	kg·m^2
I_{yy}	Moment of inertia around y	141.61	kg·m^2
I_{zz}	Moment of inertia around z	160.62	kg·m^2
R	Wheels radius	0.228	m
L_F	Distance of front axis to the CG	0.816	m
L_R	Distance of rear axis to the CG	0.724	m
L	Wheelbase	1.54	m
L_W	Track width	1.20	m
L_H	CG height	0.265	m
A_P	Projected frontal area	1.05	m^2
J_w	Wheels rotational inertia	0.24	kg·m^2
a_w	Half-length of contact patch	0.06	m

Table A.4: Tires parameters (IP: 0.8 bar) for front and rear axle

Notation	Description	Value		Units
		Simplified model	Realistic model	
B_x	Longitudinal stiffness factor	25.87	20	–
C_x	Longitudinal shape factor	1.40	1.9	–
D_x	Longitudinal peak-value	1240	1	–
E_x	Longitudinal curvature factor	–	0.6	–
B_y	Lateral stiffness factor	15.57	10	–
C_y	Lateral axle shape factor	1.32	2.2	–
D_y	Lateral peak-value	1195	1	–
E_y	Lateral curvature factor	–	0.50	–
B_z	Vertical axle stiffness factor	–	10	–
C_z	Vertical shape factor	–	0.05	–
D_z	Vertical peak-value	–	1	–
E_z	Vertical curvature factor	–	5	–
C_α	Effective cornering stiffness	24560.1	–	N/rad

Table A.5: Powertrain and steering parameters

Notation	Description	Value	Units
r_gear	Gear ratio of the transmission	16.25	–
η_PT	Powertrain efficiency	0.90	–
τ_PT	Powertrain time constant	0.02	s
τ_SA	Steering time constant	0.1	s
δ_max	Maximum steering angle (clockwise)	0.49	rad
δ_min	Minimum steering angle (counter-clockwise)	-0.49	rad

Table A.6: Additional parameters for realistic model

Notation	Description	Value	Units
C_t	CG translation coefficient	0.8	kg/m
C_d	CG downforce coefficient	1.96	kg/m
C_r	CG rotation coefficient	0.001	kg·s^2
C_{r_ω}	Wheels rotation coefficient	0.003	kg·s^2
c	Damping coefficient for each suspension quarter	2000	N·s/m
k_F	Spring constant for front suspension quarter	52490	N/m
k_R	Spring constant for rear suspension quarter	45000	N/m
r_{motion_F}	Front suspension quarter motion ratio	1.11	–
r_{motion_R}	Rear suspension quarter motion ratio	1.14	–

Table A.7: Initial conditions used in simulation

Notation	Description	Value	Units
$\mathbf{v}$	Linear CG velocity in the body frame	[0.1 0 0]	m/s
Ω	Angular CG velocity in the body frame	[0 0 0]	rad/s
$\mathbf{p}_{CG}$	CG position in the global frame	[0 0 -0.265]	m
Φ	Euler angles	[0 0 0]	rad
ω	Angular speeds for each wheel	[0.44 0.44 0.44 0.44]	rad/s
$\mathbf{t}_w$	Torques delivered by each tire	[0 0 0 0]	N·m
δ	Steering wheel angle	0	rad

A.2 Planning

Table A.8: Artificial potential field parameters for trackdrive event

Notation	Description	Value			Units
		FSG	FSI	Thin	
K_{att}	Attractive force gain	1	1	1	N/m
K_{rep}	Repulsive force gain	2	1	4	N
γ	Decay factor	10	2.5	3.5	–
v_x	Forward velocity	5	5	5	m/s
offset	Number of points ahead	4	6	8	–
d_{offset}	Approximate distance of point ahead	6.16	6.54	7.52	m
d_{min}	Distance from which the danger is 1	0.75	0.75	0.75	m

Table A.9: Speed profile generation parameters

Notation	Description	Value			Units
		FSG	FSI	Thin	
Δs	Sampling step in distance	1.50	1.04	0.89	m
η_{trans}	Transmission efficiency	0.70	0.70	0.70	–
v_{x_0}	Initial velocity	0.10	0.10	0.10	m/s
$v_{x_{\text{lim}}}$	Maximum velocity	26.5	26.5	26.5	m/s

Table A.10: Artificial potential field parameters for autocross event

Notation	Description	Value			Units
		FSG	FSI	Thin	
K_{att}	Attractive force gain	1	1	1	N/m
K_{rep}	Repulsive force gain	2.5	2.5	2.5	N
γ	Decay factor	4	4	4	–
offset	Number of points ahead	4	6	7	–
d_{offset}	Approximate distance of point ahead	6.16	6.54	6.58	m
d_{min}	Distance from which the danger is 1	0.75	0.75	0.75	m

Table A.11: Artificial potential field parameters for obstacle avoidance

Notation	Description	Value Track limits	Obstacles	Units
offset	Number of points ahead	4		–
K_{att}	Attractive force gain	1		N/m
K_{att}^c	Corrected attractive force gain	0.7		N/m
d_{pred}	Distance used to predict collision	$2.5L$		m
K_{rep}	Repulsive force gain	5	2	N
K_{rep}^c	Corrected repulsive force gain	5	4	N
γ	Decay factor	2	2	–
d_{min}	Distance from which the danger is 1	0.75	$3L$	m
d_{max}	Distance from which the danger is 0	Variable	$4L$	m

A.3 Control

A.3.1 Longitudinal Control

Table A.12: Operational range used in simulation

Notation	Description	Value	Units
$T_{F_{\text{range}}}$	Front motors torque range	[-5 10]	N·m
$T_{R_{\text{range}}}$	Rear motors torque range	[-5 15]	N·m
κ_{range}	Slip ratio range	[-0.03 0.07]	–
$\kappa_{\text{diff}_{\text{range}}}$	Slip ratio asymmetry range	[-0.03 0.03]	–

$$K_\kappa^F = 250 \quad \text{(A.1)} \qquad\qquad K_\kappa^R = 350 \quad \text{(A.2)}$$

$$K_{v_x} = 0.1 \quad \text{(A.3)} \qquad\qquad K_{\dot\psi} = 0.03 \quad \text{(A.4)}$$

A.3.2 Lateral Control

Table A.13: Look-ahead parameters

Notation	Description	Value	Units
L_{lad}^{const}	Constant look-ahead used in linear profile	1	m
t_{react}	Reaction time used in linear profile	0.25	s
L_{lad}^{ref}	Reference look-ahead used in parabolic profile	1	m
$v_{x_{\text{ref}}}$	Reference velocity used in parabolic profile	5	m/s

Linear Quadratic Gaussian

$$Q_0^{LQG} = \begin{bmatrix} 0.5 & 0 & 0 & 0 \\ 0 & 0.1 & 0 & 0 \\ 0 & 0 & 0.1 & 0 \\ 0 & 0 & 0 & 1 \end{bmatrix} \quad \text{(A.5)} \qquad Q^{LQG} = \begin{bmatrix} 7 & 0 & 0 & 0 \\ 0 & 15 & 0 & 0 \\ 0 & 0 & 1 & 0 \\ 0 & 0 & 0 & 1 \end{bmatrix} \quad \text{(A.6)}$$

$$R_0^{LQG} = \begin{bmatrix} 0.01 & 0 \\ 0 & 0.01 \end{bmatrix} \quad \text{(A.7)} \qquad R^{LQG} = 5 \quad \text{(A.8)}$$

Kinematics Lateral Speed

$$K_\psi^{KLS} = 1 \quad \text{(A.9)} \qquad K_{e_y}^{KLS} = 2.5 \quad \text{(A.10)}$$

Modified Sliding Mode

$$Q_0^{MSM} = \begin{bmatrix} 15 & 0 & 0 & 0 \\ 0 & 1 & 0 & 0 \\ 0 & 0 & 5 & 0 \\ 0 & 0 & 0 & 1 \end{bmatrix} \quad \text{(A.11)} \qquad R_0^{MSM} = \begin{bmatrix} 0.01 & 0 \\ 0 & 0.01 \end{bmatrix} \quad \text{(A.12)}$$

$$Q_0^{MSM} = \begin{bmatrix} 0.8 & 0 & 0 & 0 \\ 0 & 0.5 & 0 & 0 \\ 0 & 0 & 0.8 & 0 \\ 0 & 0 & 0 & 0.5 \end{bmatrix} \quad \text{(A.13)} \qquad R_0^{MSM} = \begin{bmatrix} 0.01 & 0 \\ 0 & 0.01 \end{bmatrix} \quad \text{(A.14)}$$

$$K_\sigma^{MSM} = 7 \quad \text{(A.15)} \qquad K_{e_\psi}^{MSM} = 0.1 \quad \text{(A.16)}$$

$$K_{e_y}^{MSM} = 1 \quad \text{(A.17)}$$

Regarding this controller a remark should be made, explaining the reason behind having two different matrices for the covariances related with the observer, where the first ones were used for the simplified model and the second ones for the realistic model.

It was noticed that, for the realistic model, from a certain point, the convergence of the estimations stagnated, always existing an offset — as it was shown in Chapter 5 — due to the effect of nonlinearites. Since the relative difference between the process and sensor noise variances affects not only the con-

vergence velocity of the estimations — which, as mentioned, only happens until a certain point in the case of the realistic model —, but also the bandwidth of the filter, i.e, the amount of noise filtered, it was chosen to decrease the values related to the process covariance matrix in order to decrease the bandwidth.

Appendix B

Additional Information

In this appendix additional information is provided. In the first section, which concerns the motors, the efficiency map and the characterisation of the electric motors — from a mechanical standpoint — are presented. In the last section, dedicated to tires, the boundaries of the parameters for which the tire model provided by Continental AG is valid are shown. The maximum values, for the Pacejka tire model, and the regions where a linear relation between slip ratio or slip angle and force or moment is verified are also provided.

B.1 Motors

Table B.1: Efficiency map with the region of high motor efficiency highlighted

Motor torque [N·m]	Motor speed [rpm]									
	500	1000	2000	3000	4000	6000	10000	12000	15000	19000
1.3	64.37	71.33	73.64	74.70	75.43	76.57	77.00	77.08	77.56	78.14
2.7	58.42	70.48	77.57	80.40	82.01	83.92	85.16	85.44	85.97	86.50
5.4	44.94	60.81	73.35	78.82	81.94	85.43	88.2	88.88	89.71	90.44
7.9	35.59	51.90	67.02	74.26	78.54	83.42	87.58	88.65	89.84	90.86
10.4	29.14	44.78	61.01	69.41	74.57	80.62	85.93	87.34	88.86	90.16
12.5	24.17	38.71	55.22	64.39	70.24	77.30	83.73	85.48	87.37	88.98
14.4	20.41	33.76	50.04	59.65	65.99	73.88	81.33	83.42	85.66	87.59
16.0	17.31	29.40	45.10	54.87	61.55	70.10	78.56	80.97	83.56	85.81
17.4	14.82	25.75	40.67	50.41	57.28	66.34	75.70	78.40	81.34	82.71
18.5	12.81	22.67	36.72	46.30	53.25	62.67	72.77	75.75	79.02	76.96
19.6	11.17	20.05	33.21	42.51	49.44	59.09	69.82	73.06	67.66	69.28

Table B.2: Electric motor characteristics

Notation	Description	Value	Units
T_{nom}	Nominal torque	10	N·m
T_{max}	Maximum torque	21	N·m
N_{nom}	Nominal speed	12000	rpm
N_{max}	Maximum speed	20000	rpm

B.2 Tires

Table B.3: Boundaries of the parameters used in the tire model

Notation	Description	Value		Units
		Minimum	Maximum	
F_z	Vertical load	230	1600	N
κ	Slip ratio	-0.25	0.25	–
α	Slip angle	-0.20	0.20	rad

Table B.4: Slip ratio and slip angle critical values and linear ranges

Notation	Description	Value	Units
κ_{cri}	Slip ratio for maximum force	0.07	–
α_{cri}	Slip angle for maximum force	0.10	rad
κ_{lin}	Slip ratio range for linear relation	[-0.025 0.025]	–
α_{lin}	Slip angle range for linear relation	[-0.040 0.040]	rad

Appendix C

Other Approaches

As mentioned in section 3.1.3.1, although some other approaches were developed in order to obtain a reference path for the trackdrive event, it was not possible to use them to obtain satisfactory results. For this reason, they are presented in this Appendix rather than in main text. As such, the following sections will be dedicated to the description of the reasoning behind those approaches.

The first subsection concerns the meta-heuristic algorithm developed to obtain a more optimised reference path having the centerline as an initial solution. The second and last subsection presents a methodology different from those mentioned in section 3.1.3.1, to obtain the attractive force needed in the potential field method.

C.1   Meta-heuristic

As mentioned before, using the centerline as reference path for the trackdrive event is not the best approach since a lot of time will be spent in curves, being necessary to develop another solution. Although the method presented in section 3.1.3.1, to find a more optimised reference, was a sweep procedure using a potential fields method, a solution involving a meta-heuristic was also implemented.

Assuming a constant speed between two consecutive waypoints, from the maximum lateral acceleration $a_{y\max}$ and curvature K_n of a segment n, such speed can be given by [33]

$$v_{x_n} = \sqrt{\frac{a_{y\max}}{|K_n|}} \qquad \text{[m/s]} \tag{C.1}$$

Since the vehicle must stay within the track boundaries, a minimum lap time problem can be formulated as

$$
\begin{aligned}
\text{minimise} \quad & t_{finish} = \sum_{n=1}^{n=N-1} \frac{l_n}{v_{x_n}} \\
\text{subject to} \quad & (X,Y)_0 = (X,Y)_N \\
& (X,Y) \in (X,Y)_{\text{track}} \\
& v_{x_n} \leqslant v_{x_{\max}}, \ n = 1,...,N
\end{aligned}
\tag{C.2}
$$

93

where l_n denotes the length of segment n, N the number of waypoints and the decision variables are the location of the points in the global frame (X, Y).

Being possible to solve such problem with different meta-heuristics algorithms, Simulated Annealing was the one chosen. This algorithm may accept movements that lead to worse solutions than the current one in order to avoid trapping the solution in a local minimum. Nevertheless, it is important to note that the probability of accepting such movement decreases during the search through a temperature parameter.

Starting with an initial solution x — which in this case is the centerline — a candidate solution y is generated and its acceptance is decided based on the Metropolis criterion. Designating the temperature by T, this criterion can be described mathematically by

$$p = \begin{cases} 1 & \text{if } f(y) \leqslant f(x) \\ e^{-\frac{f(y)-f(x)}{T}} & \text{otherwise} \end{cases} \tag{C.3}$$

For the addressed problem, the new solution is created ensuring that each point can change its position if and only if the new position presents a danger level below 1, being such position obtained assuming a Gaussian distribution for the radius and a uniform distribution for the angle, as represented in Figure C.1.
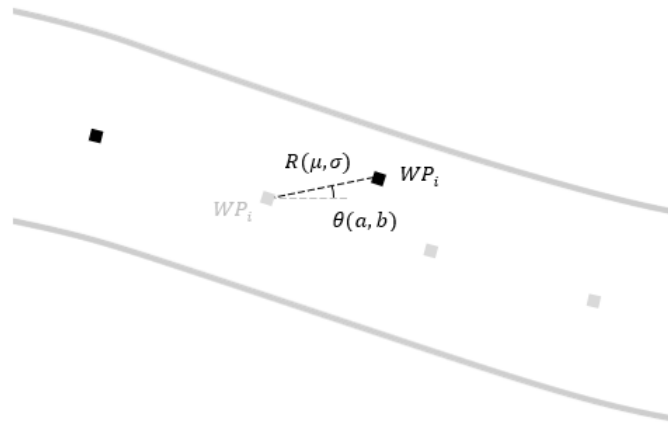

Figure C.1: Schematic of the methodology implemented to obtain a new solution

Regarding the temperature cooling schedule, this should consist of an initial temperature, a decrease function, a Markov chain and an end condition. Being the geometric cooling the most commonly used — and the one implemented — such schedule can be described by updating the temperature according to the ratio

$$T_{k+1} = \lambda T_k \tag{C.4}$$

where λ designates the cooling factor. The inherent process to Simulated Annealing is characterised by starting with high temperature values — when compared to typical values of $|f(y) - f(x)|$ — in order to obtain a relatively high probability of acceptance, thus allowing a search in random directions. With the gradual decrease in temperature values a gradual decrease in probability occurs, allowing to increase

the focus on the best solution.

From the implemented algorithm presented in Figure C.2 it is possible to verify that changes have been made in relation to the standard Simulated Annealing [54], with regard to the verification of the solution stagnation occurrence and in the implementation of counter-measures in these circumstances. These measures consist in increasing the temperature and resetting the solution. The temperature control was carried out in the inner cycle, in order to increase this parameter and, consequently, the search area. The reset was implemented in the outer cycle and, in case this intervention does not allow an improvement in the solution, the program is forced to end.

Establishing a number of iterations that correspond to the occurrence of stagnation, it is necessary to determine how the increase will be carried out. For this purpose, a division of the temperature was considered as "high" and "low", with any value below a defined threshold of the initial temperature being considered low. Although at high temperatures the increase was done simply considering

$$T_{k+1} = T_k + C_1 \cdot |T_0 - T_k| \tag{C.5}$$

where C_1 is a constant, at a low temperatures another relation was used, in a form of

$$T_{k+1} = C_2 \cdot |T_0 - T_k| \tag{C.6}$$

where C_2 is a constant, since, at low temperatures, the difference between T_0 and T_k is more significant avoiding the need of a fixed term.

Lastly, with respect to the resetting of the solution, this consists on enabling a greater focus on the search as, after a predetermined number of iterations has elapsed without obtaining a better solution, the current solution returns to being the best found so far. However it is still important to mention that, since this restart is not intended to occur prematurely or belatedly, in order to prevent the hindrance of the solution evolution, the value attributed to the number of iterations requires a careful decision.

With all of the above being implemented, the method was tested; however it stood out that from a certain point — which occurs relatively soon regarding the total number of iterations — obtaining a valid solution became too difficult and the algorithm got stuck or stagnated. In order to overcome this, several measures were tried, namely changing the radius of possible new positions for each point, the number of points used to obtain a new solution and the initial point considered.

Regarding the radius, since the new position is created with a uniform distribution for the angle and a Gaussian distribution for the radius, the standard deviation of this last distribution was changed with the intent of decreasing the liberty given to each point. However, the restraining of the allowed space to generate a new solution makes it difficult to obtain solutions with significant differences through iterations leading to stagnation. Furthermore, as the tracks are relatively narrow, the possible range for the standard deviation is restricted.

With respect to the last two measures, as the probability of obtaining a coherent movement of points decreases with the increase of the number of points considered to create a new solution, only some were used. Taking into consideration that, in addition to what was just mentioned, the use of few points
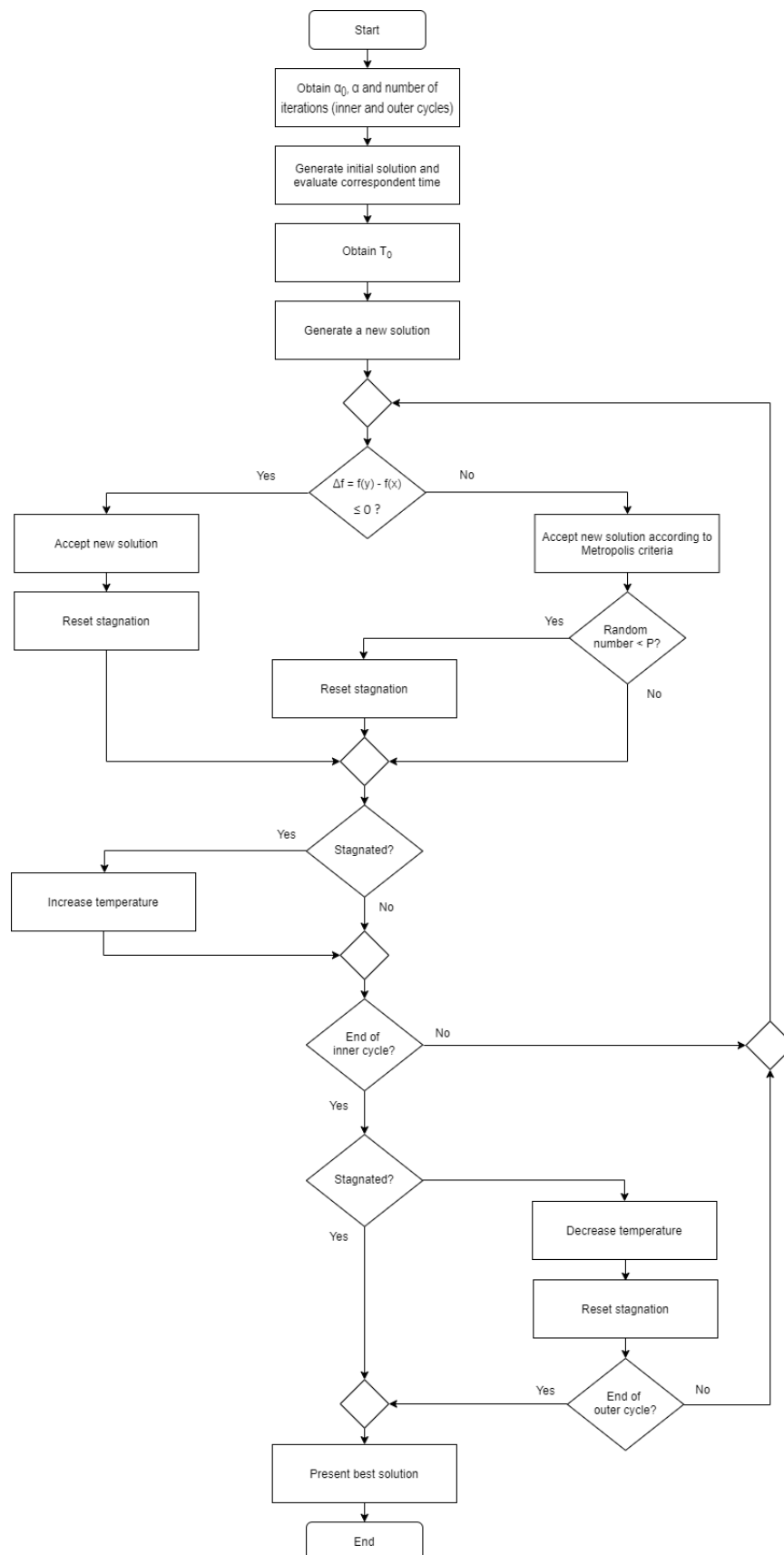
Figure C.2: Simulated Annealing flowchart

can also invalidate the solution — as the interpolation may intersect the track boundaries —, the number of neglected points used was changed. Once the reference "step" was established, the initial point was selected randomly from a set of the first n points to prevent always changing the location of the same points.

Although the presented measures helped to counteract the issue, none of them — isolated or combined — was able to effectively solve the problem or to allow the algorithm to provide better solutions than the centerline. Thereby, this method was abandoned and the potential field method combined with the sweep procedure was adopted.

C.2 Potential Field

As mentioned in section 3.1.3.1, three methods were developed with regard to the attractive force. Although the two that were presented are in a two-dimensional space, one attempt to simulate the attractive force was done resorting to a three-dimensional one.

As represented in Figure C.3, the main idea behind this approach consists in simulating a given track — the centerline of which has length of l — as a spiral with periodicity l and a cross section profile defined by the potential shape — being some examples sketched in Figure 3.5. This way, neglecting any existing friction, the movement of the vehicle will only be a consequence of the gravitational force $\mathbf{f}_g$ and the reaction $\mathbf{f}_{\text{react}}$ created by the spiral. Being the control action δ_{cmd} still obtained from the resultant force $\mathbf{f}$ and the heading of the vehicle ψ — as represented in Figure 3.6 —, it is then necessary to compute the resultant force.
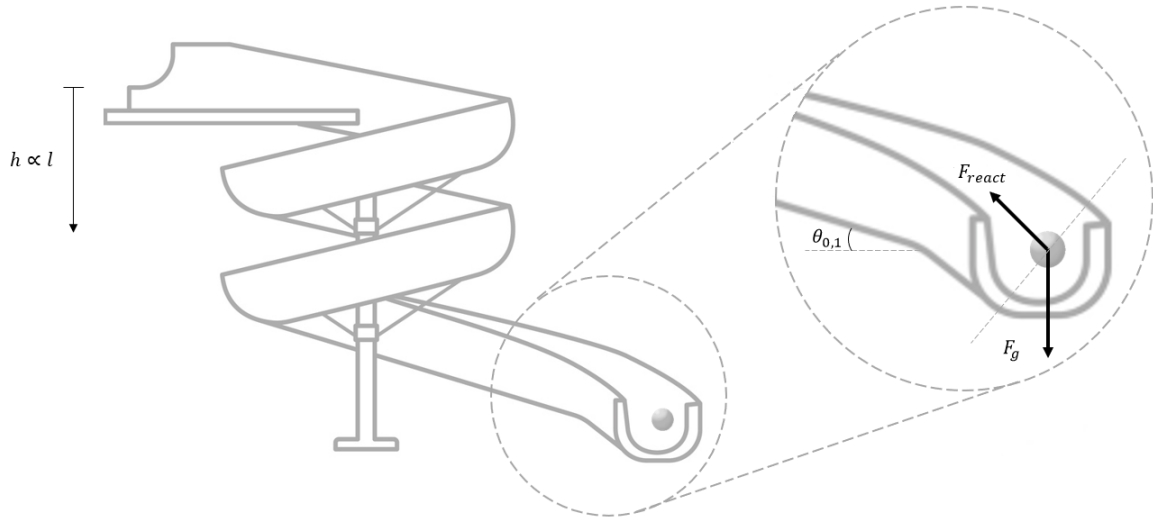

Figure C.3: Main idea behind the approach followed in three-dimensions

Representing the vehicle as a sphere — by analogy to be modelled as a charged particle in the potential field methods —, when slightly off from the centerline, the reaction force will be perpendicular to the tangency plan passing through the contact point and the gravitational force will be pointing downwards, as represented in the amplified region of Figure C.3.

To compute the resultant from these forces, three reference frames were used: the first following the NED convention, the second obtained through a rotation $\theta_{0,1}$ around the y axis, having the spiral inclination, and the third obtained through a rotation $\theta_{1,2}$ around the x axis of the previously reference frame and oriented in such way that the z axis and the reaction force are collinear, but with opposite directions. These references frames are associated with the subscripts 0, 1 and 2, respectively. The inherent rotations are schematically represented in Figures C.4 and C.5 and mathematically described in equations (C.7) and (C.8)
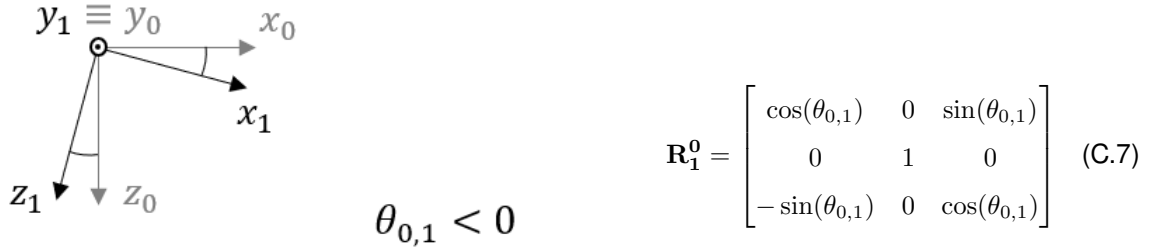

$$\mathbf{R}_1^0 = \begin{bmatrix} \cos(\theta_{0,1}) & 0 & \sin(\theta_{0,1}) \\ 0 & 1 & 0 \\ -\sin(\theta_{0,1}) & 0 & \cos(\theta_{0,1}) \end{bmatrix} \quad \text{(C.7)}$$

Figure C.4: Rotation to obtain frame 1 from frame 0

$$\mathbf{R}_2^1 = \begin{bmatrix} 1 & 0 & 0 \\ 0 & \cos(\theta_{1,2}) & -\sin(\theta_{1,2}) \\ 0 & \sin(\theta_{1,2}) & \cos(\theta_{1,2}) \end{bmatrix} \quad \text{(C.8)}$$
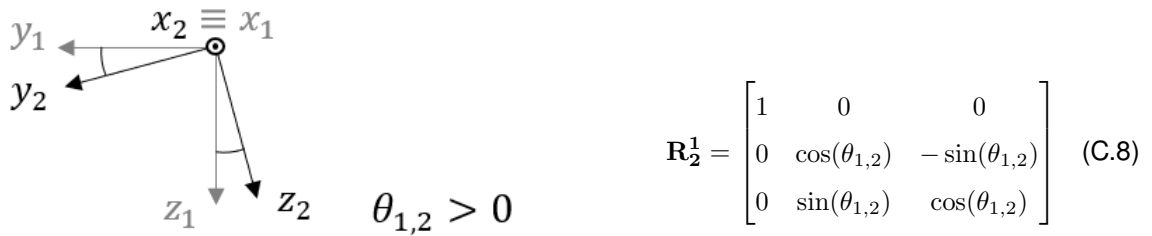
Figure C.5: Rotation to obtain frame 2 from frame 1

Since the composition of successive rotations is obtained by post multiplication of the rotation matrices, following the given order of rotations, the rotation matrix of frame 2 with respect to frame 0 $\mathbf{R}_2^0$ can be given by

$$\mathbf{R}_2^0 = \begin{bmatrix} \cos(\theta_{0,1}) & 0 & \sin(\theta_{0,1}) \\ \sin(\theta_{0,1})\sin(\theta_{1,2}) & \cos(\theta_{1,2}) & -\cos(\theta_{0,1})\sin(\theta_{1,2}) \\ -\sin(\theta_{0,1})\cos(\theta_{1,2}) & \sin(\theta_{1,2}) & \cos(\theta_{0,1})\cos(\theta_{1,2}) \end{bmatrix} \quad \text{(C.9)}$$

Being $\mathbf{f}_g$ and $\mathbf{f}_{\text{react}}$ easily expressed in reference frames 0 and 2, as they are aligned with z_0 and z_2, respectively, $\mathbf{f}$ can be computed from the vector sum of both forces expressed in the same frame. As such

$$\mathbf{f}^2 = \mathbf{f}_g^2 + \mathbf{f}_{react}^2 \quad \text{[N]} \quad \text{(C.10)}$$

where

$$\mathbf{f}_g^2 = \mathbf{R_0^2}\mathbf{f}_g^0 = (\mathbf{R_2^0})^{-1}\mathbf{f}_g^0 = \begin{bmatrix} mg\sin(\theta_{0,1}) \\ -mg\cos(\theta_{0,1})\sin(\theta_{1,2}) \\ mg\cos(\theta_{0,1})\cos(\theta_{1,2}) \end{bmatrix} \qquad [\text{N}] \qquad (\text{C.11a})$$

$$\mathbf{f}_{\text{react}}^2 = \begin{bmatrix} 0 \\ 0 \\ -F_{g_z}^2 \end{bmatrix} \qquad [\text{N}] \qquad (\text{C.11b})$$

Finally, expressing such force in the NED frame in order to compute the control action, it is possible to obtain

$$\mathbf{f}^0 = \mathbf{R_2^0}\mathbf{f}^2 = \begin{bmatrix} mg\cos(\theta_{0,1})\sin(\theta_{0,1})\cos^2(\theta_{1,2}) \\ -mg\cos(\theta_{0,1})\cos(\theta_{1,2})\sin(\theta_{1,2}) \\ mg\big(\sin^2(\theta_{0,1}) + \sin^2(\theta_{1,2})\cos^2(\theta_{0,1})\big) \end{bmatrix} \qquad [\text{N}] \qquad (\text{C.12})$$

where, regarding the angles, $\theta_{0,1}$ can be seen as a design parameter and $\theta_{1,2}$ can be obtained as the partial derivative of the danger level U, presented in (3.2), with respect to the distance d, i.e.

$$\theta_{1,2} = \arctan\left(\frac{\partial U}{\partial d}\right) = \arctan\left(\frac{(1-\gamma)\,d^{-\gamma}}{d_{\text{min}}^{(1-\gamma)} - d_{\text{max}}^{(1-\gamma)}}\right) \qquad [\text{rad}] \qquad (\text{C.13})$$

Although this approach could be seen as intuitive and reasonable, it was not possible to obtain satisfactory results from it since the vehicle was not been able to remain within the track for more than a short distance, as shown in Figure C.6. Analysing the figure, it was possible to note that the greater the distance from the centerline, the greater the tendency for the car to leave the track and, additionally, that the car stays on track for a longer distance when the spiral inclination is higher, which could be seen as counter-intuitive. The scenario where such results seem reasonable implies a convex potential shape instead of a concave one, but the flaw in reasoning that led to this has not been found. As such, this approach was dropped and the ones presented in a two-dimensional space were used.
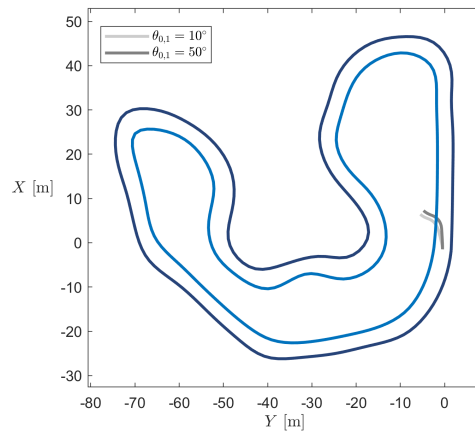

Figure C.6: Results obtained using a three-dimensional approach